TUNGSTEN INJECTION MOLDING

FOR AUTOMOTIVE APPLICATIONS

JITTRABHANU LAMLERTTHAM

A THESIS SUBMITTED IN PARTIAL FULFILLMENT

OF THE REQUIREMENT FOR THE DEGREE OF

MASTER OF ENGINEERING IN AUTOMOTIVE ENGINEERING

(INTERNATIONAL PROGRAM)

INTERNATIONAL COLLEGE

KING MONGKUT'S INSTITUTE OF TECHNOLOGY LADKRABANG

2011

KMITL-2011-IC-M-004-018

Thesis Title	Tungsten Injection Molding for Automotive Applications
Student	Mr. Jittrabhanu Lamlerttham
Student ID.	52600912
Degree	Master of Engineering
Program	Automotive Engineering (International Program)
Year	2011
Thesis Advisor	Assoc. Prof. Dr. Jaruwat Charoensuk
	Dr. Ruangdaj Tongsri
	Prof. Yoshio Saito

ABSTRACT

In this work, the processing steps for producing tungsten parts via metal injection molding method were studied. The ready-to-mold feedstock (94W with Ni-Cu-Co alloy) was used in molding step. Injection molding was performed at 175°C with the mold temperature of 100°C. In a densification process, the molded specimens were debinded by catalytic debinding technique to convert to the brown specimens. After debinding, the brown specimens were sintered under vacuum atmosphere. Sintering temperatures and sintering times were varied from 1350 to 1450°C and from 2 to 4 hours respectively. Optimal sintering temperature and sintering time were studied. The effects of sintering conditions on density, mechanical properties, microstructures and shrinkage were analyzed. It was found that with varied sintering temperatures, the temperature of 1450°C provided sintered specimens with better properties than the others. At the sintering temperature of 1450°C and with varied sintering times, the W-(Ni-Cu-Co) specimens sintered for 3 hours achieved the highest density of 18.02 g/cm^3 and the optimal mechanical properties with hardness and UTS of 105.9 HRB and 776 MPa respectively. The minimum porosity was also obtained when this condition was employed. For long sintering time (6 and 8 hours) at the sintering temperature of 1450°C resulted in coalescence to each other between tungsten particles and inevitably porosity growth. This phenomenon caused inferior density and mechanical properties of the sintered specimens. Thus, mechanical properties significantly depend on the microstructural parameters such as tungsten grain size, tungsten particles contiguity and porosity. The specimens sintered at 1450°C with too long sintering time (8 hours) were brittle. Different vacuum levels and nitrogen atmosphere were also studied for sintering the brown W-(Ni-Cu-Co)

specimens at 1450°C for 3 hours. The results show that increasing of sintering chamber pressure caused detrimental effects on both physical and mechanical properties of the sintered tungsten specimens. In addition, nitrogen atmosphere gave similar results as those of the cases of increased chamber pressure.

ACKNOWLEDGEMENT

This thesis could not be completed without the assistance of many persons to whom I would like to express my sincere appreciation.

First, I would like to sincerely thank my advisor, Dr. Ruangdaj Tongsri, who has given me this opportunity and made this work successful, and I am also grateful to his kindness, many helpful suggestions and fruitful discussions during the undertaken research. I would also like to sincerely thank Assoc. Prof. Dr. Jaruwat Charoensuk for kind advising and helping, and Prof. Yoshio Saito for the suggestion of this thesis.

I am grateful to National Science and Technology Development Agency (NSTDA), which provided the full scholarship for studying in the master program and National Metal and Materials Technology Center (MTEC), for providing laboratory equipments and instruments as well as financial support.

Moreover, I would like to thank to all laboratory's members for helping me during the experiment and helpful for discussion.

Finally, I am very grateful to my family for all love, caring, understanding and motivation throughout my life.

Jittrabhanu Lamlerttham

CONTENTS

CONTENTS (CONT.)

CONTENTS (CONT.)

LIST OF TABLES

LIST OF FIGURES

LIST OF FIGURES (CONT.)

LIST OF FIGURES (CONT.)

LIST OF FIGURES (CONT.)

LIST OF FIGURES (CONT.)

Figure Page

LIST OF FIGURES (CONT.)

CHAPTER 1

INTRODUCTION

1.1 Significance and Background

Metal injection molding (MIM) is a one of powder metallurgical process used for manufacturing small and complex components (Ho *et al.*, 2008; Ye *et al.*, 2008; Yimin *et al.*, 1998; Zaky, 2004). MIM process comprises four steps of (1) mixing, (2) injection molding, (3) debinding and (4) sintering. Feedstock is a mixture of powder and binder which temporary packing powder into desired shape and hold that shape then debinded in debinding step. In molding step, the feedstock is heated and injection molded into the mold by injection molding machine. After molding, the binder is removed from the molded specimen by debinding process. The final step is sintering, which is usually processed at temperatures near melting for the material (German, 1990). Sintering bonds between powder particles together and increases densification due to shrinkage as pores are reduced or eliminated (Loh *et al.*, 2001; Moballegh *et al.*, 2005). After sintering, the specimen has excellent strength, hardness, and other mechanical properties (Loh *et al.*, 2001). MIM process has advantages of producing parts of complex shapes, high performance and eliminating machining or other secondary operations (Fujiki, 2001; Jigui *et al.*, 2010; Li *et al.*, 2009; Ye *et al.*, 2008). Nowadays MIM is widely used for manufacturing automotive parts such as components in fuel system, engine, power train, electrical system, brake system and etc. (Fujiki, 2001; German, 1990; German, 2001). Many of these applications require demanding mechanical properties due to high temperature and pressure operating. Therefore, high strength and wear resistant materials are required.

Tungsten heavy alloy has high density, wear resistance, hardness, strength, ductility and conductivity. It has the highest melting point (3422°C) of all metals (ASM Handbook, 1984) and also has excellent mechanical properties and the low expansion coefficient (Ho *et al.*, 2008; Hong *et al.*, 2003; Qu *et al.*, 2001; Zu *et al.*, 1997). Due to its high melting point, difficultly machining and high cost of machining for complex shaped parts. The solutions of these problems can be provided by MIM process.

During sintering process, one of crucial MIM steps, sintering temperature and sintering time are important factors having strongly influences on mechanical properties of sintered parts (Ye *et al.*, 2008).

Therefore, the effects of sintering conditions of W-(Ni-Cu-Co) specimens on density, microstructure and mechanical properties were investigated in this work.

1.2 Objectives

1.2.1 To optimize debinding process time.

1.2.2 To study the effects of sintering temperature and sintering time on mechanical properties.

1.2.3 To understand the effects of long sintering times.

1.2.4 To investigate the effects of sintering atmosphere on density and mechanical properties.

1.3 Scopes

1.3.1 The first part was to study the suitable parameters for injection molding such as mold temperature, molding pressure and nozzle temperature.

1.3.2 The second part was on debinding time.

1.3.3 The third part was on sintering conditions by varied sintering temperatures and sintering times.

1.3.4 The final part was to examine density, shrinkage, hardness, tensile properties and microstructure.

1.4 Expected Benefits

1.4.1 Understanding the processing method of metal injection molding by using tungsten heavy metal.

1.4.2 Understanding the effects of sintering conditions on physical and mechanical properties.

CHAPTER 2

THEORY AND LITERATURE REVIEWS

2.1 Introduction to Metal Injection Molding (MIM)

A new technology known as powder injection molding (PIM) or metal injection molding (MIM) uses the shaping advantages of injection molding but is applicable to metals and ceramics. This process combines a small quantity of a polymer with an inorganic powder to form a feedstock that can be molded. After molding, the binder is extracted and the powder is sintered, often to near-theoretical densities (German and Bose, 1997).

The significant advantages of MIM process are the ability to produce complex or geometry parts, near-net shapes processing, good surface finishes, enable production of low cost (Huang *et al.*, 2003; Moballegh *et al.*, 2005; Ye *et al.*, 2008), applicability to several materials, high final properties (ASM International, 1998), eliminating machining and other processing steps (German, 1994; German, 2001). MIM process, which is shown in **Figure 2.1**, comprises four stages of (1) mixing, (2) injection molding, (3) debinding and (4) sintering.

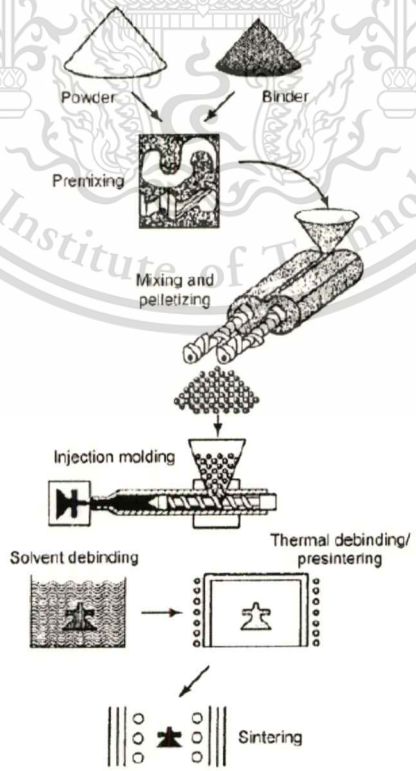

Figure 2.1 Metal Injection Molding Process (ASM International, 1998).

2.2 Process of MIM

2.2.1 Feedstock

Feedstock, which is shown in **Figure 2.2**, represents a balanced mixture of powder and binder. Metal powder is mixed with minimum amount of a binder, which provides the necessary rheological properties for injection molding. The mixture must be homogenous and free from agglomeration (Moballegh *et al.*, 2005). The ratio of powder to binder largely determines the success or failure of subsequent process (Setasuwon *et al.*, 2003). Three possible situations are shown in **Figure 2.3**. Too little binder results in a high viscosity and trapped air pockets that make for molding difficulties. As the binder concentration is decreased, a critical composition is encountered beyond which the viscosity is very high and voids form in the mixture. Most feedstocks are formulated with slightly less powder than the critical solids loading. The critical solids loading is the composition where the particles are packed as tightly as possible without external pressure and all space between the particles is filled with binder. With more powder (less binder) there is insufficient binder to prevent voids which leads to difficult molding (German and Bose, 1997). Mixing of powder and binder is an important step (Piotter *et al.*, 1997; Zeep *et al.*, 2007), the uniformity of the mixture influences the flow behavior of the feedstock and the sintered parts (Suri *et al.*, 2003).

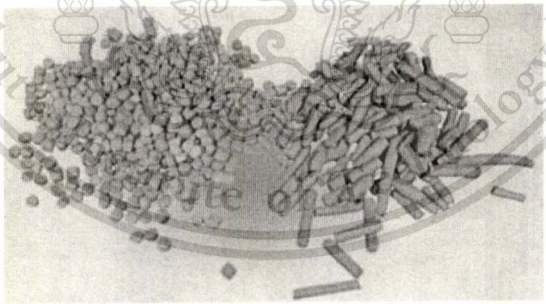

Figure 2.2 Feedstock for injection molding (ASM International, 1998).

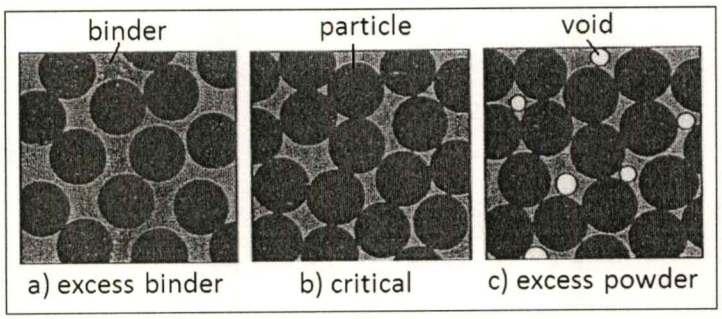

Figure 2.3 Three possible situations of feedstock (German and Bose, 1997).

2.2.1.1 Metal Powder

Particle size and size distribution have a significant effect on the behavior of metal powders during processing. A particle is the smallest unit of a powder that cannot be subdivided by simple mechanical means. Agglomeration is a common problem with small particles, so some work is needed to break apart agglomerates. The scanning electron microscope (SEM) is the best tool available for observing the discrete characteristics of a particle. **Figure 2.4** shows a scanning electron micrograph of powder suitable for MIM. There are many variations in particle size and shape, but the particles generally are equiaxed, rounded and below 20 μm in size. They pace to densities between 30 and 80% of theoretical, but most typically pack to about 60% density. Spheres pack to 60 to 64% density, but non-spherical shapes are less efficient. A wide particle size distribution aids packing since the small particles fit between the large particles, but this distribution proves more difficult to handle and is prone to separation in molding (German and Bose, 1997).

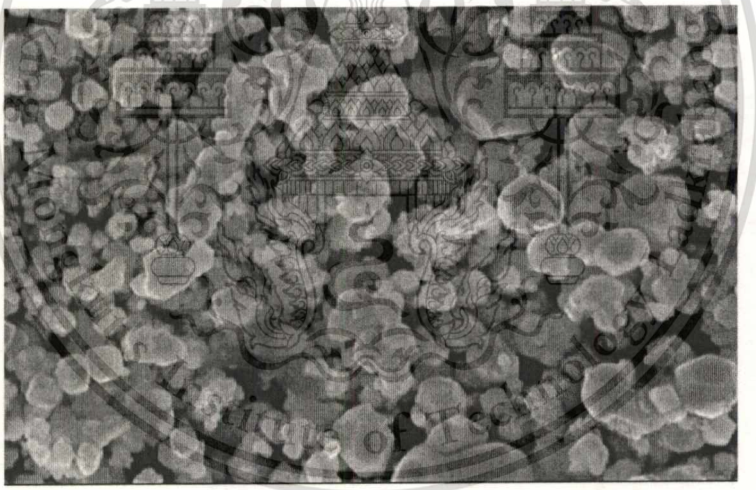

Figure 2.4 Scanning electron micrograph of a typical powder used in MIM (Ho *et al.*, 2008).

The more irregular the particle shape, the greater the number of parameters that are necessary to size a particle. Because of the difficulty in quantifying particle shape, qualitative descriptors are used. These are usually based on SEM observations. **Figure 2.5** gives a collection of scanning electron micrographs showing the range of particles shapes.

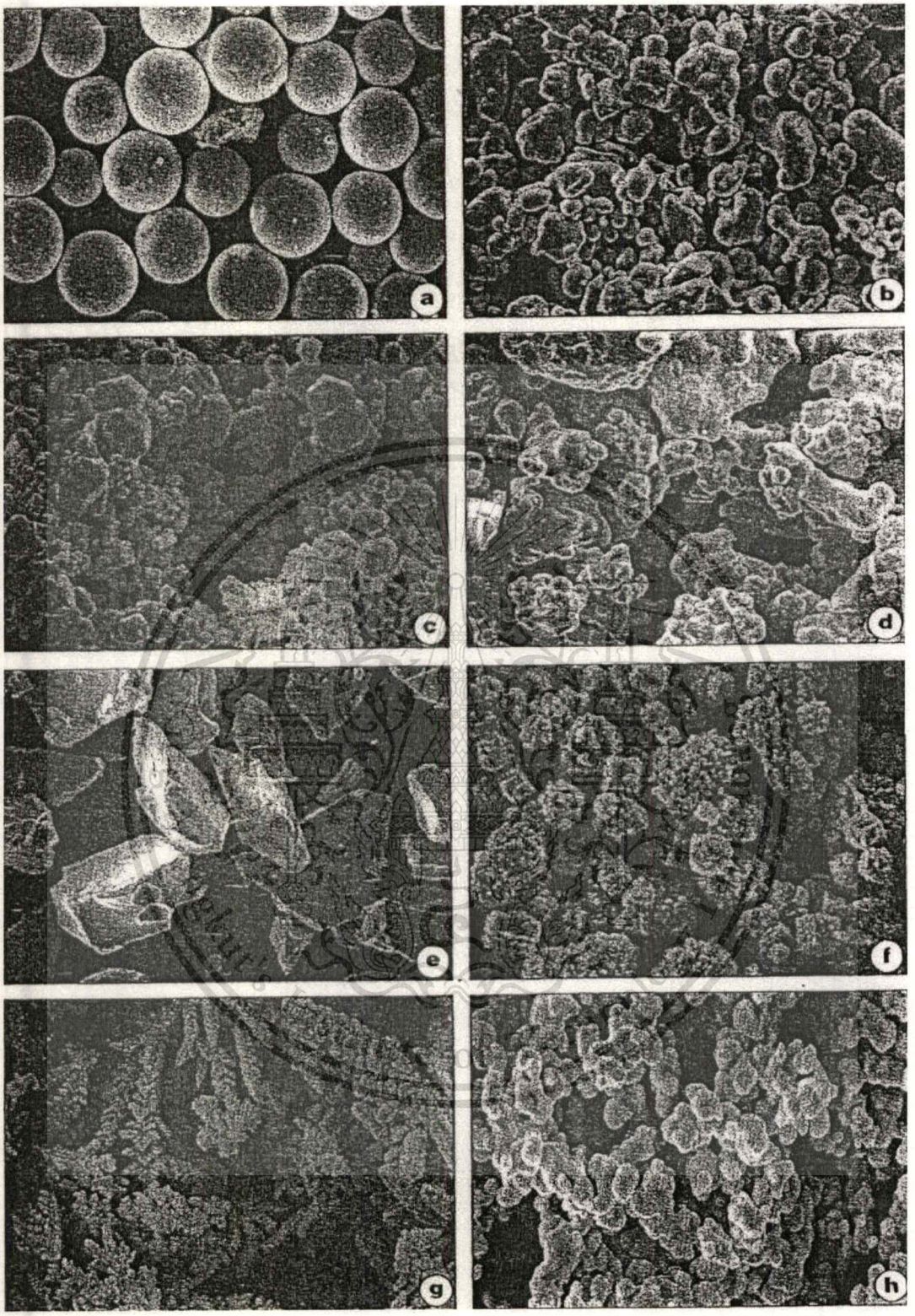

Figure 2.5 Scanning electron micrographs of various MIM powders. Qualitative particle shape descriptors prove useful in describing particle shape a) spherical, b) ligamental, c) agglomerated cubes, d) irregular, e) angular, f) spiky, g) dendritic and h) spongy (German and Bose, 1997).

Irregular particles increase the component strength after binder removal, but lower the packing density and raise the mixture viscosity and sintering densification. Spheres are desirable because of their higher packing density, lower flow viscosity, and isotropic sintering densification. Nevertheless, spheres reduce the component strength after binder removal. **Table 2.1** provides a summary of the advantages and disadvantages (German, 1990).

Table 2.1 Characteristic of powder and their effects on MIM (German and Bose, 1997).

	Advantages	**Disadvantages**
Small particle size	- Faster sintering - Smaller molding defects - Shape retention	- Slower debinding - Greater expense - More contamination - More sintering shrinkage - Higher mixture viscosity - More agglomeration
Spherical shape	- Higher packing density - Lower mixture viscosity - Improved flow	- Lower strength - Slumping during debinding
Wide distribution	- Higher packing density - Less sintering shrinkage	- More quality problems - Inhomogeneous microstructure - Slower debinding - More prone to size segregation

2.2.1.2 Binder

The binder is mixed with the powder to form feedstock for molding. It influences all aspects on MIM (Setasuwon *et al.*, 2003). Most binders are multiple-component systems that contain the basic properties along with several modifiers added to suit the particular application. A multiple component binder is beneficial in allowing removal via a progressive extraction cycle. The binder must wet the powder and provide low viscosity at a high solids loading. The attributes of an ideal binder are listed as follows:

- A mixture viscosity in the 20 to 200 Pa•s range.
- Small molecule to fit between particles and void.

- Low viscosity change with temperature during molding and rapid change in viscosity during cooling.

- Low contact angle, chemically passive and adherence to powder.

- Thermally stable during mixing and molding.

- Noncorrosive and nontoxic.

- High strength, stiffness, lubricity and thermal conductivity.

- Low thermal expansion coefficient.

- Inexpensive and available

Many binder systems are used in MIM operations. Part of this variation reflects the subtle differences in powder characteristics and debinding techniques. A general classification shows at least five types of binders used in MIM, most of which are polymers. There are categorized as follows:

1. Thermoplastic compounds
2. Thermosetting compounds
3. Water-based systems
4. Gelation systems
5. Inorganics

Thermoplastic and thermosetting compounds are the two general forms of polymer most commonly used in MIM. The thermosetting polymers form cross-links upon heating and become permanently rigid. They do not soften on reheating but decompose at high temperature. On the other hand, thermoplastics are essentially thermally reversible. They soften on heating and harden on cooling. Low-molecular-weight polymers or waxes are the usual base for a binder. Short-chain-length molecules are easier to mix and remove in debinding.

Mechanical properties of polymers depend on test condition. At low temperature the polymer is brittle. At high temperature it is flexible. **Table 2.2** provides a summary of room temperature properties for some common binder constituents (German and Bose, 1997).

Table 2.2 Approximate properties of common polymer employed as binder constituents (German and Bose, 1997).

PP = polypropylene

PE = polyethylene

PS = polystyrene

PVC = polyvinyl chloride

PW = paraffin wax

PEC = polyethylene carbonate

PEG = polyethylene glycol

MW = microcrystalline wax

Property	**PP**	**PE**	**PS**	**PVC**	**PW**	**PEC**	**PEG**	**MW**
Density, g/ cm^3	0.90	0.91	1.04	1.35	0.91	1.42	1.15	0.80
Melt temperature, °C	150	170	180	180	60	-	65	70
Melt density, g/ cm^3	0.77	0.8	0.9	1.25	0.7	1.1	-	-
Thermal conductivity, W/m/°C	0.2	0.3	0.1	0.2	0.3	0.2	-	-
Thermal expansion, K	100	200	70	140	400	-	740	-
Tensile strength, MPa	35	10	50	20	4	2	nil	0.5
Failure elongation, %	200	400	2	300	-	1000	nil	2

Suri *et al.* (2003) concluded about the effect of mixing on the rheology of 97%W-2.1%Ni-0.9Fe feedstock that feedstock composed of agglomerated powder has lower packing fraction and higher viscosity compared with deagglomorated powder. In addition, a homogenous feedstock exhibits lower viscosity and higher flow stability.

Yimin *et al.* (1998) investigated the rheological properties of 97W-2Ni-1Fe feedstock. The powder loadings were 45, 47, 50 and 55 (volume fraction, %). They reported that the viscosity of the feedstock decreased with the increase of shear rate and the increase of temperature. They also suggested that the viscosity of MIM feedstock should decreased quickly with increasing shear rate during injection process. This high shear sensitivity is important for producing complex parts. The results showed that the mechanical properties first increased with the powder loading and achieved the highest at 47% powder loading then decreased with further increase of the powder loading. From the microstructure results, it was observed that the grain size increased from 40 to

80 μm when powder loading increased from 47 to 55%. This was the main cause of the decreased in the mechanical properties.

2.2.2 Injection Molding

Feedstock is injection molded into the desired shape by heating it in the molding machine and injecting it under pressure into the tool cavity. By virtue of the binder, the feedstock becomes low enough in viscosity that it can flow into the die cavity under pressure. Cooling channels in the die extract heat and solidify the polymer to preserve the molded shape. High-volume injection molding uses a horizontal reciprocating screw located inside a heated barrel. The screw is designed to compress and transport the feedstock to the die, and it becomes a plunger during mold filling. **Figure 2.6** is a typical layout of a horizontal machine. The tooling is clamped in the center of the machine. The granulated or pelletized powder-binder feedstock is placed in the hopper for metering into the injection barrel. This is the beginning of the molding operation.

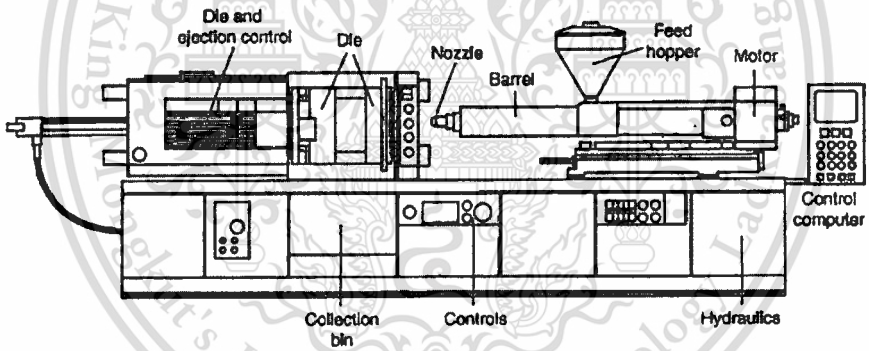

Figure 2.6 Overview of a horizontal injection molding machine (ASM International, 1998).

During the molding cycle, the screw initially rotates, compressing the feedstock. Then, during the injection step, the screw moves forward, closing the check ring, and the shot is injected into the mold. During the fill stroke, the volume of feedstock injected into the mold depends on the cross-sectional area of the screw and on the stroke length. In the typical tool set, the feedstock flow path is from the molding machine nozzle into the sprue, along the runner, through the gate, and into the mold cavity. Feedstock flow in molding depends on the applied pressure and viscosity. For a cylindrical runner, the volumetric feedstock flow rate, Q, varies with the runner diameter, D, to the fourth power according to Poiseuille's equation:

$$Q = \frac{P\pi D^4}{128\eta L} \quad (2.1)$$

where P is the applied pressure on the feedstock, L is the runner length, and η is the feedstock viscosity.

After molding, the component is cooled in the die cavity. Cooling causes the binder to contract and this results in a progressively lower pressure. For ejection, pins move from flush positions on the tool walls and push against the component to extract it from the cavity (ASM International, 1998).

Moballegh *et al.* (2005) studied effects of injection molding parameters. From the TGA result, binder degradation starts at 170°C, thus the injection molding temperatures must be lower than this temperature. The injection molding results showed that the injection below than 160°C was not successful. Defect-free green parts were obtained at the injection temperature of 160°C with the mold temperature of 50-60°C and injection pressure of 5.5-6 bar.

Jigui *et al.* (2010) studied the injection molding process of W-20wt%Cu. From the DSC result, they suggested that the minimum injection temperature should be higher than the melting temperature but lower than decomposition temperature of the binder. The injection molding results showed that the weight of the green parts increased as the injection pressure increased from 90 to 110 bars but decreased when the pressure was higher than 110 bar because injection pressure induced severe stresses in the part and caused cracks. Defect-free parts of W-20wt%Cu were obtained at the suitable injection parameters with injection pressure of 110 bars, injection speed of 30% (of the standard injection speed), injection temperature of 180°C and mold temperature of 50°C.

Huang *et al.* (2003) investigated the injection molding factors which influence the rheological of behaviors of the feedstock, i.e. MA milling time, powder loading, and injection temperature. **Figure 2.7** illustrates the viscosity variation of the W-Ni-Fe feedstock with powder loading of 51vol.% with shear rate at temperature of 120, 135 and 150°C. They concluded the effect of temperature on rheological behavior that the viscosity decreases as temperature increases (as shown in **Figure 2.7**). The difference in viscosity is large at lower shear rate. With increase of shear rate and temperature, the difference in viscosity becomes small. This indicated that the viscosity is more sensitive to shear rate at lower temperature.

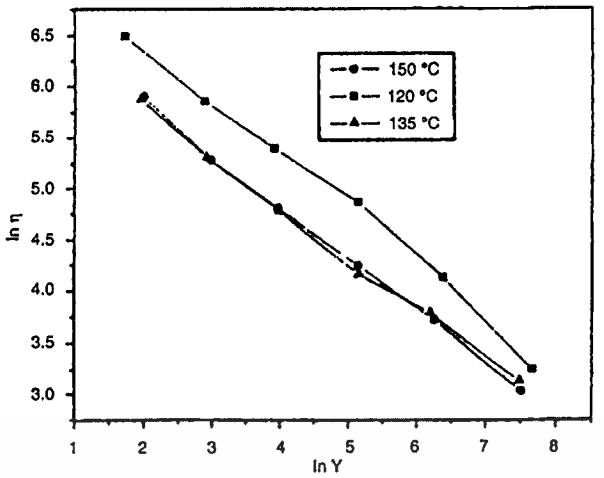

Figure 2.7 Variation of the viscosity of the feedstock with shear rate (Huang *et al.*, 2003).

2.2.3 Debinding

After molding, the binder must be removed from molded specimen and the binder becomes a disposable. (ASM International, 1984) Failure to remove most the binder before sintering can result in component distortion, cracking and contamination. Removing the binder without disrupting the particle is a delicate process that is best achieved in multiple steps. When the binder is removed, the component becomes very fragile until sintered, though it must be strong enough to retain its shapes.

There are several debinding techniques, categorized as thermal and solvent debinding processes (Loh *et al.*, 2001). These are shown in **Figure 2.8**. Thermal debinding perhaps the most commonly used technique, which is often very slow and debinding duration of several days are not uncommon, while in solvent debinding, the binder is removed by dissolving one or more binder component with significantly faster speed (Loh *et al.*, 2001; Setasuwon *et al.*, 2008; Zaky, 2004). As illustrated by **Table 2.3**, many variants exist. The measured rates are compared on an equivalent basis of 5 m steel powder and 10 mm section thickness (German and Bose, 1997).

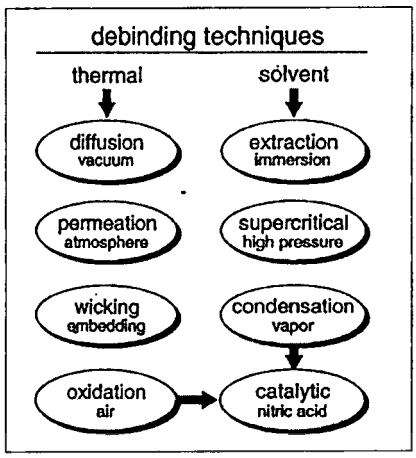

Figure 2.8 Classification of the debinding processes (German and Bose, 1997).

Table 2.3 Comparison of debinding techniques and times (ASM International, 1998).

Binder system	Debinding technique	Condition	Time
Wax-polypropylene	Oxidation	Slow heat 150 °C, hold, heat to 600 °C in air	60 h
Wax-polyethylene	Wicking	Slow heat 250 °C, hold, heat to 750 °C in hydrogen	4 h
Wax-polymer	Supercritical	Heat in Freon vapor at 10 °C/min to 600 °C under 10 MPa pressure	6 h
Wax-polyethylene	Vacuum extraction	Slow heat while passing low-pressure gas over compacts, heat to sintering temperature	36 h
Water-gel	Vacuum sublime or freeze dry	Hold in vacuum to extract water vapor from ice	8 h
Oil-polymer	Solvent immersion	Hold in ethylene dichloride at 50 °C	6 h
Water-gel	Air drying	Hold at 60 °C	10 h
Polyacetal-polyethylene	Catalytic debinding	Heat in nitric acid vapor at 135 °C	3

2.2.3.1 Thermal Debinding

The classic debinding cycle uses slow degradation of a wax-based binder in air. The component is slowly heated to decompose the binder. A typical cycle involves slow heating in a circulating air furnace to a temperature between 100 and 200°C. This temperature is below the melting temperature of the backbone polymer. Oxidation is continued for times up to 60 hours to

remove at least 40% of the binder. The binder permeates through the surface connected pores as shown in **Figure 2.9**. The second stage of debinding involves heating to a presenter temperature under a neutral or reducing atmosphere (hydrogen, nitrogen or argon) to thermally decompose the remaining binder.

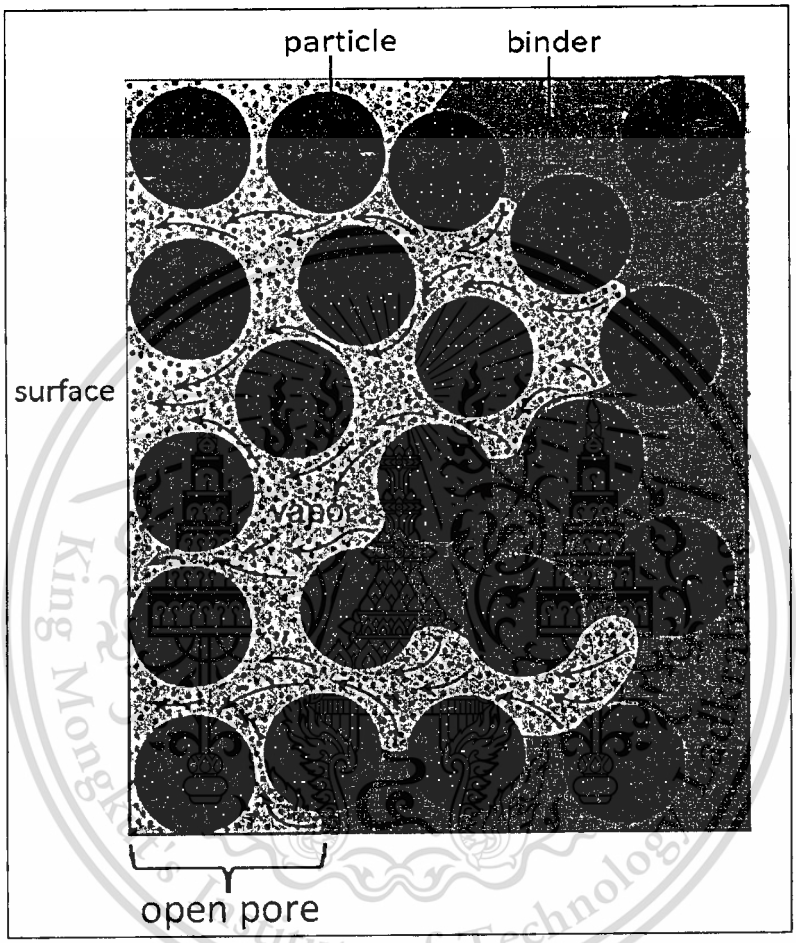

Figure 2.9 A model pore geometry showing a point in time during thermal Debinding where the binder is permeating to the component surface through open pores from an interface source in the pore structure (German and Bose, 1997).

The classification of thermal debinding are

- Diffusion, the binder can be removed as a vapor during heating under partial vacuum via diffusion through the pores between particles. The mathematics for treating debinding, namely the distance gas molecules move between collisions. In diffusion control, the collisions are mostly with the pore structure. **Figure 2.10** sketches the layout of a vacuum furnace equipped with a

sweep gas inlet and condensation baffles for collection of the vapors before reaching the vacuum pump.

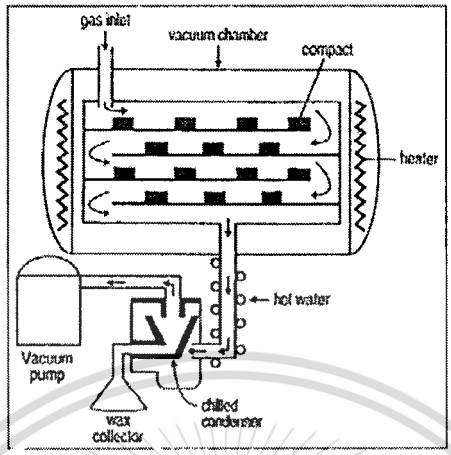

Figure 2.10 Outline of thermal debinding in a vacuum where a gas is used to sweep debinding vapors to a cold trap located in the vacuum pumping system (German and Bose, 1997).

- Permeation, the binder can be removed as a vapor during heating at ambient pressure via permeation through the pores. The difference between diffusion and permeation depends on the binder vapor pressure, which in turn determines the ease of vapor flow through the pores between particles. In permeation control, the collisions are mostly with other gas molecules. As shown in **Figure 2.11**, a batch system for thermal debinding consist of a retort that holds the compacts and contains the atmosphere and various control for time, temperature, pressure and atmosphere.

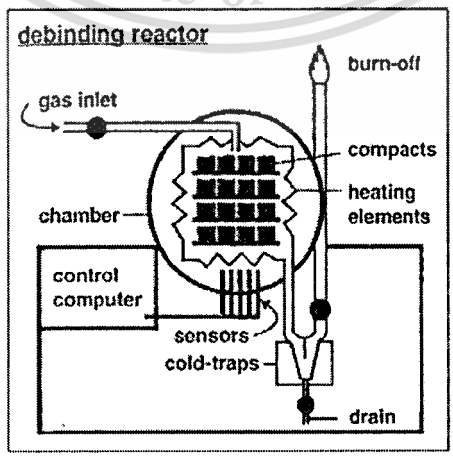

Figure 2.11 A sketch of a batch debinding system consisting of a retort chamber, heating unit, and various control and sensors for optimizing debinding (German and Bose, 1997).

- Wicking, wicking has been applied in several variations and is combined with thermal burnout for many thermoplastic binder systems as shown in **Figure 2.12.** Typically the binders used for wicking debinding contain wax, which is preferentially extracted using either an embedding powder or a porous substrate. Wicking is carried out at a temperature where the binder melts, allowing it to flow out of the component into pores in the contacting substrate. If the wicking material has a pore size smaller than the component, then very rapid debinding is possible. However, not all binder can be fully extracted by wicking because of the irreducible saturation.

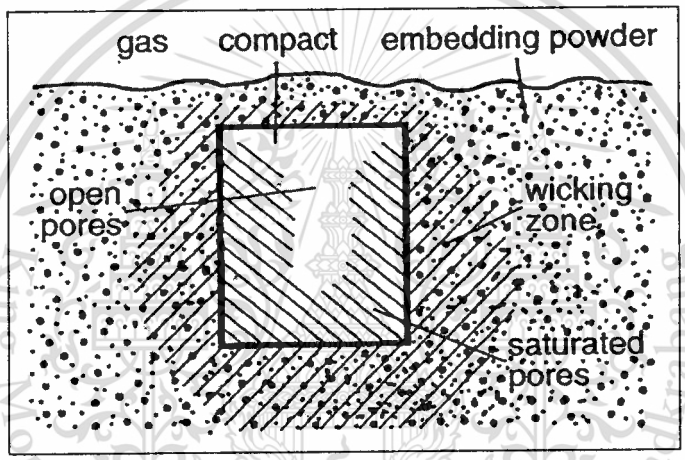

Figure 2.12 Illustration of wicking debinding with an embedded part in a low density powder with a small pore size (German and Bose, 1997).

Loh *et al.* (2001) studied the effects of thermal debinding parameters, i.e. heating rate, debinding temperature and debinding time. The debinding temperature was based on the TGA curve for the binder. Slow debinding rate were necessary to avoid excessive pressure build-up. Using too fast a heating rate causes vapour pockets to be built up by the internal pressure, resulting in flaking and blistering. The defect-free parts were obtained when the debinding time for 24 hours was employed.

2.2.3.2 Solvent Debinding

Solvent extraction is widely employed with oil-polymer binder systems. The solvent is selected to dissolve the oil but not the polymer. To allow handling after stage debinding, the oil

and polymer should be insoluble in each other. Initially, the component is immersed in the solvent to extract the oil.

The classification of solvent debinding are

- Solvent Immersion, solvent extraction by immersion or exposure to solvent vapors, requires that some binder be insoluble on the solvent. Thai process is applied to binder mixtures such as polypropylene and vegetable oil or polystyrene, polyethylene and vegetable oil. The solvent is heated to increase the rate of oil extraction as shown in **Figure 2.13**. The binder must not swell from absorption of the solvent. After immersion, the insoluble portion of the binder holds the particles together while the component is dried. The backbone polymer is subsequently removed by thermal degradation. Also, rapid drying after removal from the solvent causes surface cracks due to drying stresses.

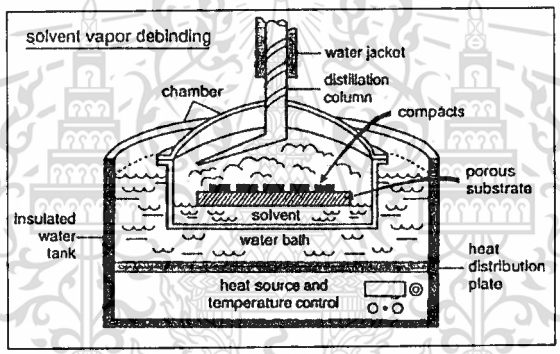

Figure 2.13 Solvent vapor debinding is performed in a vapor generated by a heated solvent, typically generated by a water bath. The vapor condenses on the MIM components and migrates back to the vapor source with dissolved binder (German and Bose, 1997).

- Catalysis, catalytic debinding is a hybrid between thermal and solvent debinding. The reaction depends on permeation of the catalyst vapor into the pores and permeation of the decomposition product out of the pores. These occur in nitrogen at atmospheric pressure as shown in **Figure 2.14**. The reaction temperature and catalyst concentration determine the debinding rate. A backbone polymer that is unaffected by the catalyst provide handling strength after the catalysis event. Debinding is performed in special reactors that ensure proper acid feed rates and proper nitrogen flow rate. After extraction, the remaining binder is burnt out as part of the sintering cycle.

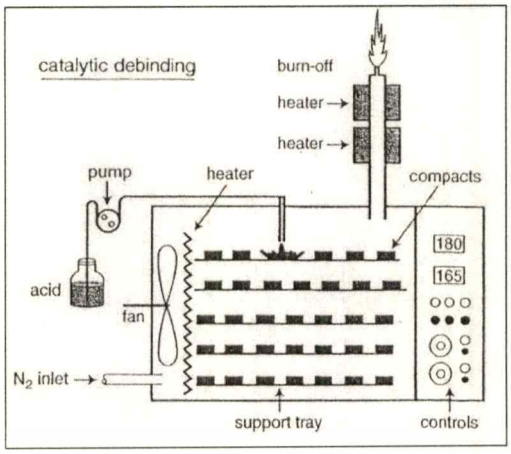

Figure 2.14 Catalytic debinding is performed in a sealed oven that allows a nitrogen process gas with the addition of the depolymerization catalyst (German and Bose, 1997).

Debinding is highly variable as to binder system, technique, and section thickness. **Table 2.4** provides a summary of the key aspects of each process.

Table 2.4 Contrast and comparison of debinding approaches (German and Bose, 1997).

Debinding technique	Key features	advantages	disadvantages
Solvent immersion	Place component in solvent to selectively extract major binder phase via dissolution.	Component remains rigid without chemical reaction, open pore channels for subsequent easy degradation of binder	Solvent hazard, chemical handling and environmental concerns, drying required prior to heating or sintering.
Supercritical extraction	Heat and pressurize fluid above critical point to dissolve binder into fluid.	No phase change and minimized defect formation.	Requires precise temperature and pressure control, slow rate.
Solvent vapor condensation	Hold compact in heated vapor of solvent and allow condensation to adsorb major binder phase, dripping off to	Low component temperature minimizes defects and distortion, with replenished surface solvent aiding	Chemical, environmental and health concerns with solvent vapor, condensation and

	replenish surface solvent.	rapid debinding.	recovery, drying required prior to heating.
Catalytic depolymerization	Heat compact in atmosphere containing catalyst to continually depolymerize and sweep away polymer.	Rapid process that works on both thick and thin sections with excellent shape retention and high automation.	Hot mold, possible hazard with special acid catalysts and decomposition product.
Diffusion controlled thermal	Slowly heat com pact in a low pressure system with continual sweep gas to remove molten and vapor product.	One step process eliminates handling between Debinding and sintering.	Soft binder allows warpage, expensive equipment, slow extraction rates, possible contamination of parts and furnace.
Permeation controlled thermal	Pass process gas over compact as it is slowly heated to give progressive degradation of binder	Low cost installation, widely used process, no solid or liquid waste.	Poor dimensional control and relatively slow process with possibility of contamination during heating.
Wicking	Heat component in packed powder bed or on porous substrate that absorb molten binder.	Fast initial rates, applicable to wide range of binder, easy to master.	Distortion possible due to multiple handling steps, binder disposal problems, separation of part from wick.
oxidation	Heat component on air to simultaneously burn out binder and oxidize powder to give strength.	High strength after Debinding, effective in removing carbon.	Low residual carbon, slow process, only applicable to low stability metals and oxides, possible exothermic reaction.

Li *et al.* (2009) studied the processing steps of metal injection molding of pure molybdenum, including solvent debinding process. They found that a higher efficiency of the binder removal was achieved as the debinding temperature increased due to larger solubility and diffusivity. The debinding rate was decreased when the debinding time increased. Similar results were also observed by Jigui *et al.* (2010). The results showed that the debinding rate increases as the solvent temperature rises and the weight loss of the binder remains nearly unchanged after 11 hours because the equilibrium of solution binders between the samples and the solvent.

2.2.4 Sintering

The next step is sintering, which can be incorporated directly into a thermal debinding cycle. Sintering bonds the particles together and reduces the void spaces, leading to densification, so high linear shrinkage of 10–20% takes place in the specimens (Moballegh *et al.*, 2005) Usually sintering shrinkage is uniform and isotropic, so the molded component is oversized to deliver the desired final dimensions. For metals, sintering is performed in a protective atmosphere or vacuum at a peak temperature that causes rapid elimination of the pores that were previously filled with binder (ASM International, 1998). Sintering densification usually occurs close to the melting temperature for the material. The bonds between particles grow by the motion of individual atoms via either solid-state or liquid-phase events. **Figure 2.15** is a scanning electron micrograph of the neck formed between sintering particles. The resulted density can reach over 97% of the theoretical value, depending on the powder properties like initial density and type of material and also sintering conditions such as atmosphere, temperature, heating rate and sintering time.

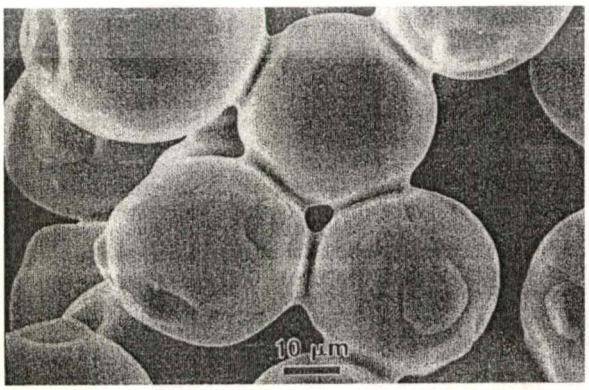

Figure 2.15 Scanning electron micrograph of the initial stage sintering between spherical particle with necks growing at the contact points (German and Bose, 1997).

2.2.4.1 Basic Mechanisms

The important driving force for sintering is the stress associated with a curved surface. This surface curvature, and the associated high surface area of small MIM particles, provides the motivation for sintering. At the microscopic level, sintering occurs because atoms move to fill the pores between particles. In eliminating the pores, mass flows along particle surfaces (surface diffusion), across pore spaces (evaporation-condensation), along grain boundaries (grain boundary diffusion) and through the lattice interior (viscous flow or volume diffusion). The atoms take many paths to form the bonds as shown on the three particle geometry in **Figure 2.16**. These paths include atomic diffusion through the crystals, along the grain boundaries, and over free surface. The rate of neck growth, shrinkage and densification all depend on the cumulative rates of transport by these various paths.

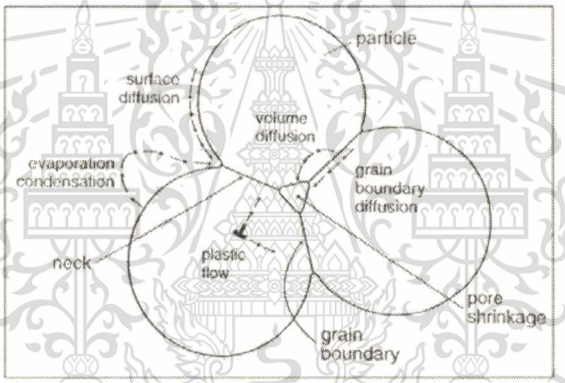

Figure 2.16 Three particles in contact with sinter necks growing. The various transport possibilities are shown to indicate the possible mechanisms of sinter bonding (German and Bose, 1997).

A grain boundary is the region of crystal disruption where two particles come together. Grain boundaries play a vital role in sintering, since atomic transport is faster along these defective regions. Thus, sintering is enhanced by retention of small grain sizes (high grain boundary contents) and small pores attached to the grain boundaries.

So, during sintering, the initially loose-powder compact undergoes a transformation to become a dense, polycrystalline structure with physical and mechanical properties similar to other material. A structural change during sintering process probably similar to that shown in **Figure 2.17**. The final stage of sintering has a few small pores sitting on grain boundaries.

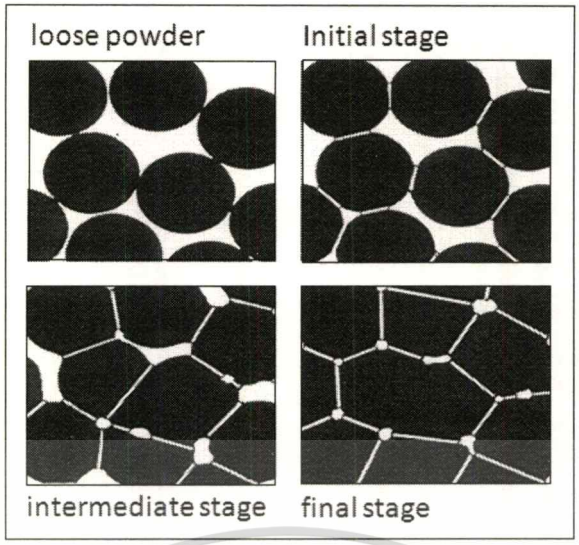

Figure 2.17 Microstructure evolution in MIM sintering involves the initial bonding of the particles, followed by pore rounding and grain growth by the final stage (German and Bose, 1997).

2.2.4.2 Effects of Sintering on Dimensions and Properties

Dimension change is inherent with sintering densification. For many MIM powder, however, it proves necessary to measure the dimensional change versus time or temperature to identify a process cycle. The linear dimensional change, designated as shrinkage $\Delta L/L_0$. It is the change in a compact dimension (ΔL) divided by the initial dimension (L_0). Density and shrinkage are interrelated. In MIM, isotropic shrinkage is assumed in sintering, where the compact densifies from the initial green fractional density ρ_G (after debinding) to the sintered density ρ_S as follows:

$$\rho_S = \frac{\rho_G}{\left(1-\frac{\Delta L}{L_0}\right)^3} \tag{2.2}$$

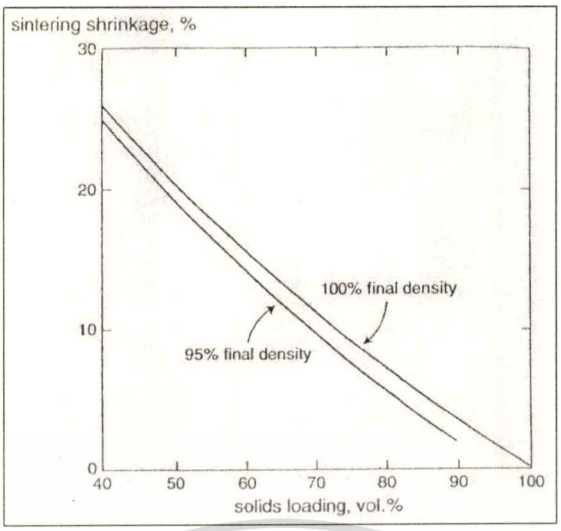

Figure 2.18 Shrinkage as a function of the initial solids loading for two final sintered densities (German and Bose, 1997).

Figure 2.18 plots this relation to show the shrinkage as a function of green density (as a percent of the theoretical) for two final density levels, 95 and 100%.

Pore elimination is a typical concern in attaining maximum properties. Higher sintering temperature and smaller particle sizes help in obtaining high sintered densities. Consequently, the mechanical and other properties of MIM compact are improved. The strength increases due to better sinter bonding and improved distribution. Generally, higher strengths result from higher sintering temperatures and similar trends are evident in most engineering properties. Other adjustments in mechanical properties are possible by control of the carbon level in the sintered material via the sintering atmosphere. For example, yield strength varies from 190 MPa at 0.0% retained carbon to 300 MPa at 0.8% retained carbon for Fe-2Ni sintered at 1250 °C.

2.2.4.3 Sintering Furnace and Atmospheres

The sintering furnace provides the time-temperature control of the sintering cycle while containing the process atmosphere. The furnace performs these functions in either batch (discontinuous) or continuous mode. A batch furnace, such as shown in **Figure 2.19**, is loaded with the material to be sintered and is heated to temperature following a predetermined cycle. Batch furnaces have lower productivity in contrast with continuous furnaces. The main advantage of a batch furnace comes from its flexibility. Containment of a vacuum is only possible in a batch furnace. Batch furnaces also provide options for special cycles and small production quantities.

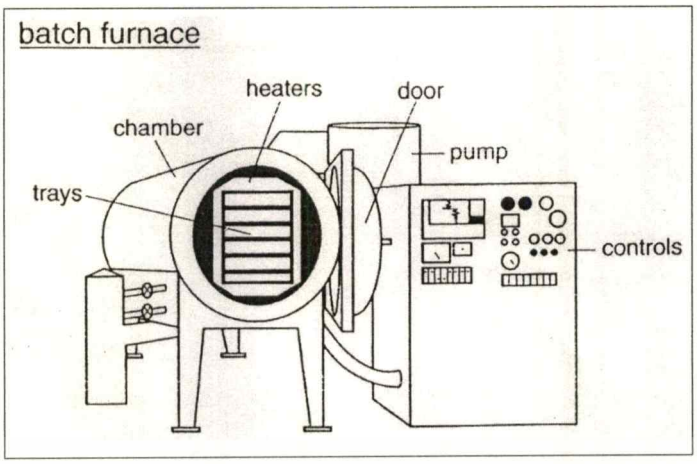

Figure 2.19 A sketch of a vacuum batch-sintering furnace with a front-opening door (German and Bose, 1997).

A continuous sintering furnace provides the desired thermal treatment by controlling the position of the component in preheated furnace. **Figure 2.20** shows a typical layout. In these furnaces, the parts are moved through multiple heating zones by a conveyor such as a belt, pusher, lifting beam or roller assembly.

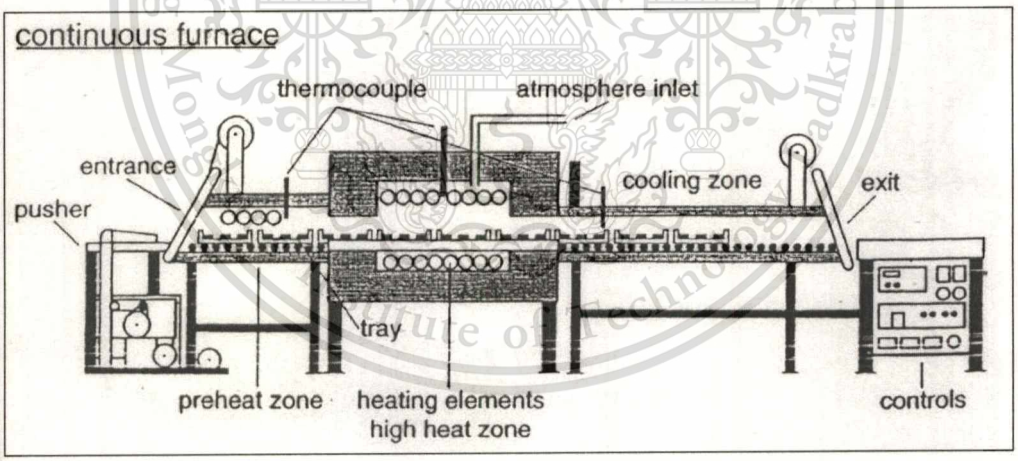

Figure 2.20 A side view through a pusher furnace as applied to the continuous production of sintered MIM components (German and Bose, 1997).

The first zones in a continuous furnace initiate compact heating and remove the remaining binder. Primary polymer burnout products are encountered in the preheat zones, so atmosphere flow is adjusted to push the vapors toward the furnace entrance. Typically, these zones are 1 to 5 m in length and usually consist of three or four temperature steps. The high heat region controls the actual time, temperature and atmosphere condition associated with sintering. Before entry in

the high heat region, the compact should be fully debinded. Depending on the production rate, the high heat zone ranges from 0.7 to 8 m in length and might consist of up to eight individual temperature zones. Cooling takes place in the last zone, which has a water jacket and the compact is subjected to a high gas flow. Within limited ranges, it is possible to tailor the carbon, oxygen or nitrogen levels during cooling. By selective placement of gas inlets and outlets, each zone of the furnace may contain a different atmosphere, allowing tailoring of the chemical reactions during the sintering cycle.

The sintering atmosphere is contained in the furnace to control reaction during sintering. Additionally, the atmosphere transports heat to the compact. There are three ways to transfer heat – conduction, convection and radiation. Radiation occurs by the emission of light or other electromagnetic radiation from the heating elements. Convection and conduction require a gas phase, so they are not active in vacuum sintering. Once heat is deposited at the component surface, it must be distributed into the component this depend on the thermal conductivity that is reduced by the pores. Many sintering atmospheres are used in MIM are:

- Air is used in the sintering of oxide ceramics. The advantage of air atmosphere is the least expensive but difficult to control moisture and contamination.

- Nitrogen is the protective atmosphere during sintering and it is used in the sintering of nitride ceramics.

- An inert gas, such as argon and helium, atmosphere is neutral and gives little thermo chemical interaction with the compact. It is most useful when sintering reactive materials like titanium. The lack of reduction makes inert gas sintering a poor choice in most applications. Further, since inert gases are insoluble in the sintering material, gas filled pores do not close during sintering.

- Dissociated ammonia is one basis for forming a 75% H_2 – 25%N_2 blend. It is formed by the decomposition of ammonia vapor by the following reaction,

$$2NH_3(g) \longrightarrow 3H_2(g) + N_2(g) \qquad (2.3)$$

The ammonia molecule is split into the hydrogen and nitrogen molecules. The hydrogen supplies for oxide reduction but in some occurrence nitrogen can react to form nitrides and thereby be harmful (German and Bose, 1997).

- Vacuum, sintering in a vacuum is processing at a reduced pressure. The pressure in the sintering chamber might be between 10^{-4} and 10^{-7} atmosphere (10 and 0.01 Pa) pressure. Under controlled condition, it provides a clean and nonreactive environment. Most materials can be sintered in a vacuum.

- Hydrogen is the most proper in terms of reducing. So hydrogen atmosphere is the most favorable in the sintering of stainless steel, but its disadvantages are expensive cost and the efficiency of reduction depends on sintering temperature (German and Bose, 1997).

2.2.4.4 Sintering Temperature and Sintering Time

Temperature is a main parameter causes the atom motion and bond diffusion. Sintering temperature is usually approximately 75% of melting temperature of that material. The difference of sintering temperature contributed to the difference of the mechanical properties. Higher sintering temperature increases the sintered density and properties, but the dimensional change also becomes larger. As the temperature is increased, the rate of grain boundary motion increases. As shown in **Figure 2.21** pores separated from the boundaries because of slower moving than the grain boundaries (German, 1994). Sintering time also affect to the grain size. Longer sintering time increases grain size, because pores separated from the grain edges and bound inside the grain which increases the porosity and decrease the mechanical properties. Pores located on the grain edges can occur from the optimums of diffusion and sintering time. **Figure 2.22** shows the two possible pore-grain boundary configurations during sintering (German, 1994) and **Table 2.5** details some common sintering cycles, giving the initial green density, heating rate, maximum temperature, hold time, sintering atmosphere, support material, and final density (ASM International, 1998).

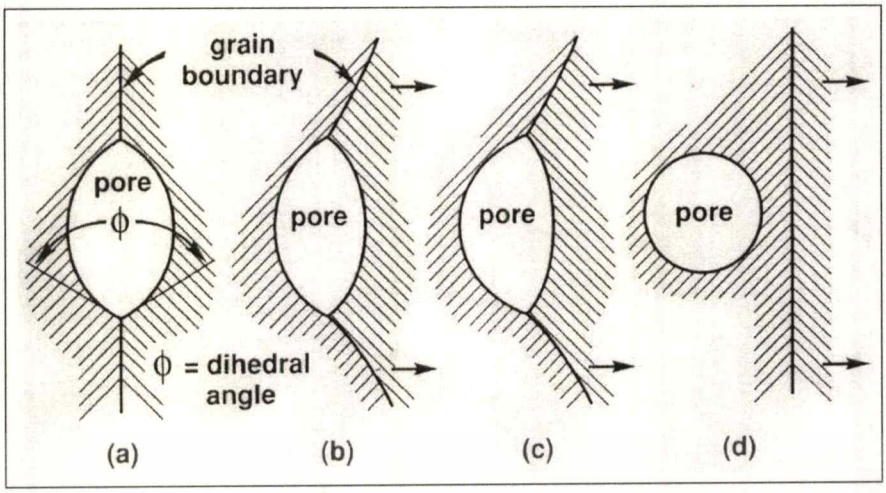

Figure 2.21 The sequence of steps leading to pore isolation and spheroidization in the final stage of sintering; (a) pore on the grain boundary, (b) and (c) correspond to grain growth with pore drag and (d) represents pore isolation because of boundary separation (German, 1994).

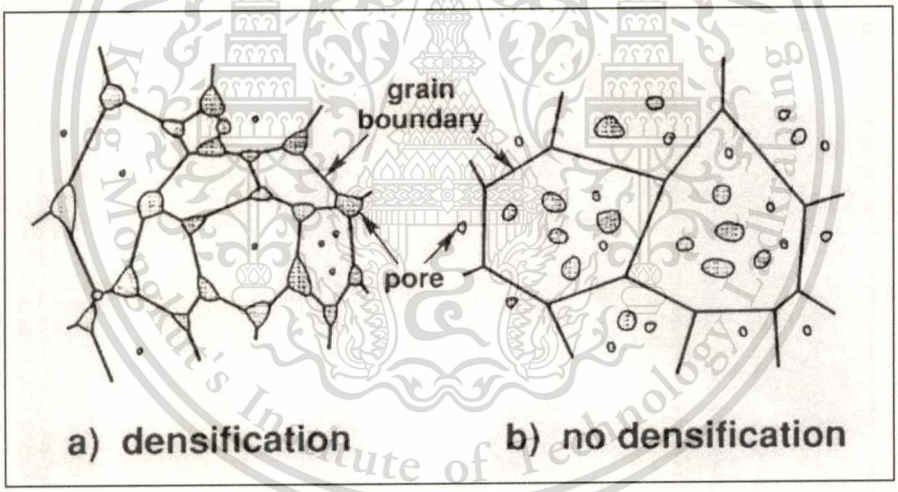

Figure 2.22 Two possible pore-grain boundary configurations during sintering. The pores located on grain boundaries in (a) give densification, while the isolated pores in (b) do not densify (German, 1994).

Table 2.5 Sample of sintering cycles for powder injection molding material (ASM International, 1998).

Material	D, μm	ρ_G, %	dT/dt, °C/min	T,°C	t, min	Atmosphere	Support	ρ_s, %
Ag	90	67	1400	900	60	Hydrogen	Stainless	70
Co-50Fe	5	50	50	1250	120	Hydrogen	Alumina	98
Cu	9	70	10	900	60	Hydrogen	Alumina	94
Fe	5	60	10	1200	60	Vacuum	Alumina	100
Fe-49Co-3V	6	58	5	1350	240	Vacuum	Alumina	96
Fe-2Ni	5	64	15	1250	60	Hydrogen	Alumina	99
Fe-2Ni-0.8C	4	58	4	1200	60	Hydrogen	Alumina	97
Fe-50Ni	5	60	10	1250	60	Hydrogen-nitrogen	Alumina	96
Fe-29Ni-17Co	7	60	10	1250	240	Hydrogen-argon	Alumina	97
Fe-3Si	8	60	10	1350	180	Hydrogen	Alumina	97
Mo-15Cu	9	30	10	1400	60	Hydrogen	Alumina	86
Ni_3Al	14	52	10	1340	60	Hydrogen	Alumina	99
316L stainless	15	62	10	1325	120	Vacuum	Alumina	97
W-10Cu	8	50	10	1350	60	Hydrogen	Alumina	96
W-5Ni-Fe2	2	55	10	1500	30	Hydrogen	Alumina	100

Hong *et al.* (2003) studied two-stage sintering of a 93W-5.6Ni-1.4Fe. When a mechanically alloyed 93W-5.6Ni-1.4Fe was solid-stage sintered at 1300°C for 1 hour, the tungsten particle grains were interconnected to each other and showed high relative density above 99%. When the secondary sintering was performed at a temperature below 1460°C, tungsten particles remained a highly contiguous shape as in a solid-state microstructure. At secondary sintering temperature above 1470°C, tungsten particles were spherical in shape as in a liquid phase sintered microstructure. The matrix volume fraction increased and W-W contiguity decreased with secondary sintering temperature increased. The effect of secondary liquid-phase sintering time on microstructure was also investigated. The results showed that the average size of tungsten particles increased from 6 to 27 μm with increasing secondary sintering time from 4 to 90 minutes.

Ho *et al.* (2008) studied the effect of holding temperature (at 1150, 1200 and 1250°C) on infiltration behavior of W-Cu. They reported that density, shrinkage, hardness, and electrical resistivity increased with the increasing of sintering temperature. Because at higher sintering temperature, the more extensive necking between tungsten particles caused for a greater degree of shrinkage observed and the reduction of porosity within the tungsten matrix for sintered component.

Jigui *et al.* (2010) studied the effect on sintering temperatures on sintering densification of the W-Cu parts. In their work, the brown W-Cu balls were sintered at different temperature (1050, 1100 and 1150°C). The results showed that sintered density of W-Cu samples increased as sintering temperature raised. Relative density of the parts sintered at 1050°C was about 87.37% of the theoretical. But a relative density of 95.58% of the theoretical was achieved when the sintering temperature (1150°C) was above the melting point of Cu (1083°C), there occurred liquid-phase sintering and homogeneous redistribution of W particles.

2.3 Tungsten

Tungsten, also known as wolfram, is a steel-gray metal with the highest melting point of all the metals. Tungsten heavy metal contains 90 to 98 wt% W and composes either copper and nickel or iron and nickel and/or cobalt plus addition elements. The addition of cobalt to a tungsten alloy slightly increases of both strength and ductility. Cobalt additions of 5 to 15% of the nominal binder weight fraction are most common. Tungsten has very high densities, ranging from 16.8 to 18.5 g/cm^3. Tensile strength and Young's modulus are ranging from 760 to 970 MPa and from 270 to 340 Gpa respectively. Tungsten has low thermal expansion coefficients and excellent corrosion resistance. **Figure 2.23** provides a liquid phase sintering microstructure for tungsten heavy metals. A comparison of density and elastic stiffness for various W-(3Ni/Fe) alloys and pure tungsten is shown in **Table 2.6** (German, 1994).

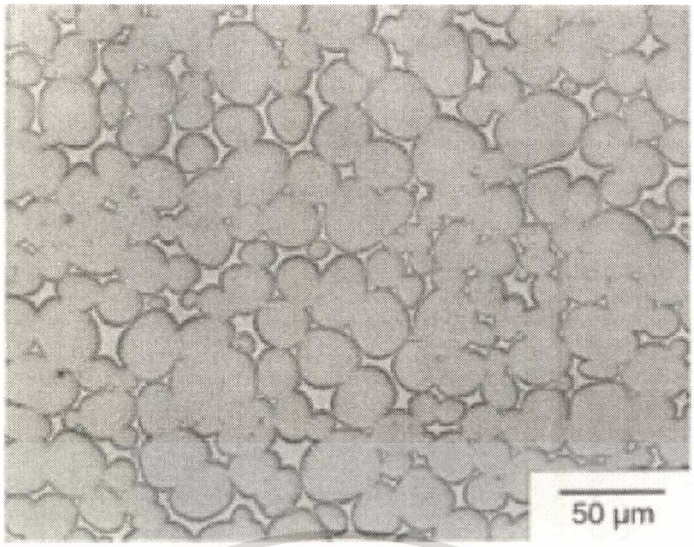

Figure 2.23 Microstructure of a liquid phase sintered 93 wt% tungsten heavy metals (ASM International, 1998).

Table 2.6 Variation of density and Young's modulus with tungsten content (German, 1994).

wt% W	Density, g/cm^3	Young's modulus, Gpa
90	17.2	345
91	17.4	350
93	17.8	360
95	18.2	370
97	18.6	385
98	18.8	390
100	19.3	410

Nowadays tungsten is widely used in various industrial that includes (ASM International, 1998):

- Damping weights for computer disk drive heads.
- Balancing weights for ailerons in commercial aircraft, helicopter rotors, and for guided missiles.
- Kinetic energy penetrators for defeating heavy armor.
- Fragmentation warheads.
- Radiation shielding, radioisotope containers and collimation apertures for cancer therapy devices.

- High performance lead-free shot for waterfowl hunting.
- Gyroscope components.
- Weight distribution adjustment in sailboats and race cars.
- Heavy casings for downbore logging of oil wells.
- Weights in premium golf clubs for improving consistency in response.
- Low chatter, high stiffness boring bars and toolholders for metalworking.
- Electrical contacts.

CHAPTER 3

EXPERIMENTAL PROCEDURES

3.1 Material

3.1.1 Feedstock

A feedstock used in this experiment was supplied by BASF, Aktiengesellschaft, Ludwigshafen, Germany. The tungsten alloy powder is composed of tungsten-nickel-copper-cobalt (W-Ni-Cu-Co) alloy and thermoplastic polymers are used as a binder. The chemical compositions of tungsten alloy powder are shown in **Table 3.1** and the feedstock for the production of tungsten alloy specimens are shown in **Figure 3.1**.

Table 3.1 Chemical compositions of tungsten alloy powder.

Chemical composition		
Element	Tungsten	Nickel + Copper + Cobalt
Weight (%)	≥ 94	Balance

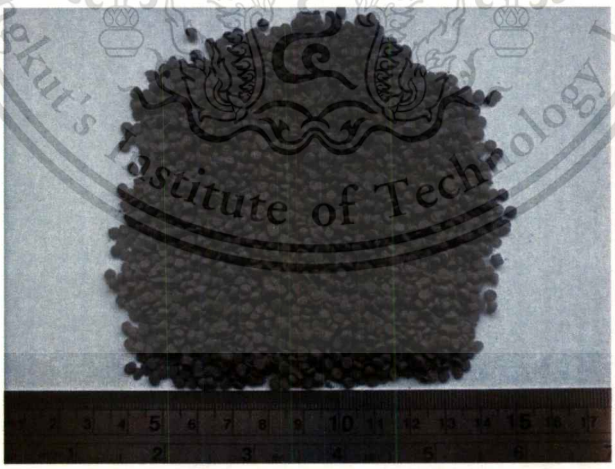

Figure 3.1 Ready-to-mold feedstock of tungsten alloy metal.

3.1.2 Gas

In debinding process, nitric acid was used as a catalyst and a 99.99% purity nitrogen gas was used as a purging gas.

3.2 Equipment

3.2.1 Equipment for Specimens Preparation

1. Injection molding machine produced by Thai Machinery Association model MT50E (**Figure 3.2**) for injection molding of green specimens.

2. Catalytic debinding oven using nitric acid as a catalyst (**Figure 3.3**).

3. Sintering furnace for brown specimens sintering (**Figure 3.4**).

Figure 3.2 Injection molding machine.

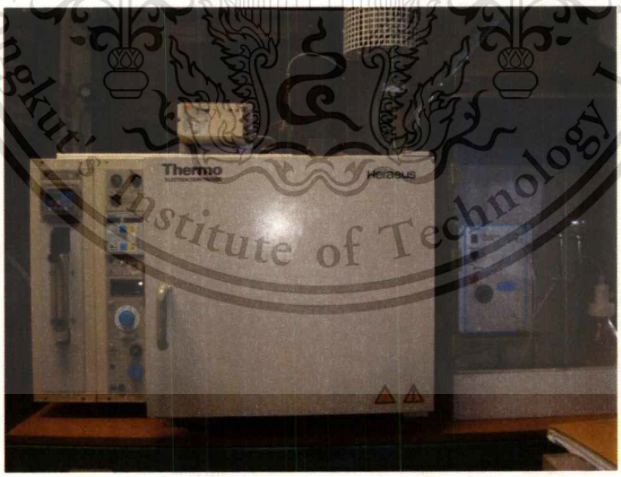

Figure 3.3 Catalytic debinding oven.

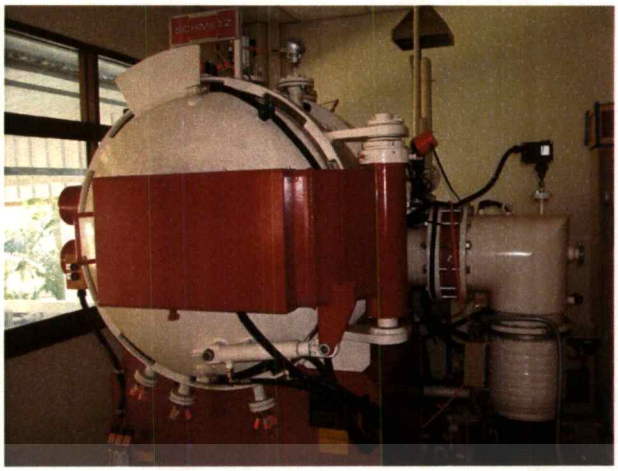

Figure 3.4 Sintering furnace.

3.2.2 Equipment for Properties Testing

1. Digital vernier model Digimatic Caliper produced by Mitutoyo Co., Ltd.
2. Analytical balance produced by Mitutoyo Co., Ltd (**Figure 3.5**).
3. Profile projector model PH-3500 produced by Mitutoyo Co., Ltd (**Figure 3.6**).
4. Tensile testing machine model 8801 produced by Instron Co., Ltd.
5. Hardness testing machine model Wolpert 930/250 produced by Instron Co., Ltd.
6. Cut off machine model Discotom-5 produced by Struers Co., Ltd.
7. Hot Mount machine model LaboPress-3 produced by Struers Co., Ltd.
8. Grinding machine model LaboPol-25 produced by Struers Co., Ltd (**Figure 3.7**).
9. Reflecting microscope model Eclipse produced by Nikon Co., Ltd (**Figure 3.8**).

Figure 3.5 Analytical balance.

Figure 3.6 Profile projector.

Figure 3.7 Grinding machine.

Figure 3.8 Reflecting microscope.

3.3 Process

3.3.1 Injection Molding

The tensile test specimens of 94 wt.% W-balance (Ni-Cu-Co) alloy were prepared by an injection molding machine. The melting point of the feedstock was tested by Differential scanning calorimeter (DSC) analysis for providing injection molding temperatures. The minimum injection temperature should be higher than feedstock melting point but lower than decomposition temperature in order that binder decomposition does not occur. **Figure 3.9** shows the dimension of tensile test specimen. The injection molded specimens are commonly called "green specimens".

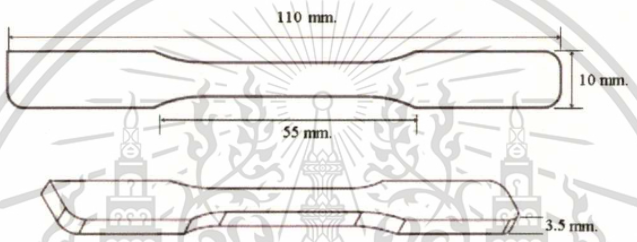

Figure 3.9 Dimension of tensile test specimen.

3.3.2 Debinding

Debinding of the green specimens was performed in two stages: catalytic debinding and thermal debinding. The green specimens were debinded in catalytic debinding process at 145°C by using nitric acid as a catalyst. Nitric acid feeding rate of 15 ml/h and a purging gas (nitrogen) throughput of 500 l/h were adopted in debinding process. The acid catalyzes rapid debinding (depolymerisation of the binder) of the green specimens from outside in. The binder comprises of multi components allow binder removal in stages during the debinding process. As the first binder component depolymerises and vaporizes from within the molded specimens, forming a large amount of open pores. The remaining binder components will serve to retain the shape of the part. During thermal debinding, performed in the initial stage of sintering process, these open pores allow the decomposing of the rest of binder to vaporize to the surface of specimen easily.

3.3.3 Sintering

After debinding, the brown specimens were sintered under vacuum atmosphere with sintering chamber pressure of 10^{-5} bar. A sintering cycle (**Figure 3.10**) started with heating from

room temperature to 600°C at the heating rate of 5°C/min, held at that temperature for 2 hours to remove remaining binders. After the holding time was completed, the temperature further increased to the sintering temperatures at 1350, 1400 and 1450°C with the same heating rate at varied sintering times for 2, 3 and 4 hours, respectively.

The processing steps of the experiment are illustrated in **Figure 3.11**.

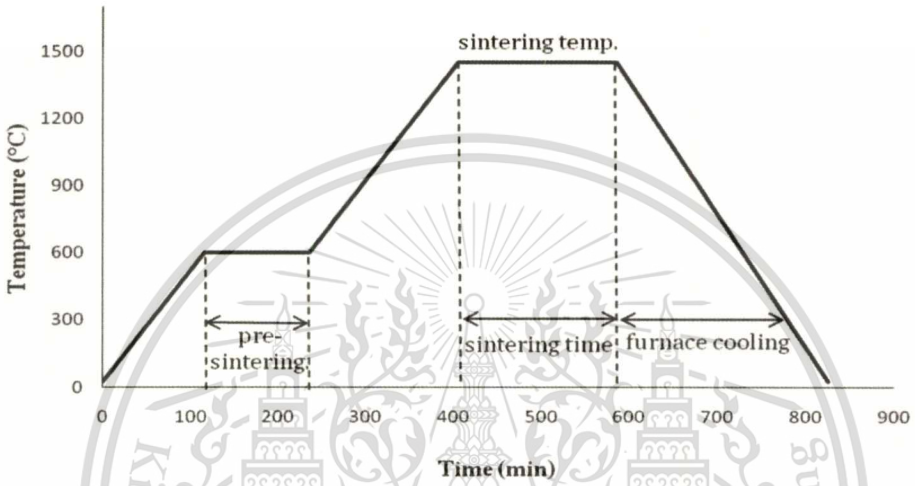

Figure 3.10 Sintering profile.

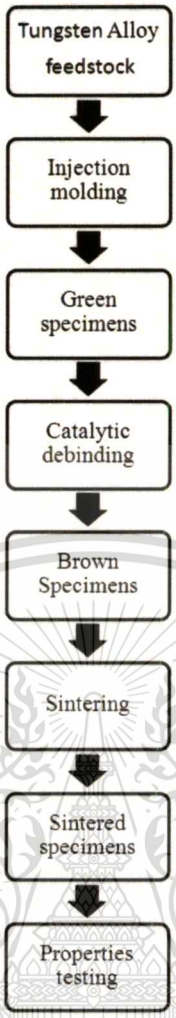

Figure 3.11 Flow chart of steps and experimental procedures.

3.4 Properties Testing

3.4.1 Differential scanning calorimetry (DSC)

The melting point of the feedstock was tested by DSC analysis. The feedstock was tested the thermal properties of the binder components with the heating rate of 20°C/min in N_2 atmosphere with a flow rate of 60 ml/min. The peak melting and recrystallization temperatures foe the feedstock are available from standard compilations. DSC data are valuable for providing injection molding temperatures.

3.4.2 The thermogravimetric analysis (TGA)

The thermogravimetric analysis (TGA) provides information on the degradation temperature range of the feedstock components. TGA plots the percentage change in mass related to a temperature. In this experiment, the thermal degradation properties were determined

in the temperature range of 30-800°C with a heating rate 20°C/min under nitrogen atmosphere with a flow rate of 60 ml/min.

3.4.3 Dimensional Change

Sintering gives strong bonds between particles and removes or reduces the pores by densification. Hence, sintering causes substantial shrinkage in the MIM specimens. Therefore, the dimensional change of the sintered specimens was measured relatively to their green specimens. The measurement was taken at the positions as shown in **Figure 3.12**. Position 1 and 3 are grip's width, position 2 is gauge's width, position 4 is specimen's length and position 5 is specimen's thickness. The dimension change of the sintered specimens from their green stage can be calculated as equation 3.1

Figure 3.12 The specific positions for measuring dimension in the specimen.

$$DC = \frac{(Dg - Ds)}{Dg} \times 100 \tag{3.1}$$

where, DC = the dimension change (%),

D_g = the dimension of the green specimen (mm),

D_s = the dimension of the sintered specimen (mm).

3.4.4 Density

The density of the W-(Ni-Cu-Co) specimens sintered at different sintering conditions was measured by the Archimedes' principle. This corresponded to the standard test method of ASTM B311. The density can be calculated as equation 3.2

$$\rho = \frac{m_a}{m_a - m_w} \times (\rho_0 - d) + d \tag{3.2}$$

where, ρ = the density of test specimen (g/cm^3),

m_a = mass of the specimen in air (g),

m_w = mss of the specimen in water (g),

ρ_0 = the density of water (g/cm^3),

d = the density of air (approx. 0.001 g/cm^3).

3.4.5 Tensile Properties

The specimens were tested for their tensile properties according to the ASTM E8 standard by using Universal Testing Machine model 8801 which produced by Instron Co., Ltd. Crosshead speeds of 2 mm/min were used for the measurement of the tensile strength. All measurements were performed for five sintered specimens and averaged to obtain the results.

3.4.6 Hardness

The Rockwell scale B (HRB) hardness test was selected to measure the apparent macroscopic hardness of the specimen according to ASTM E18 standard by using Universal Testing Machine produced by Instron Co., Ltd.

3.4.7 Microstructure Preparation

The sintered specimen was cut into small pieces to reveal cross section and was then hot mounted in the resin. The specimen was firstly ground with silica papers grade 240, 400, 600, 800, 1000, 1200 and 2400, consecutively and subsequently fine polished with the diamond suspension size 6, 3 and 1 micrometer, respectively. The optical microscope was used to observe the microstructures of the specimen.

3.4.8 Scanning electron microscope (SEM)

The microstructure and the fracture surface of the tensile test specimens were observed by using Scanning electron microscope. The SEM micrograph was observed by scanning with a beam of electrons in a raster scan pattern, which is held within a vacuum atmosphere. Once the beam hits the specimens, electrons and X-rays are ejected from the specimens. Detectors collect these X-rays, backscattered electrons, and secondary electrons and convert them into images.

3.4.9 Energy dispersive spectroscopy (EDS)

In order to study the elemental distribution and composition in the microstructure of sintered W-(Ni-Cu-Co) specimen, the energy dispersive spectroscopy (EDS) with mode of quantitative analysis, elemental mapping and line profile analysis were performed with the sintered W-(Ni-Cu-Co) specimens.

CHAPTER 4

RESULTS AND DISCUSSION

4.1 Injection Molding

Differential scanning calorimetry (DSC) data are valuable for providing injection molding temperatures (Loh *et al.*, 2001). The melting point of the feedstock was tested by DSC analysis. The feedstock was tested the thermal properties of the binder components with the heating rate of 20°C/min in N_2 atmosphere with a flow rate of 60 ml/min. The DSC result of W-(Ni-Cu-Co) feedstock is illustrated in **Figure 4.1**. As shown, the melting peak temperature of W-(Ni-Cu-Co) feedstock is 168.5°C. This temperature can be selected to establish the injection molding temperature range. Thus, the minimum injection temperature should be higher than 168.5°C but lower than binder decomposition temperature in order that binder decomposition does not occur (Jigui *et al.*, 2010).

The thermogravimetric analysis (TGA) provides information on the degradation temperature range of the feedstock components. **Figure 4.2** shows the plotted of the percentage change in mass of W-(Ni-Cu-Co) feedstock and temperature. The thermogravimetric analysis shows that the binder comprises of multi components. The binder starts to degrade at about 200°C and complete the degradation at about 530°C. It can be observed from **Figure 4.2** that the loss weight from 200 to 325°C is about 5.86%. From 325 to 420°C is about 0.23%. The weight loss of the binder almost unchanged from 420 to 530°C (about 0.086%). All of the binder is removed at about 530°C

Defect-free green specimens with the tensile test bar shape were obtained at the injection molding temperature of 175°C with the mold temperature of 100°C. Averaged weight and density of tensile test bars were 29.46 g and 10.09 g/cm^3, respectively. The average weight, density and dimension of green specimens are shown in **Table 4.1**. **Figure 4.3** shows the figure of tensile test bar specimens molded.

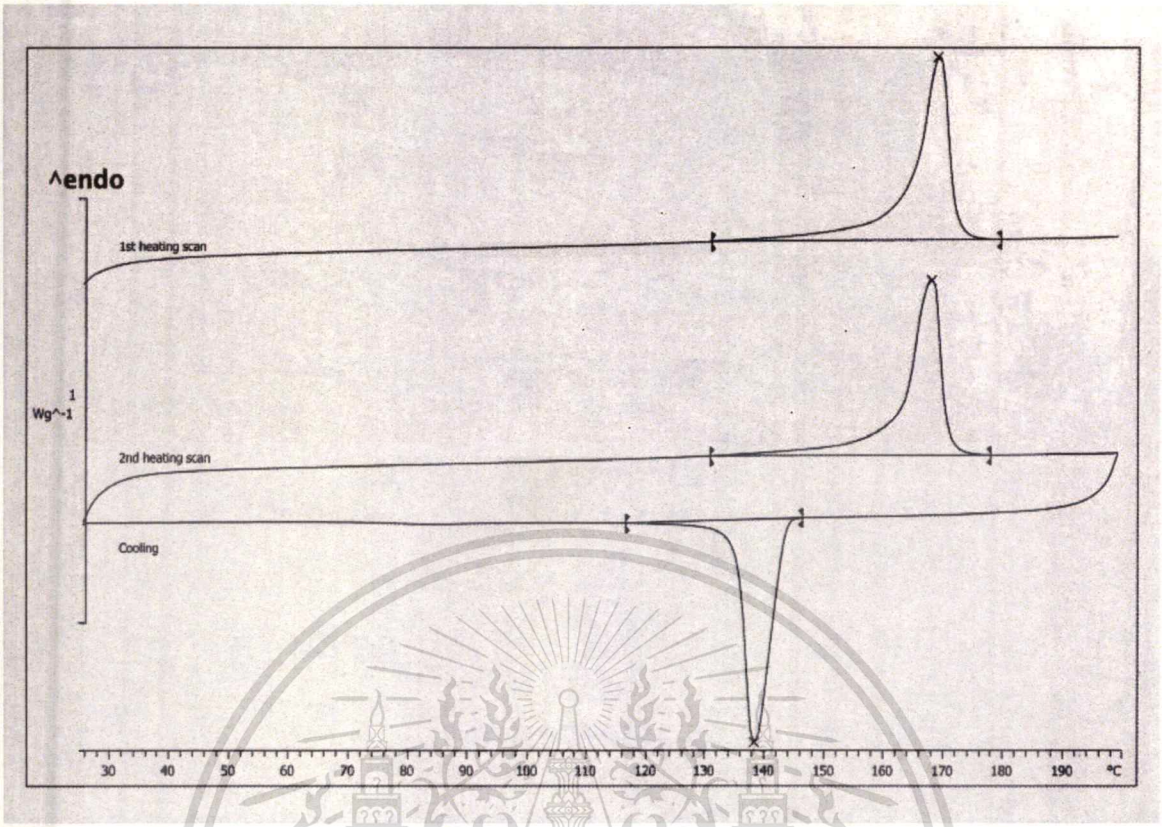

Figure 4.1 Differential scanning calorimetry curve of the W-(Ni-Cu-Co) feedstock.

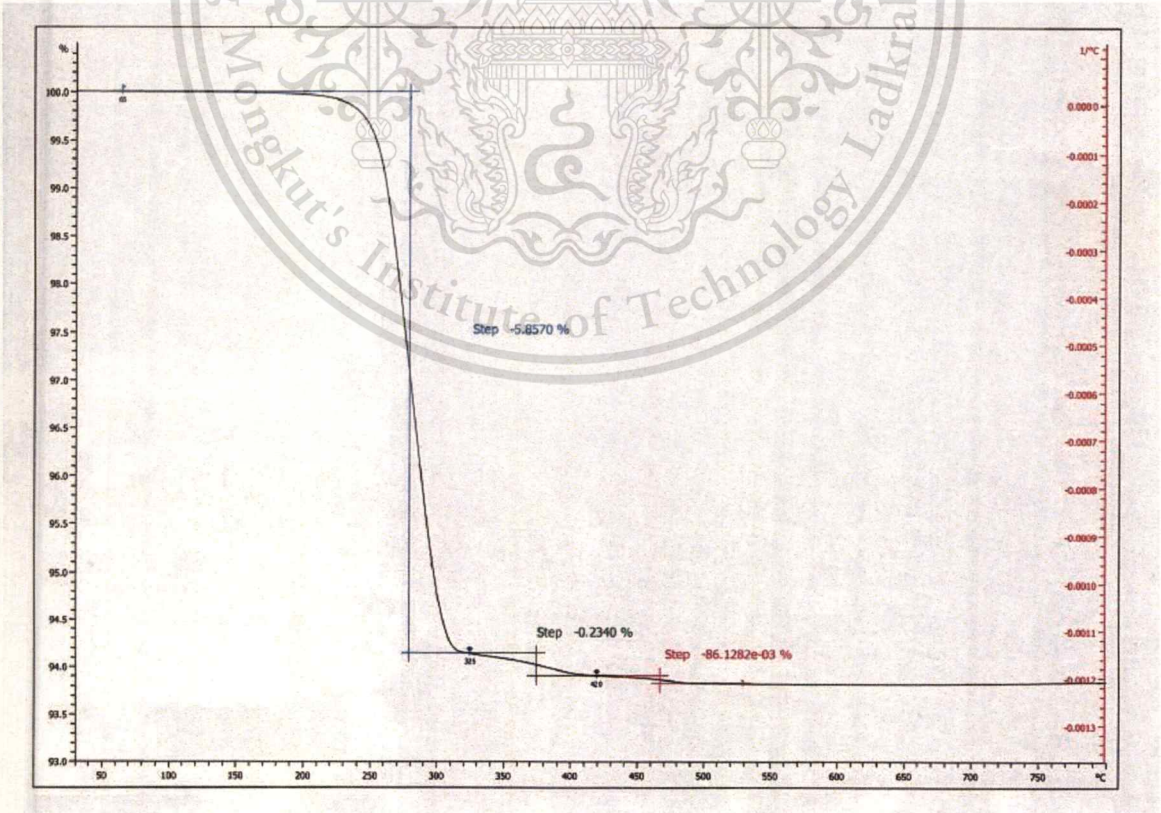

Figure 4.2 Thermogravimetric analysis of the W-(Ni-Cu-Co) feedstock.

Table 4.1 Green specimens' physical properties

Weight (g)	Density (g/cm^3)	Dimension (mm)				
		Grip	Gauge	Grip	Length	Thickness
29.46	10.01	10.28	6.24	10.27	100.07	3.59

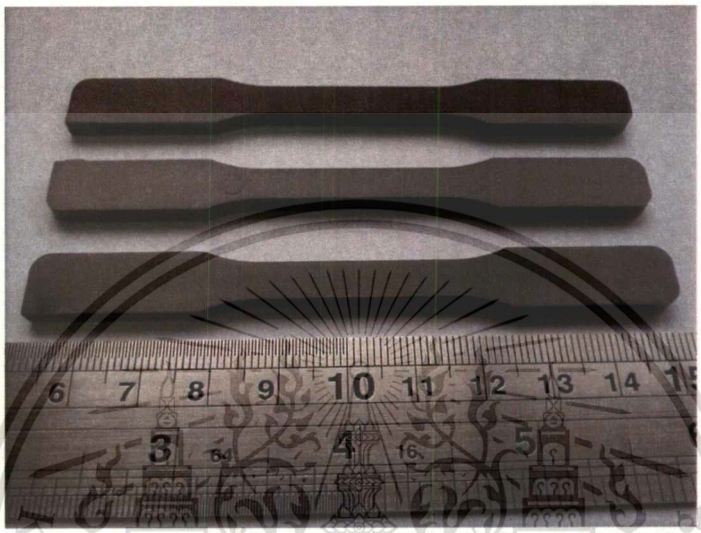

Figure 4.3 The figure of tensile test bar specimens.

4.2 Debinding Process

The debinding process used catalytic amounts of nitric acid. The acid catalyzes rapid debinding (depolymerisation of the binder) of the green specimens from outside in (Krueger *et al.*, 1993). The TGA curve shows that the binder comprises of multi components, which allow binder removal in stages during the debinding process. As the first binder component depolymerises and vaporizes from within the molded specimens, the remaining binder components will serve to retain the shape of the part (Li *et al.*, 2009).

In this work, the green specimens were debinded in catalytic debinding process at 145°C under nitric acid vapour atmosphere with the feeding rate of 15 ml/h for various times. The effect of debinding time on binder weight loss of molded specimens is shown in **Figure 4.4**. It can be seen from **Figure 4.4** that the debinding rate is fast at the debinding time increases from 1 to 2 hours, the amount of binder extracted increases approximately from 61 to 71%. However, the debinding rate reduces when the debinding time increases. At the debinding time ranging from 4 to 6 hours, the binder weight loss of molded specimens almost unchanged (from 74.9 to 75.3%). This suggests that the binder extraction nearly reaches saturation (Zaky, 2004), which means that

the binder weight loss would be constant even the debinding time is increased further. Therefore, it can be noticed that the debinding time of 4 hours is selected as the enough time for removing the major binder (74.9wt%). After debinding, the debinded specimens had good surface appearance with dark gray colour. The visual inspection (shown in **Figure 4.5**) was also observed by breaking some parts and then scratching the cross section area on the paper. **Figure 4.6** exhibits the Scanning electron micrograph of a specimen after catalytic debinding. It was observed that the debinded specimens have a large amount of open pores. This affirms that most of the binders were debinded, forming porous structure of metal powders held by residual binder. These pores allow the decomposing of the rest of binder after thermal debinding, performed in the initial of sintering, to vaporize to the surface of specimen easily. **Figure 4.7** presents the XRD patterns of debinded W-(Ni-Cu-Co) specimen. The XRD result shows the strongest diffraction peak of tungsten peak at a 2θ angle of ~40.4, 58, 73 and 87°. Weak peaks of $Cu_{0.4}W_{0.6}$ are observed at 2θ angle of ~58.5, 73.5 and 87.3°. Small peaks of Co_7W_6 and Ni are also detected.

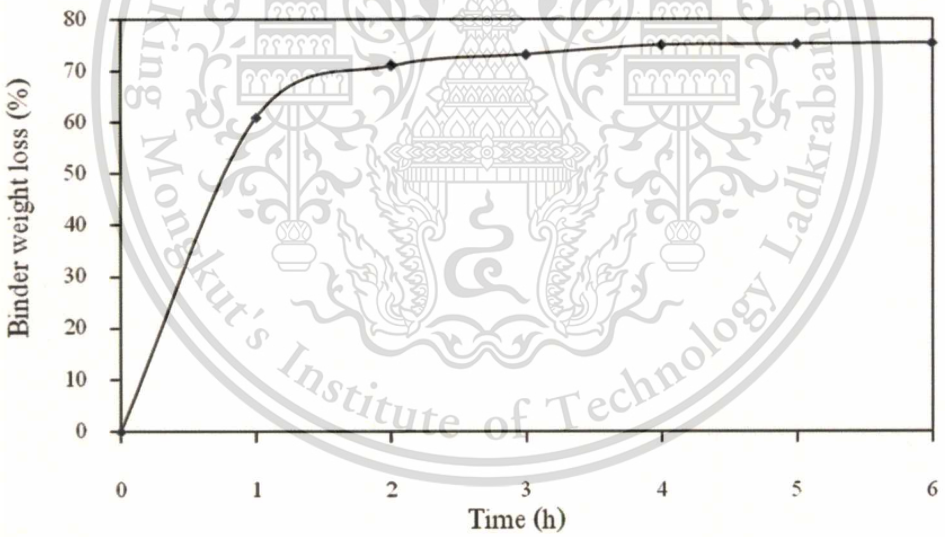

Figure 4.4 The effect of debinding time on binder weight loss of molded specimens.

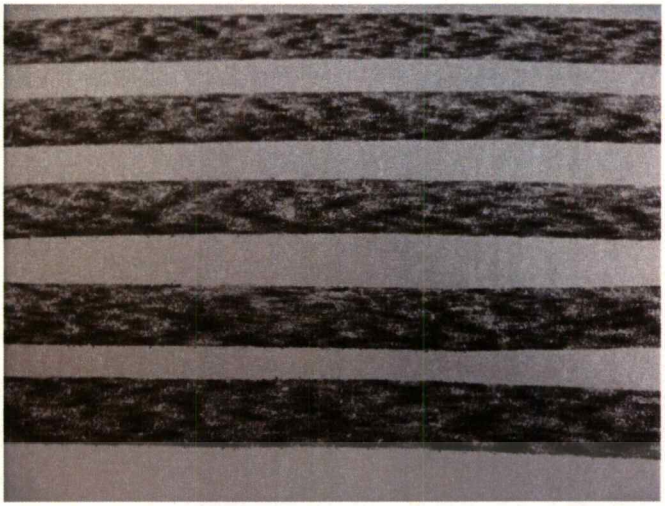

Figure 4.5 The visual inspection of debinded specimens.

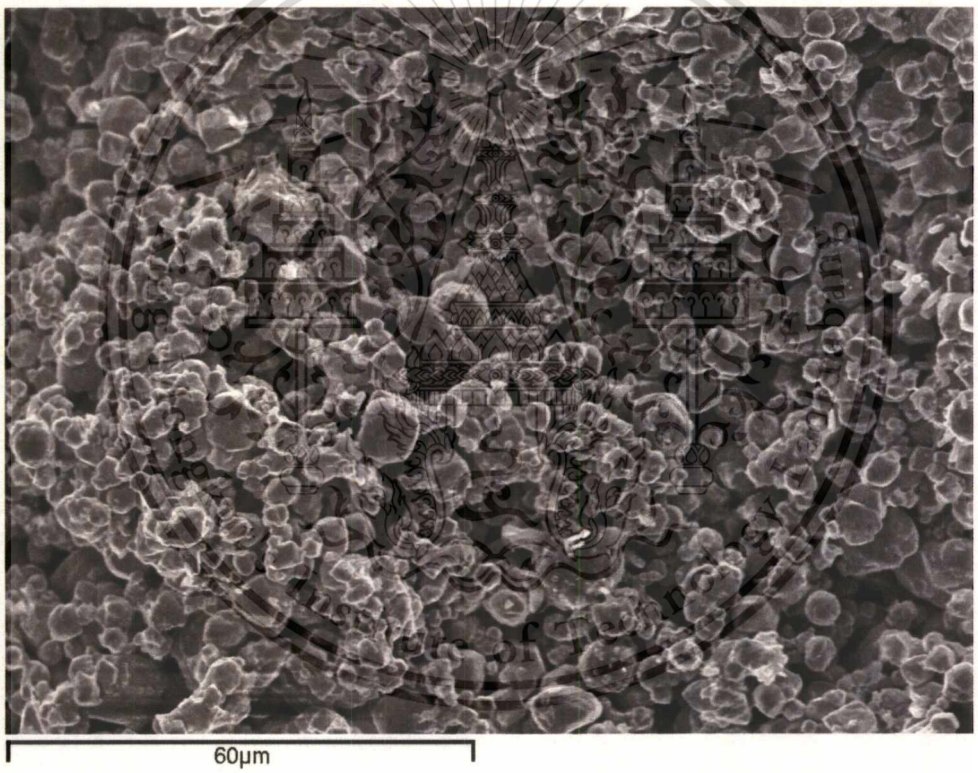

Figure 4.6 SEM micrograph of a debinded W-(Ni-Cu-Co) specimen.

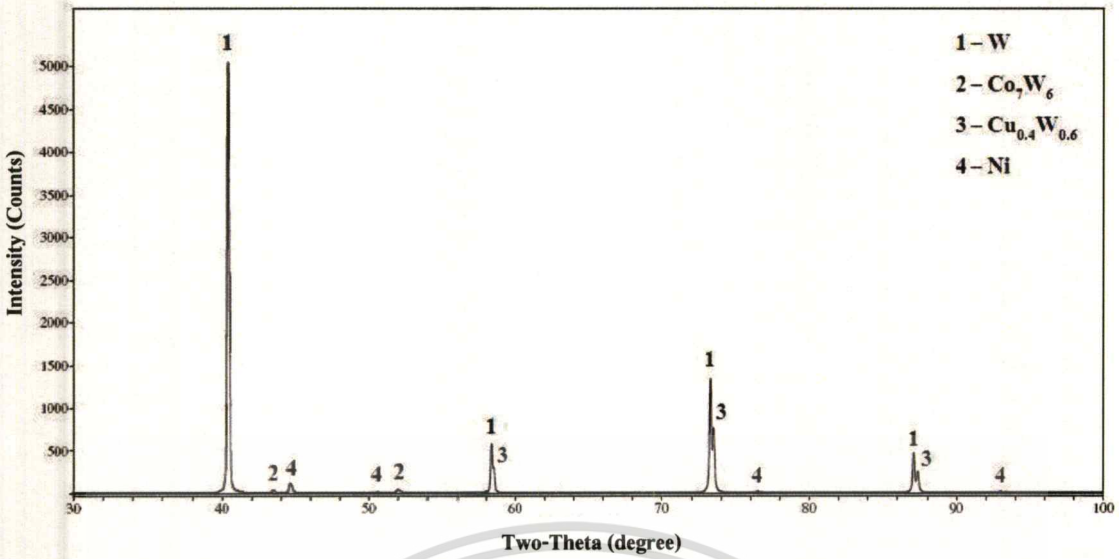

Figure 4.7 XRD pattern of debinded specimen.

In this experiment, after debinding process, the brown specimens were carried out into the sintering process at various sintering temperatures and sintering times under vacuum atmosphere (with sintering chamber pressure of 10^{-5} bar). Sintered W-(Ni-Cu-Co) specimens were then tested the properties. The results were examined to find out the optimal sintering condition.

4.3 Effects of Sintering Temperatures and Sintering Times on Physical Properties

4.3.1 Sintered Density

Sintering densification depends greatly on sintering temperature (Jigui *et al.*, 2010). As the sintering temperature increases, the density increases also. Initially, the average green density was 10.09 g/cm^3. Densities of the W-(Ni-Cu-Co) specimens sintered at different sintering temperatures and sintering times are shown in **Figure 4.8**. The results show that the sintered densities of specimens sintered at 1450°C were higher than the others. The density slightly increases from sintering temperature of 1350 to 1400°C but dramatically increases from 1400 to 1450°C. At sintering temperature of 1450°C with increasing of sintering time from 2 to 3 hours, density increases from 17.68 to 18.02 g/cm^3. A decrease in density is observed when the sintering time is increased to 4 hours. For sintering times in the range of 2-4 hours, the sintering for 3 hours yielded highest sintered density. However, the sintering for longer than 3 hours yielded lower sintered density.

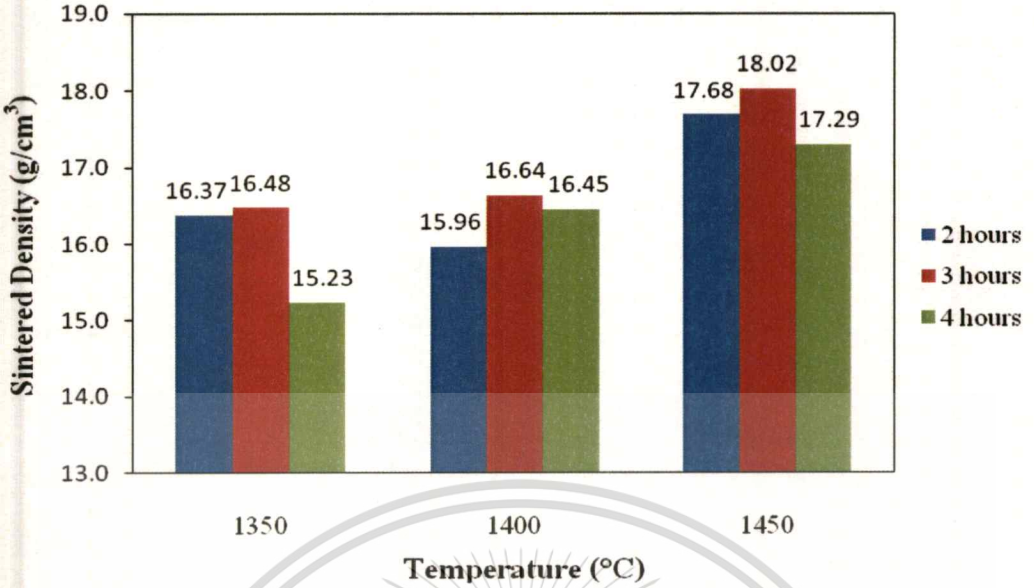

Figure 4.8 Densities of the W-(Ni-Cu-Co) specimens sintered under different sintering conditions.

4.3.2 Dimensional Change

The dimensions of W-(Ni-Cu-Co) specimens before and after sintering were measured and examined. **Figure 4.9** shows a comparison between a sintered specimen (a) and a green one (b). From the previous result, there was the increase in sintered density relative to green density. This had to be accompanied by the shrinkage of the specimens. The shrinkage along grip width, gauge width, length and thickness at various sintering temperatures and sintering times are shown in **Figure 4.10**, **4.11**, **4.12** and **4.13** respectively. The results show that the sintered W-(Ni-Cu-Co) specimens showed shrinkage along all dimensions and showed a similar trend at all directions. At constant sintering temperature with varied sintering times, the shrinkage slightly increases with increasing sintering time. With varied sintering temperatures, the shrinkage significantly increases with increasing sintering temperature. The shrinkage at all positions was highest at sintering temperature of 1450°C for 3 hours. The maximum shrinkage along grip width, gauge width, length and thickness were about 17.47, 16.21, 19.09 and 17.61%, respectively. It was observed that the shrinkage of the sintered specimens shows the result corresponding to the density. As the sintering temperature and sintering time increase, the increasing of shrinkage rate because during sintering, pores and void spaces were reduced as result of densification (Moballegh *et al.*, 2005). This was the main cause of shrinkage. Therefore, sintering temperature and sintering time significantly influenced on density, shrinkage and mechanical properties.

Figure 4.9 The figure of sintered (a) and green W-(Ni-Cu-Co) specimen (b).

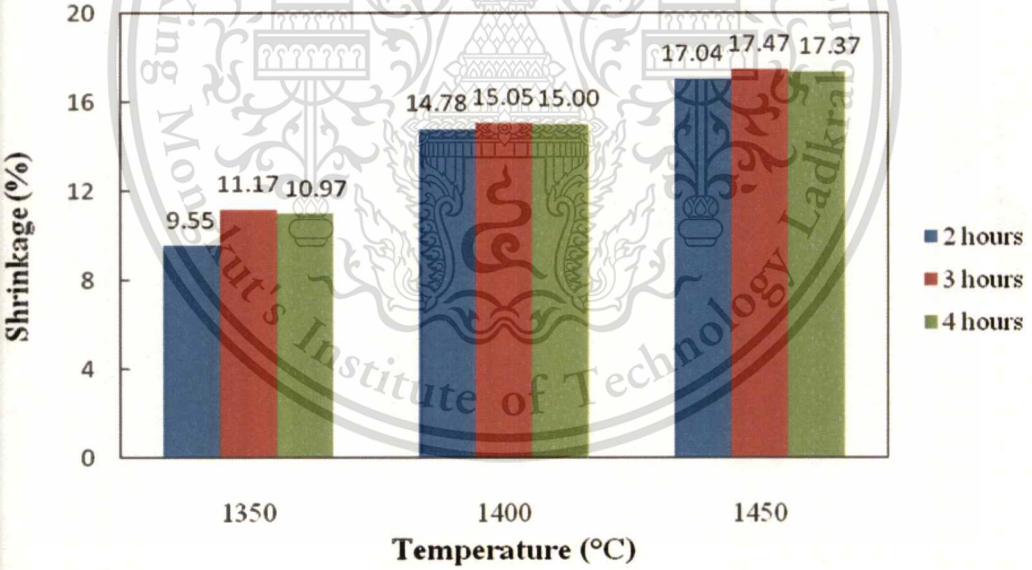

Figure 4.10 The shrinkage along grip width of sintered W-(Ni-Cu-Co) specimens at various sintering conditions.

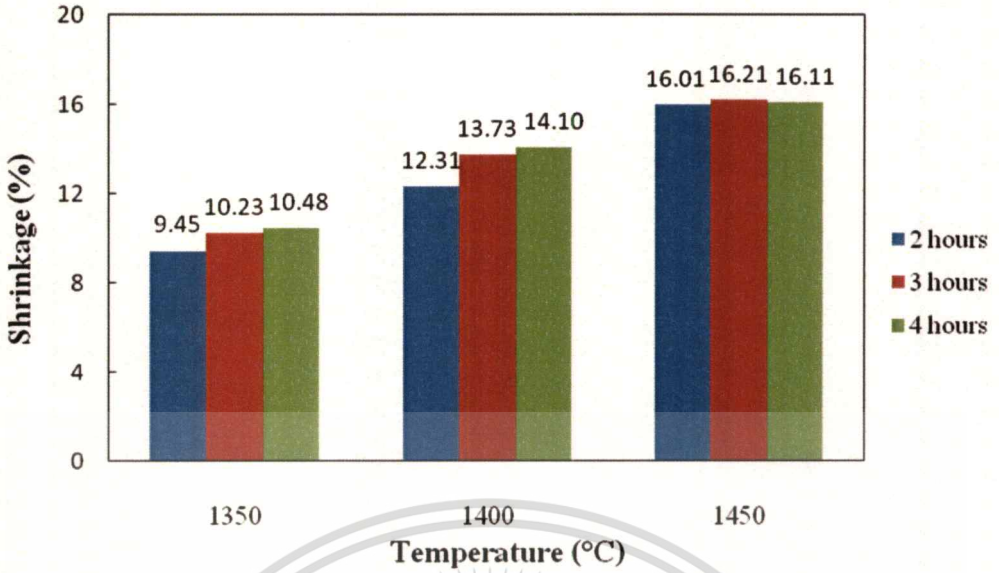

Figure 4.11 The shrinkage along gauge width of sintered W-(Ni-Cu-Co) specimens at various sintering conditions.

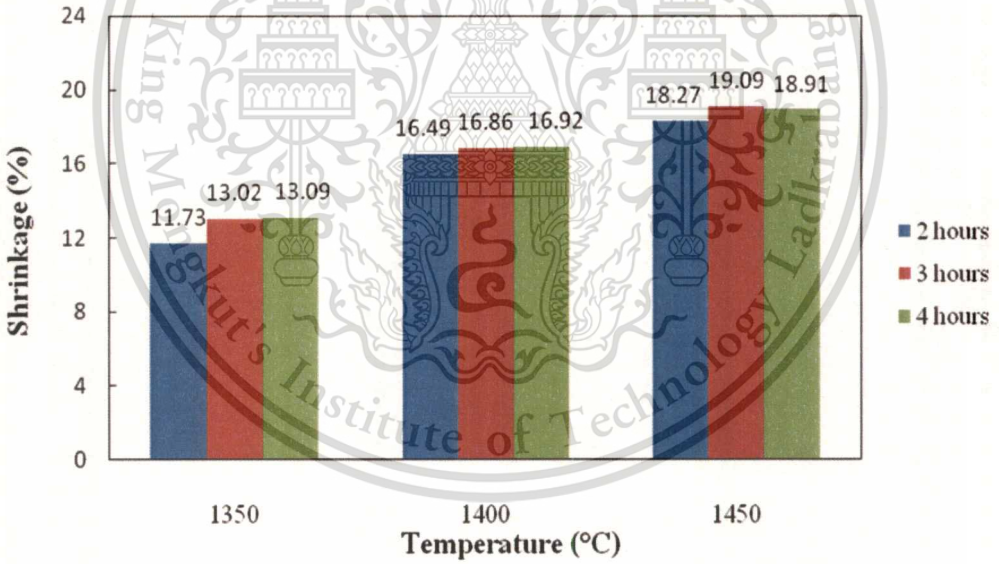

Figure 4.12 The shrinkage along length of sintered W-(Ni-Cu-Co) specimens at various sintering conditions.

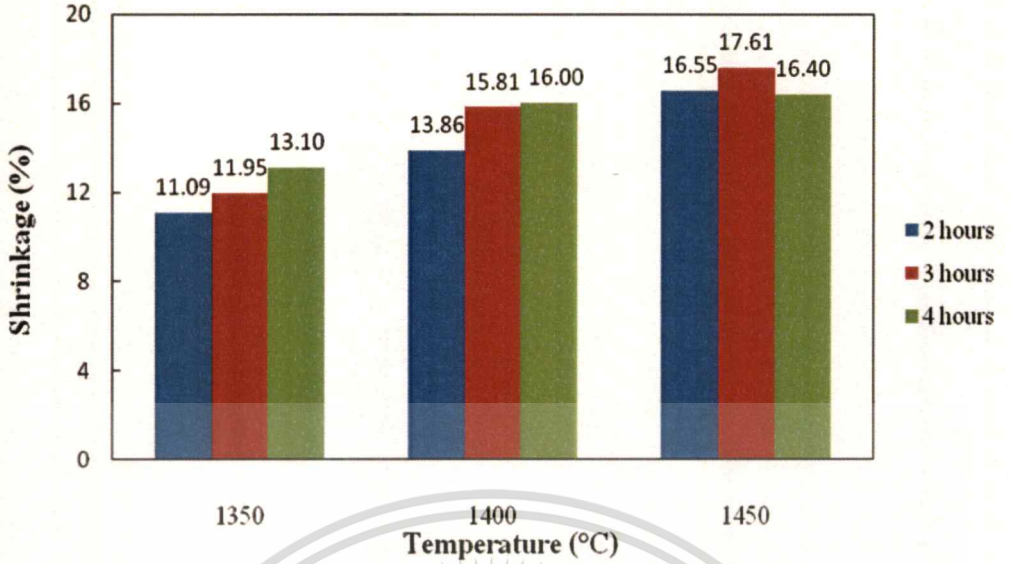

Figure 4.13 The shrinkage along thickness of sintered W-(Ni-Cu-Co) specimens at various sintering conditions.

4.3.3 Microstructures

Microstructures of the specimens sintered at 1350, 1400 and 1450°C are shown in **Figure 4.14, 4.15 and 4.16** respectively. It was observed that the microstructures of sintered W-(Ni-Cu-Co) specimens at sintering temperatures of 1350 and 1400°C were similar. For sintering temperature in the range of 1350 to 1400°C, the microstructures of sintered W-(Ni-Cu-Co) specimens showed that the tungsten and Ni-Cu-Co particles were interconnected to each other, shown in **Figure 4.14** and **4.15**, similar microstructure to solid-state sintering (Hong *et al.*, 2003). Das *et al.* (2009) pointed out that during liquid phase sintering the other elements would be completely melted and form the matrix, which binds the tungsten particles together. Liquid phase sintering system can consist of a combination of boned and non-bonded grain. For the W-(Ni-Cu-Co) system in which the solid is soluble in the liquid, liquid penetration of grain boundaries occurs after melt formation (Xu *et al.*, 1999). In this experiment, at the sintering temperature of 1450°C, microstructures of the sintered W-(Ni-Cu-Co) specimens showed dense pack of spherical tungsten particles uniformly distributed in a sound metal binder matrix (**Figure 4.16**). **Figure 4.17** presents the similar microstructure, prepared by liquid phase sintering at 1500°C for 1.5 hours under H_2 atmosphere, which observed by Das *et al.* (2009). It was found that porosity in metal binder was changed with sintering temperatures and sintering times. Porosity was reduced when the sintering temperature increased, at the same time the grain size increased (Setasuwon *et*

al., 2008). Sintering with too short times resulted in incomplete penetration of the metal binder matrix so pores could not be removed. This indicates that three phenomena are important for densification of the W-(Ni-Cu-Co) brown parts. One is a transition from solid to liquid (Ni-Cu-Co) metal binder. This phenomenon was similar to that reported by Hong *et al.* (2003) (**Figure 4.18**). Second is penetration and occupation of the liquid phase to the pores between tungsten particles. The third involves with rearrangement of tungsten particles. From experimental results, a complete penetration was found in the case of 1450°C sintering for 3 hours. It indicates that a transition temperature from solid to liquid (Ni-Cu-Co) metal binder matrix may be at somewhere between 1400 to 1450 °C. These changes in the microstructure improve the density and mechanical properties of sintered W-(Ni-Cu-Co) specimens (Ding *et al.*, 2012). For too long sintering, however, it was found that porosity growth was observed. It may be attributed to migration of very fine porosity to accumulate somewhere in microstructures. **Figure 4.19** shows the optical microstructure of W-(Ni-Cu-Co) specimen sintered at different conditions.

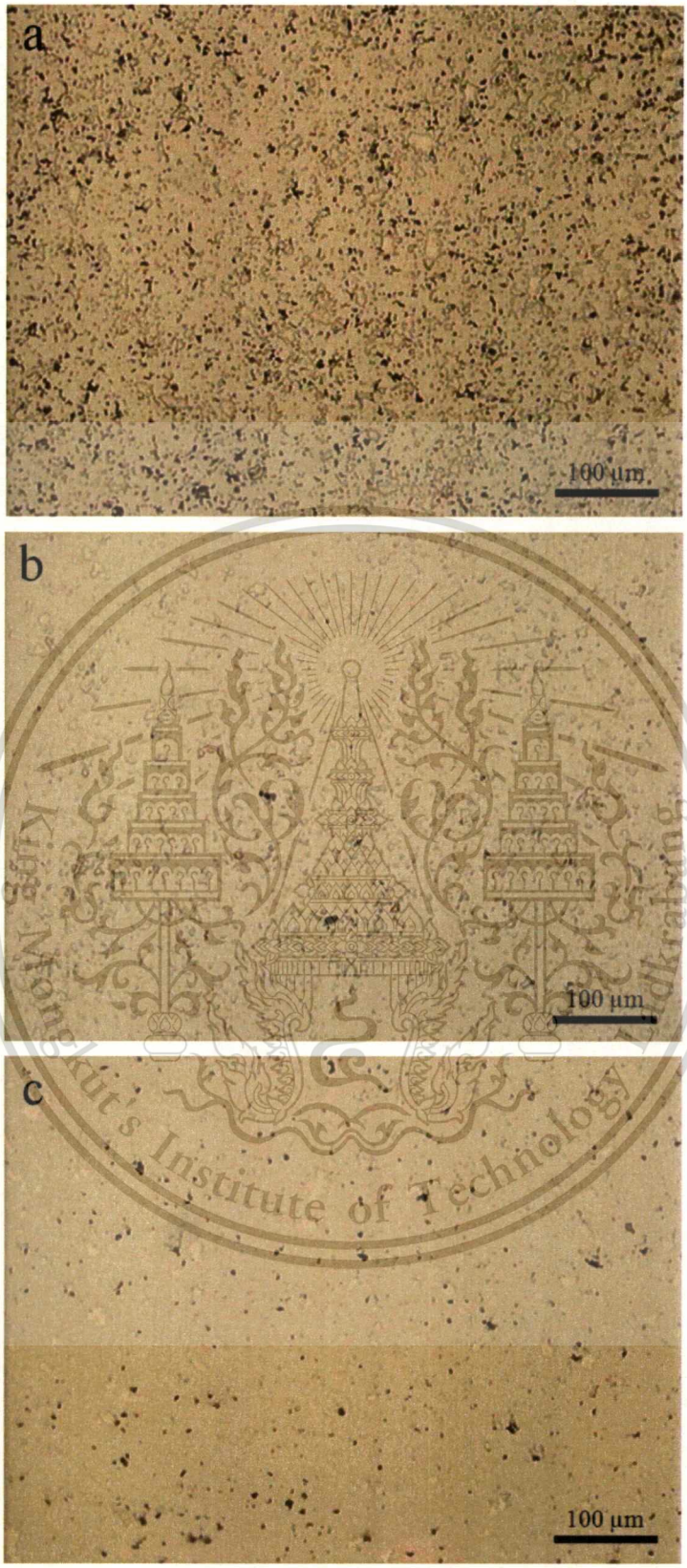

Figure 4.14 Microstructures of W-(Ni-Cu-Co) specimen sintered at 1350°C for (a) 2 hours, (b) 3 hours and (c) 4 hours.

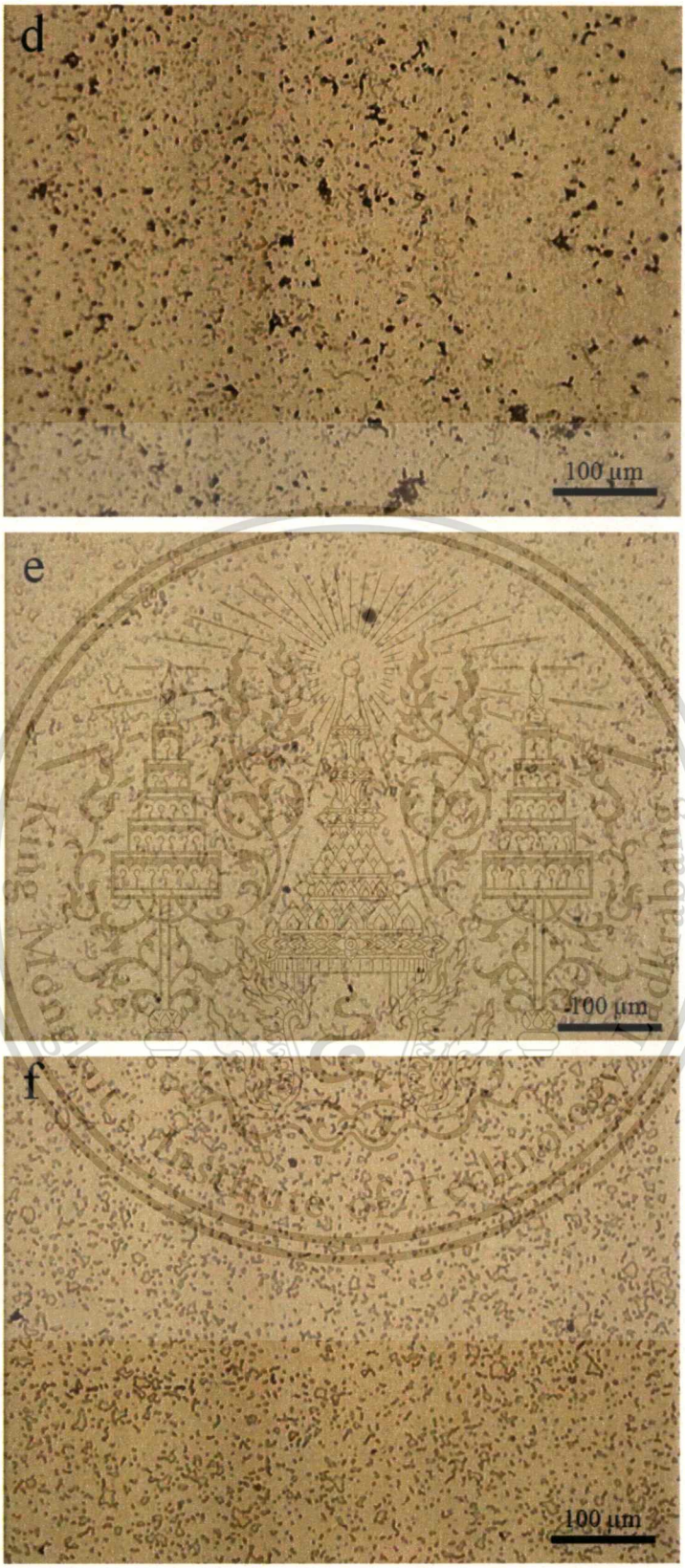

Figure 4.15 Microstructures of W-(Ni-Cu-Co) specimen sintered at 1400°C for (d) 2 hours, (e) 3 hours and (f) 4 hours.

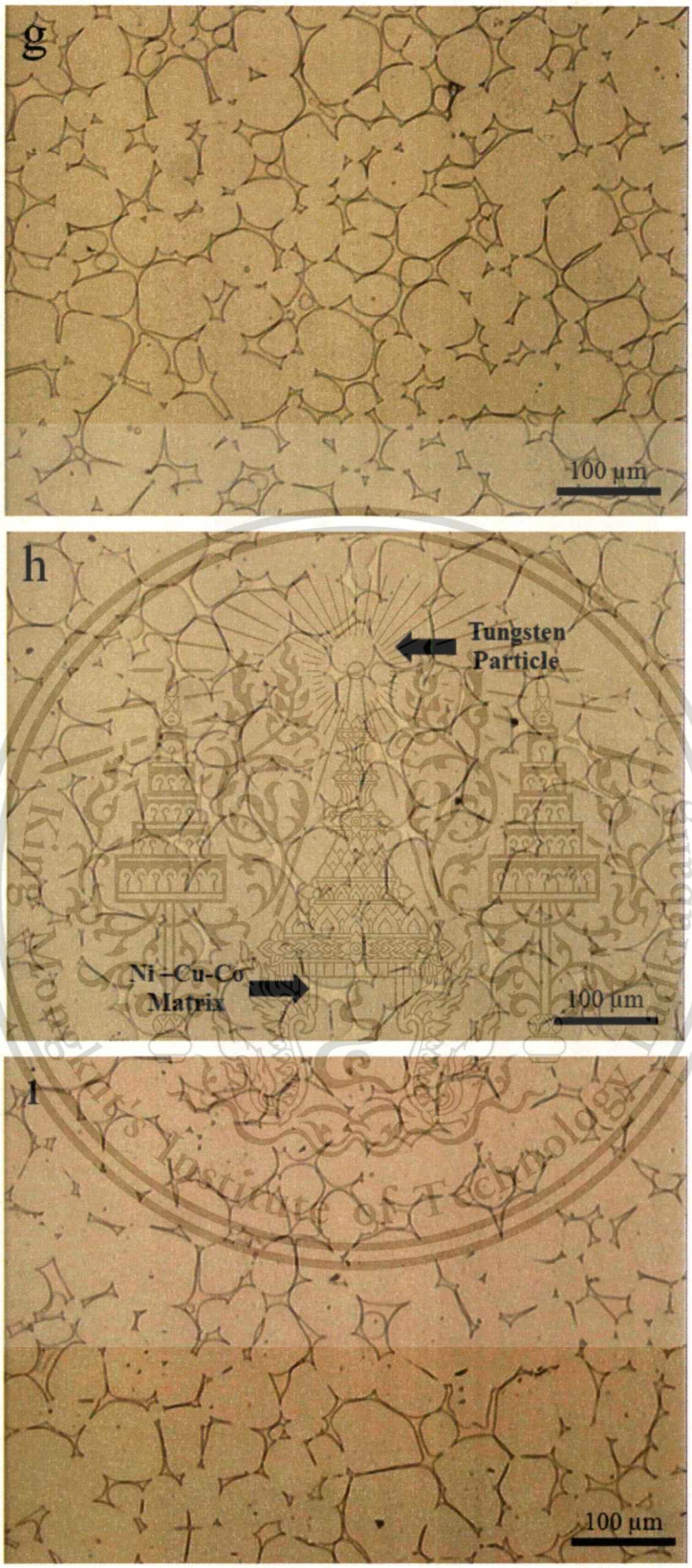

Figure 4.16 Microstructures of W-(Ni-Cu-Co) specimen sintered at 1450°C for (g) 2 hours, (h) 3 hours and (i) 4 hours.

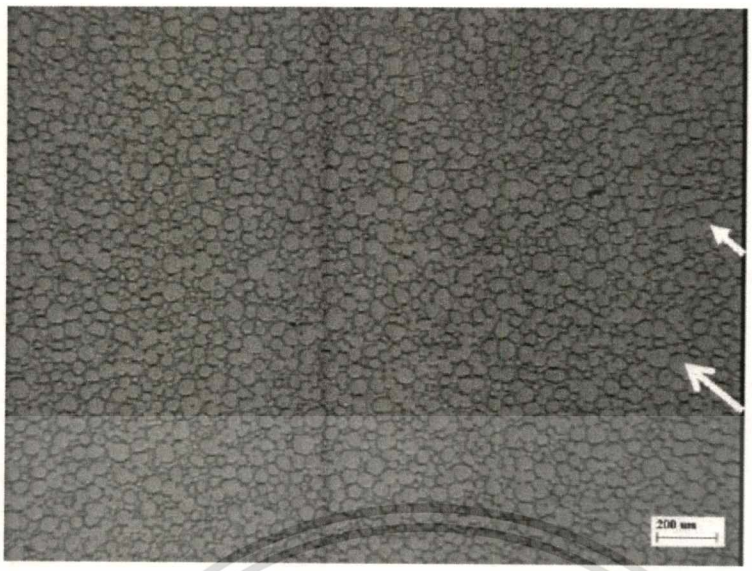

Figure 4.17 Optical microstructure of W-90.5, Ni-7.2, Fe-1.8, Co-0.45, Mo-0.05 alloys sintered at 1500°C for 1.5 hours (Das *et al.*, 2009).

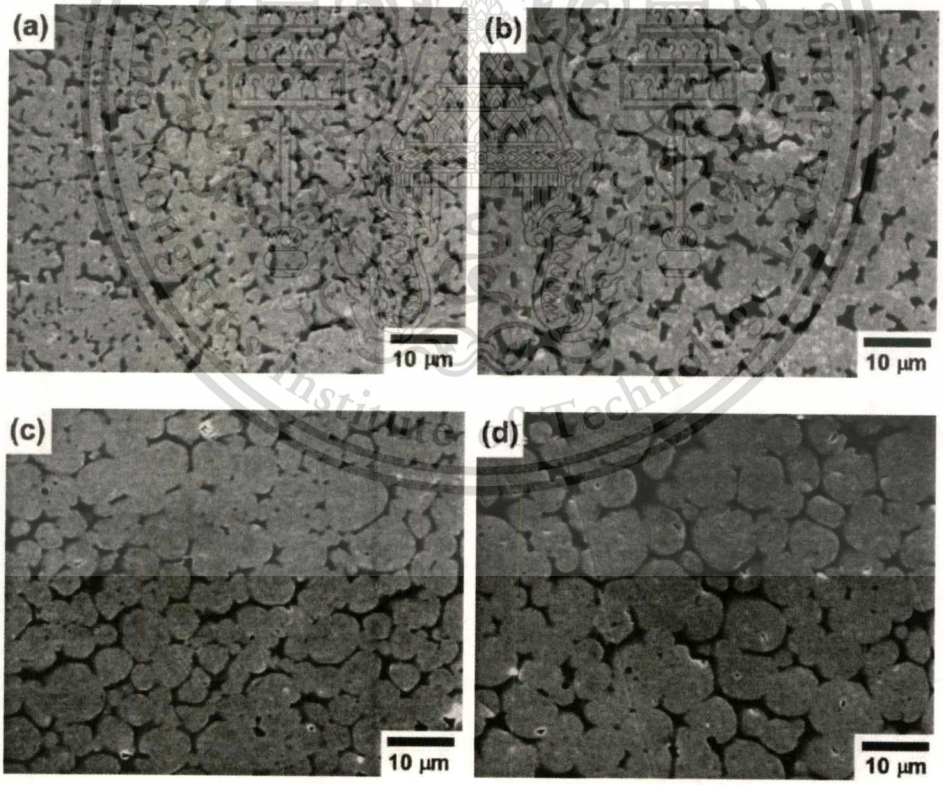

Figure 4.18 SEM of 93W-5.6Ni-1.4Fe tungsten heavy alloys liquid-phase sintered (a) 1445°C, (b) 1460°C, (c) 1470°C and (d) 1485°C for 4 minutes after solid-state sintering at 1300°C for 1 hour (Hong *et al.*, 2003).

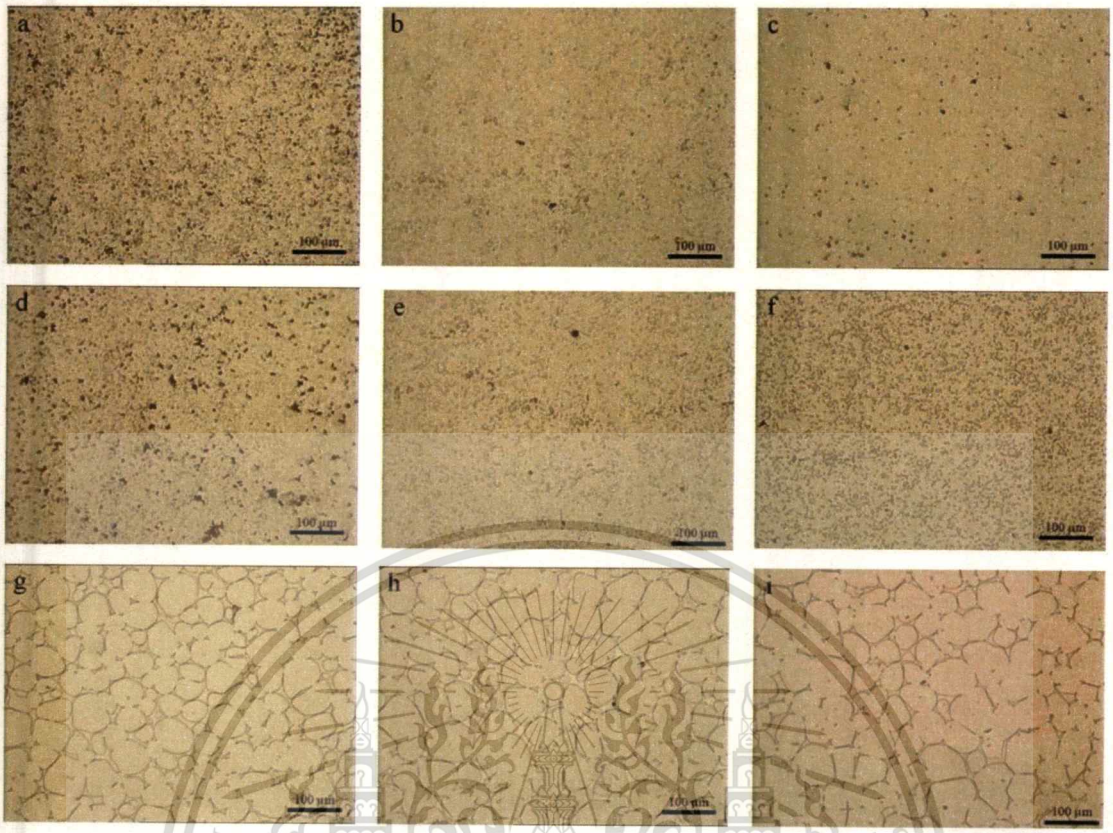

Figure 4.19 Microstructures of W-(Ni-Cu-Co) specimen sintered at different sintering temperatures and sintering times.

Zhu *et al.* (2007) suggested that the composition homogeneity within each phase is necessary for high strength and ductility. Thus, in order to study the elemental distribution and composition in the microstructure of sintered W-(Ni-Cu-Co) specimen, the energy dispersive spectroscopy (EDS) with mode of quantitative analysis, elemental mapping and line profile analysis were performed with the sintered W-(Ni-Cu-Co) specimens sintered at 1400 and 1450°C for 3 hours. **Figure 4.20**, **4.21** and **4.22** show the EDS patterns, elemental mapping and line profile analysis of the W-(Ni-Cu-Co) specimens sintered at 1400°C for 3 hours respectively. **Table 4.2** shows structure elements of EDS patterns in **Figure 4.20**. **Figure 4.23**, **4.24** and **4.25** show the EDS patterns, elemental mapping and line profile analysis of the W-(Ni-Cu-Co) specimens sintered at 1450°C for 3 hours respectively. **Table 4.3** shows structure elements of EDS patterns in **Figure 4.23**. For the EDS results of sintered specimens from both sintering conditions, the color in microstructure can be classified into black and grey. The dark area in the **Figure 4.20** and **4.23** (area number 1) represent the metal binder phase, whereas the grey (area

number 2) area is tungsten phase. The EDS patterns show the tungsten peaks along with Ni, Cu and Co in the matrix binder phase in both microstructures of specimens sintered at 1400 and 1450°C for 3 hours. The results suggested that Ni, Cu and Co have minor solubility in tungsten particles, while tungsten has some solubility in Ni-Cu-Co liquid phase. At sintering temperature of 1400°C for 3 hours, the microstructure shows high tungsten content (28.95wt.%) dissolved in the Ni-Cu-Co binder. For the grey area, the tungsten content is very high and some content of Ni dissolved in tungsten phase was detected but less than 1wt.%. Corresponding to the elemental mapping analysis results that show the solubility of Ni, Cu and Co in tungsten phase has a little solubility, but the tungsten solubility in Ni-Cu-Co phase is higher. However, penetration of the metal binder was incomplete, pores and defects still existed. With increasing temperature, from 1400 to 1450°C, liquid phase sintering occurred. The metal binder phase increases and the tungsten particles distribution become more uniform. The specimens sintered at 1450°C for 3 hours also showed higher tungsten content (34.28wt.%) dissolved in the Ni-Cu-Co binder (with lower Cu content). Neither Ni, Cu nor Co was detected in tungsten phase. This is also in agreement with the elemental mapping analysis results of specimens sintered at 1450°C for 3 hours that show tungsten homogenously dissolved into Ni-Cu-Co phase in a large quantity (**Figure 4.24 (b)**). Distribution of copper was uniformly across the whole specimens. Wetting of the liquid binder on tungsten grains was perfect without porosity.

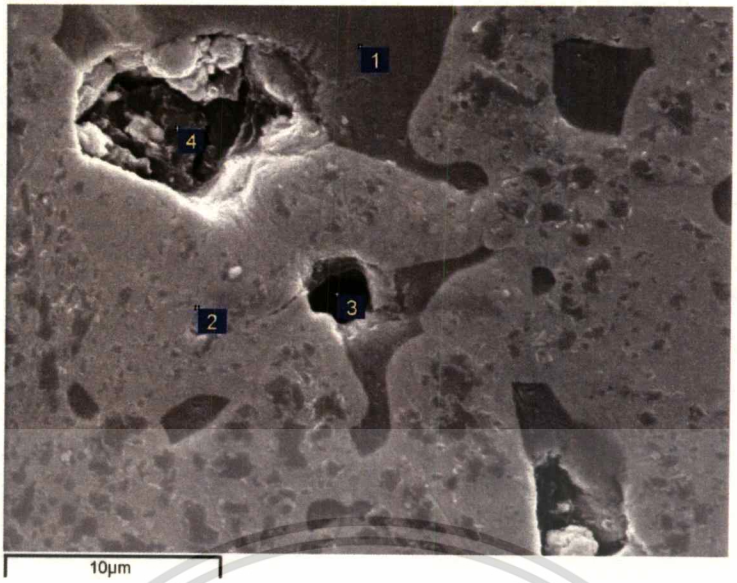

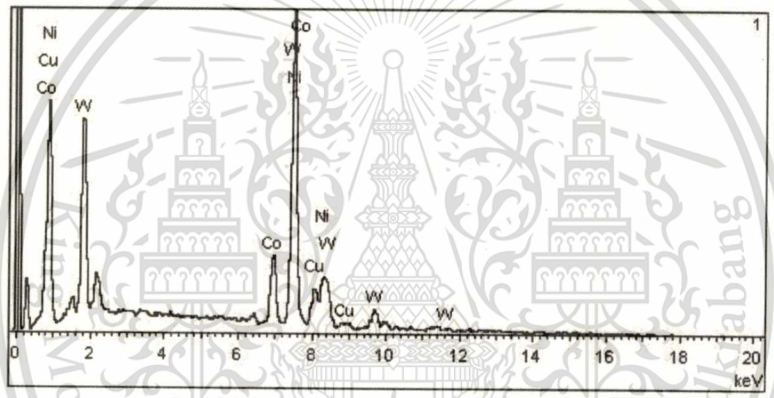

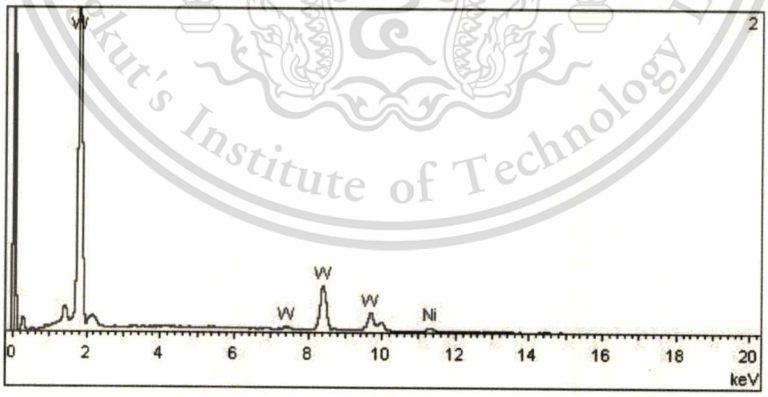

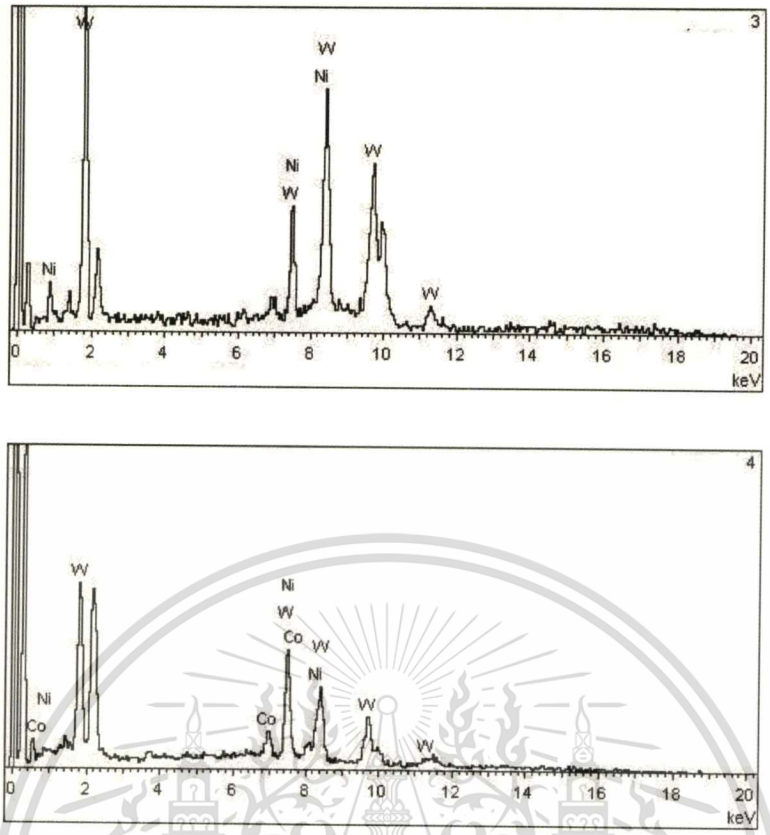

Figure 4.20 EDS patterns of W-(Ni-Cu-Co) specimen sintered at 1400°C for 3 hours.

Table 4.2 Structure elements of sintered W-(Ni-Cu-Co) specimen in **Figure 4.20**.

No.	Structure elements, wt%			
	W	Ni	Cu	Co
1	28.95	53.57	7.78	9.70
2	99.2	0.80	-	-
3	65.87	34.13	-	-
4	48.95	43.81	-	7.23

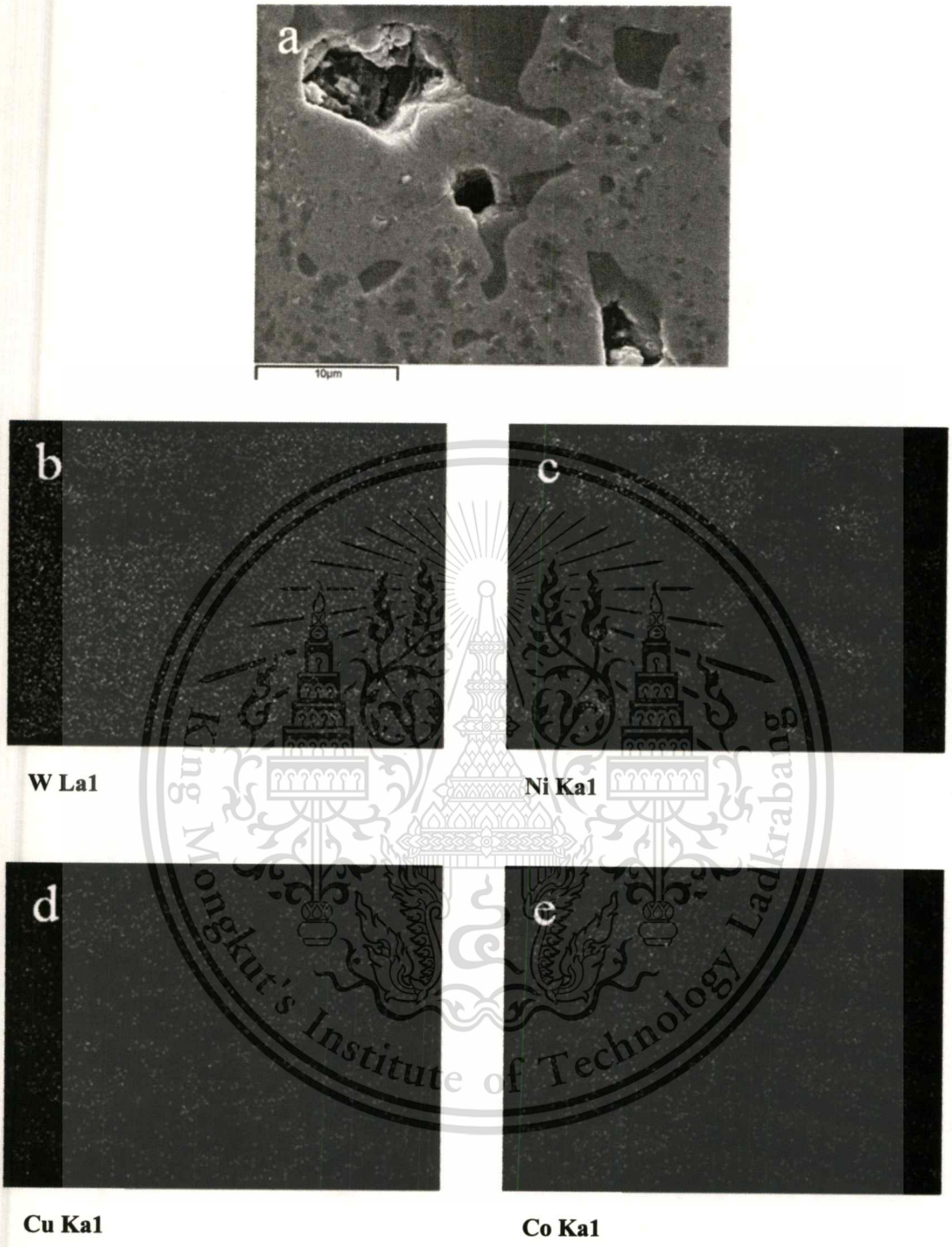

Figure 4.21 Elemental mapping of the W-(Ni-Cu-Co) specimen sintering at 1400°C for 3 hours; (a) SEM image, (b) W distribution, (c) Ni distribution, (d) Cu distribution and (e) Co distribution.

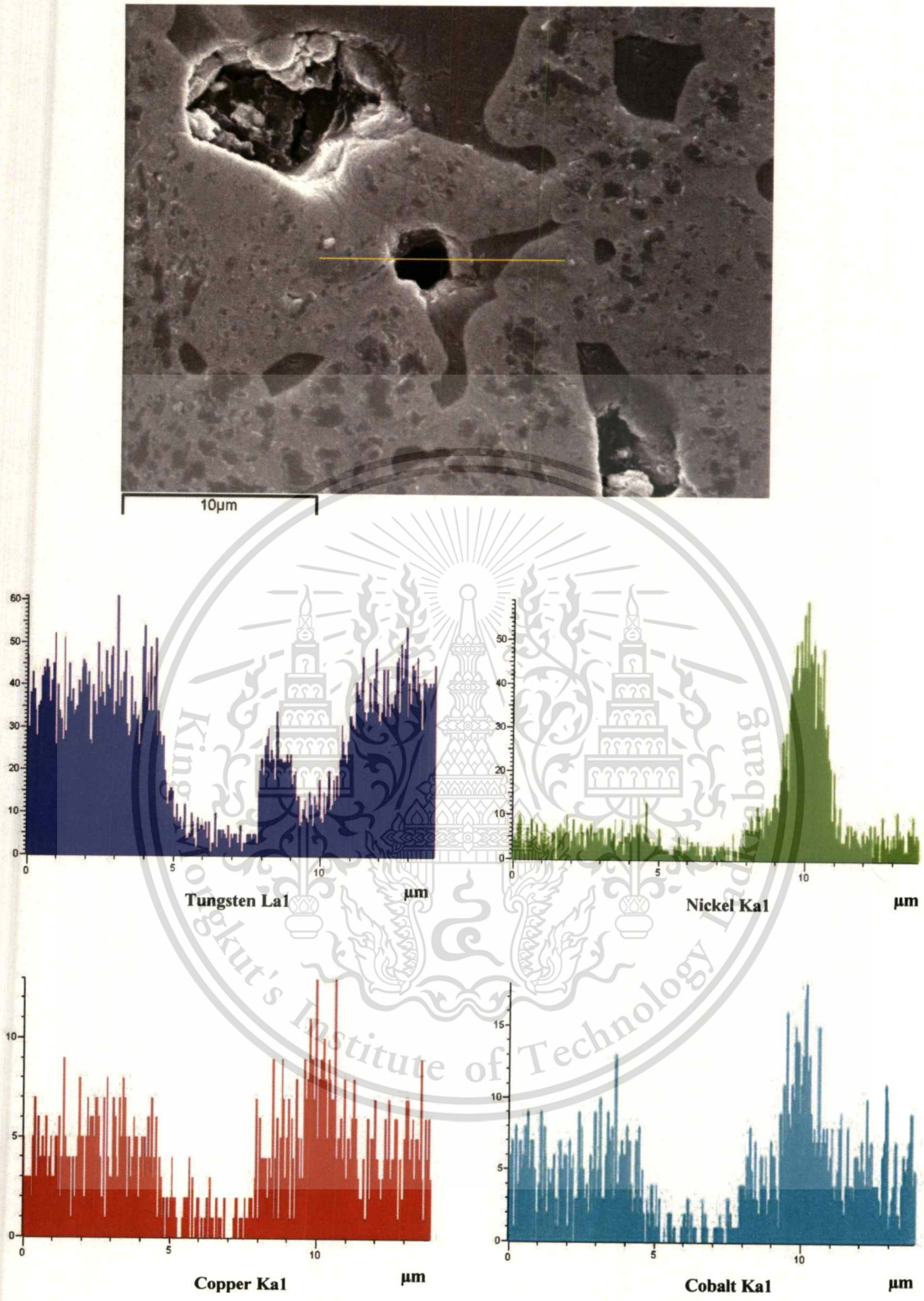

Figure 4.22 The line profile analysis on compositions across the tungsten particles and metal binder liquid phase of the W-(Ni-Cu-Co) specimen sintered at 1400°C for 3 hours.

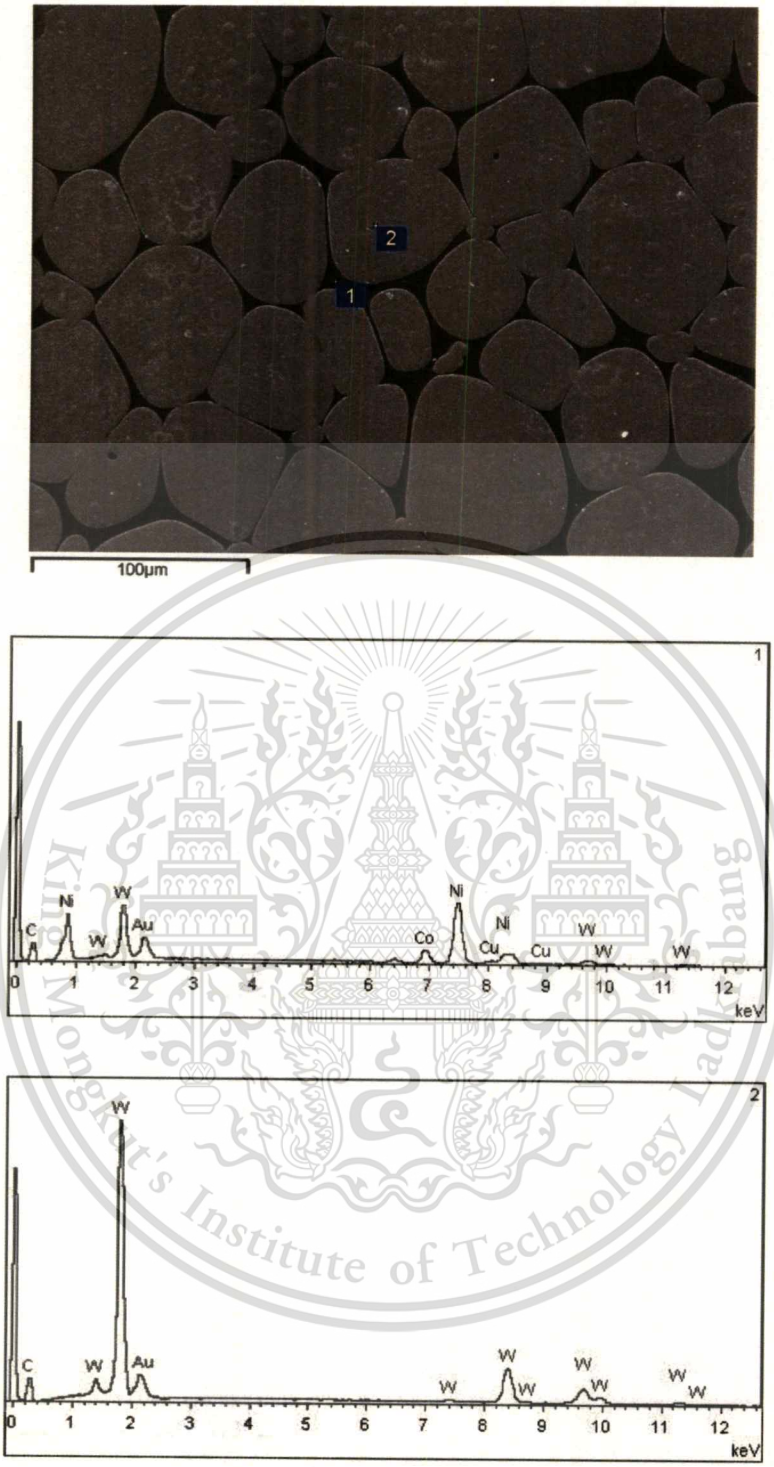

Figure 4.23 EDS patterns of W-(Ni-Cu-Co) specimen sintered at 1450°C for 3 hours.

Table 4.3 Structure elements of sintered W-(Ni-Cu-Co) specimen in **Figure 4.23**.

No.	Structure elements, wt%			
	W	Ni	Cu	Co
1	34.28	53.68	2.38	9.66
2	100	-	-	-

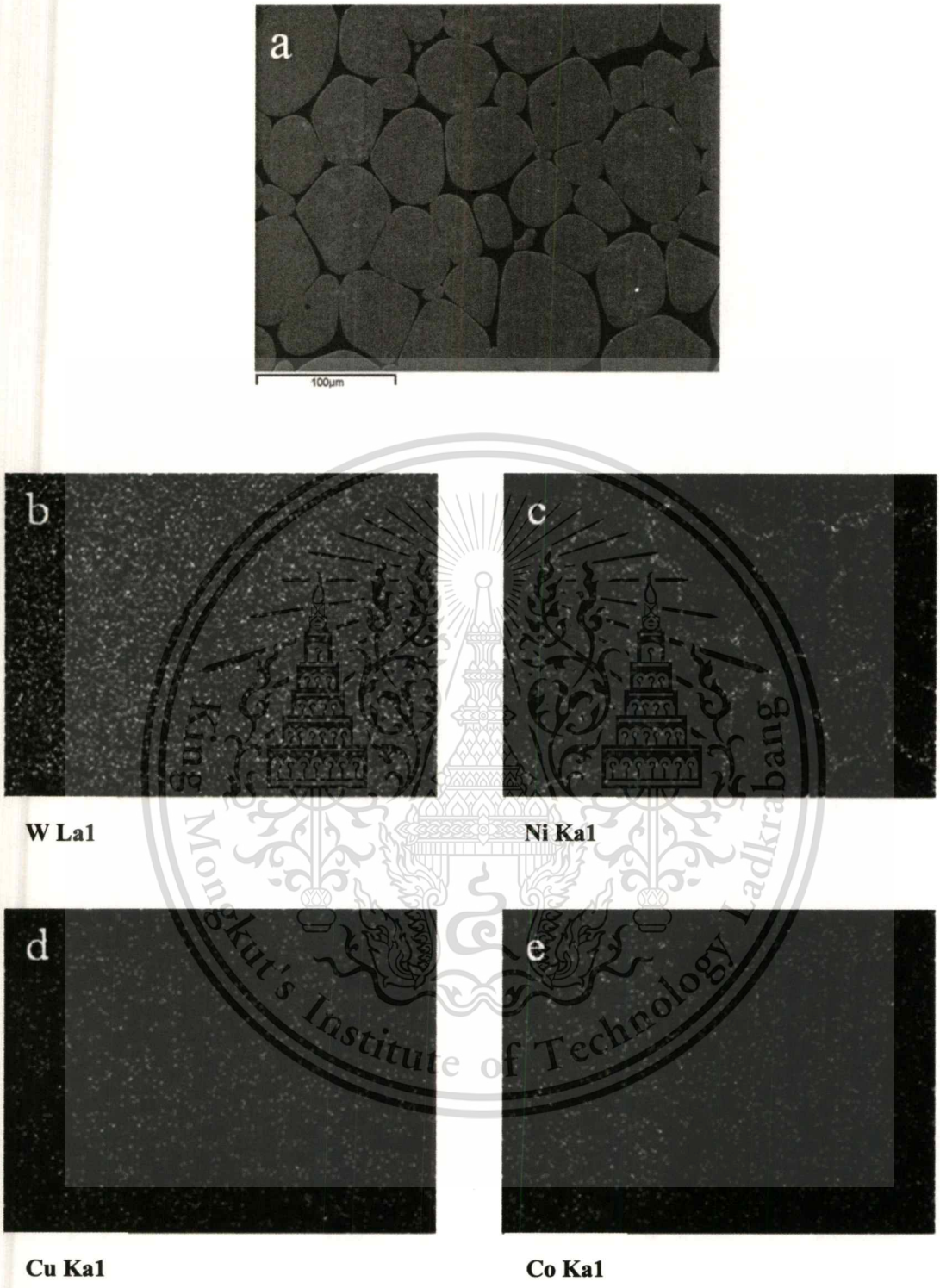

Figure 4.24 Elemental mapping of the W-(Ni-Cu-Co) specimen sintering at 1450°C for 3 hours; (a) SEM image, (b) W distribution, (c) Ni distribution, (d) Cu distribution and (e) Co distribution.

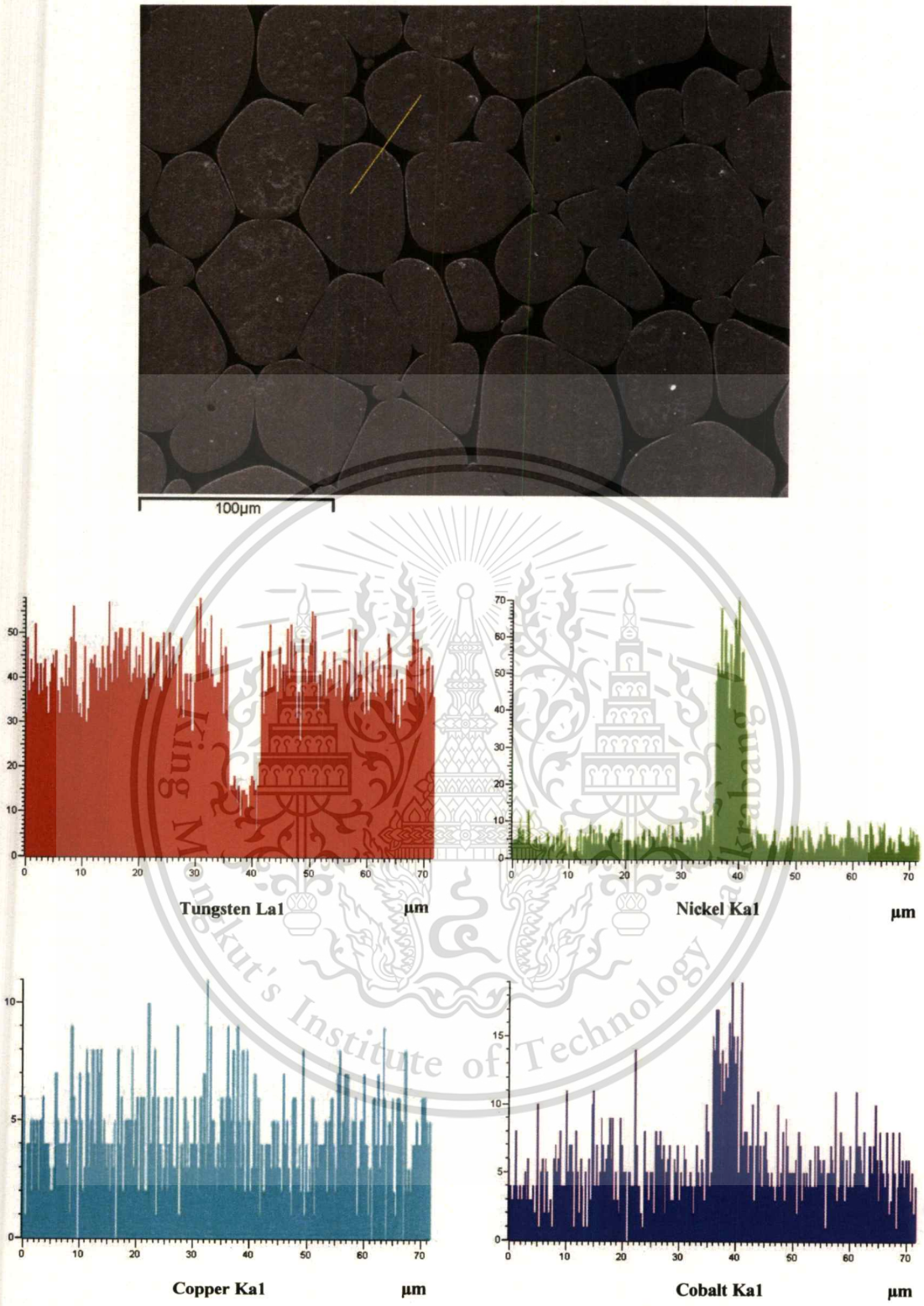

Figure 4.25 The line profile analysis on compositions across the tungsten particles and metal binder liquid phase of the W-(Ni-Cu-Co) specimen sintered at 1450°C for 3 hours.

4.4 Effects of Sintering Temperatures and Sintering Times on Mechanical Properties

Ultimate tensile strength (UTS), Yield strength, Modulus and Hardness of the W-(Ni-Cu-Co) specimens sintered under different conditions are shown in **Figure 4.26**, **4.27**, **4.28** and **4.29** respectively. From the results, it was found that the mechanical properties of W-(Ni-Cu-Co) specimens sintered under all conditions showed similar trends, in which mechanical properties increases with increasing sintering temperature. The W-(Ni-Cu-Co) specimens which were sintered at 1350 and 1400°C had much lower tensile properties than the specimens sintered at 1450°C. When the sintering temperature increases from 1350 to 1400°C, the strength slightly increases but dramatically increases when the sintering temperature increases from 1400 to 1450°C. The optimal mechanical properties with ultimate tensile strength of 776 MPa, yield strength of 562 MPa, modulus of 134 GPa and hardness of 105.9 HRB were obtained when the materials are sintered under sintering temperature of 1450°C for 3 hours. However, the mechanical properties are reduced when sintering time is raised further to 4 hours. It indicates that sintering for longer than 3 hours yielded sintered materials with inferior mechanical properties.

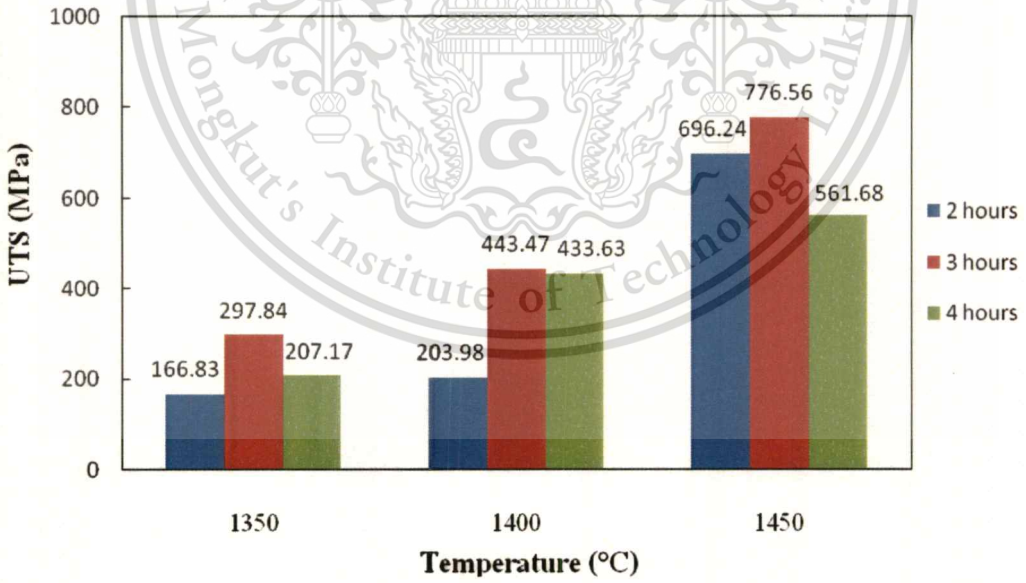

Figure 4.26 Ultimate tensile strength of W-(Ni-Cu-Co) specimens sintered at various conditions.

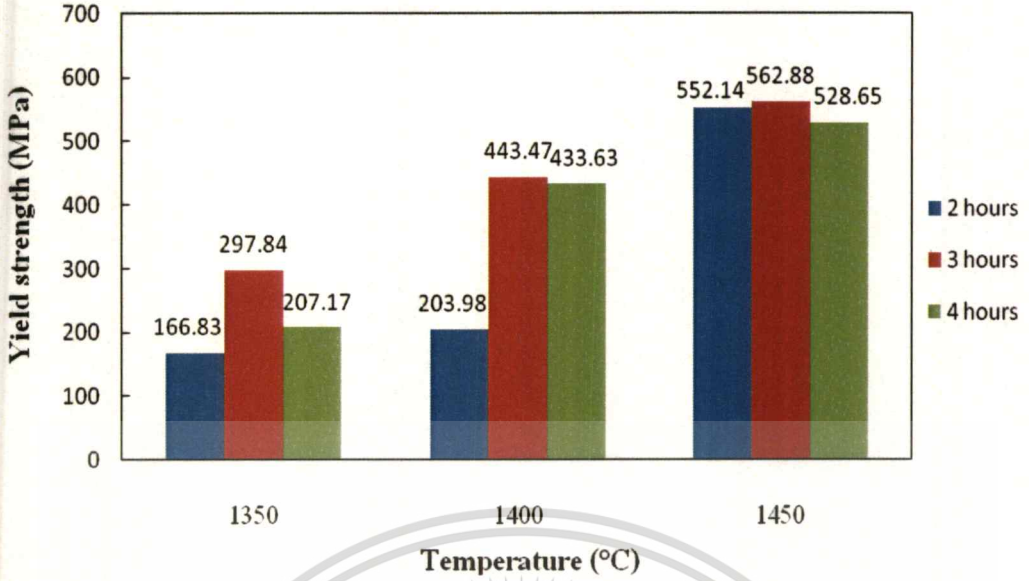

Figure 4.27 Yield strength of W-(Ni-Cu-Co) specimens sintered at various conditions.

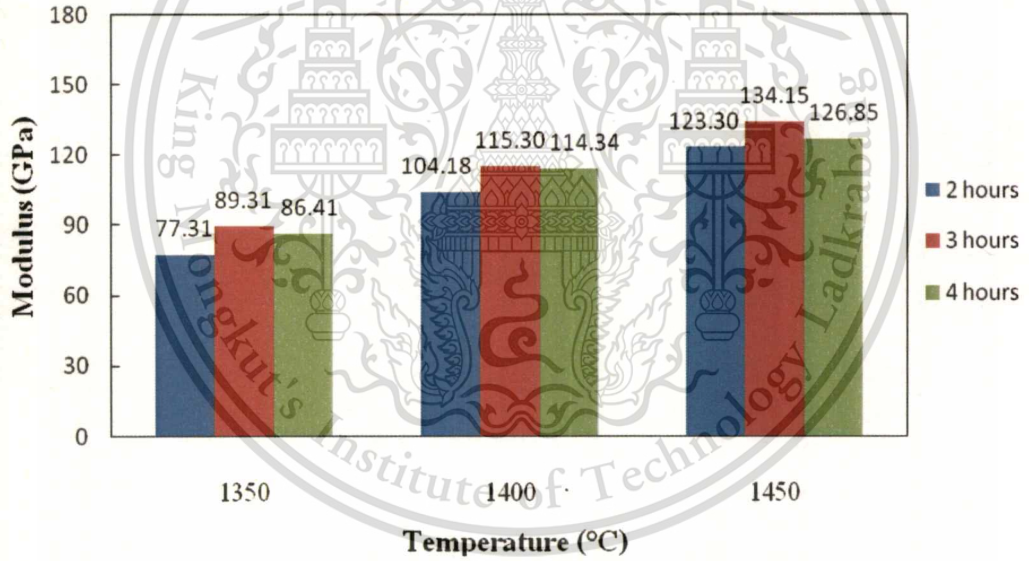

Figure 4.28 Modulus of W-(Ni-Cu-Co) specimens sintered at various conditions.

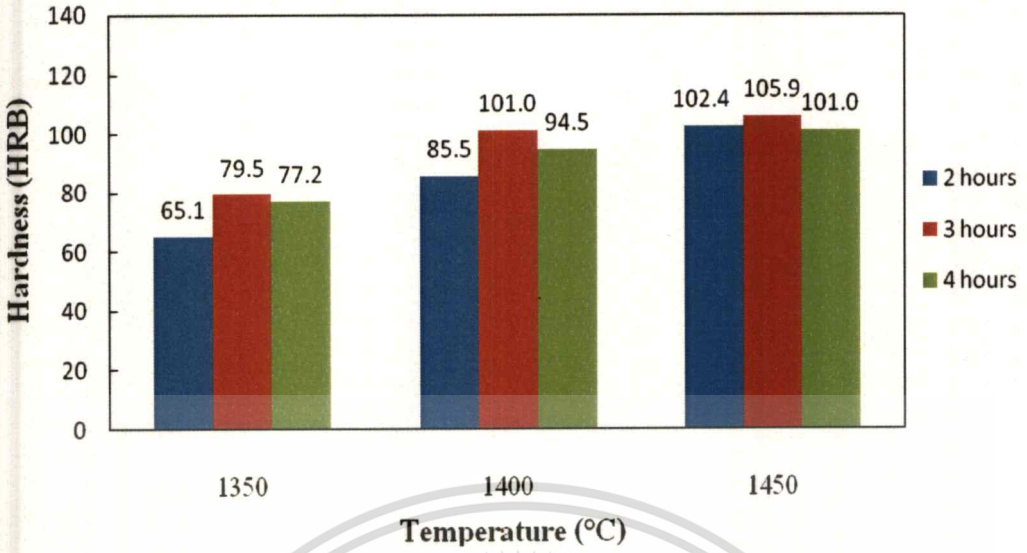

Figure 4.29 Rockwell hardness of W-(Ni-Cu-Co) specimens sintered at various conditions.

4.5 Relationship between Microstructure, Density and Mechanical Properties

The sintering temperature and sintering time affected directly the microstructure and hence affected the density and mechanical properties of W-(Ni-Cu-Co) specimens. At sintering temperatures of 1350 and 1400°C, the microstructures showed the contiguity between the solid tungsten particles and the Ni-Cu-Co metal binder particles (**Figure 4.14 and 4.15**). However, porosity still existed and the tungsten particles were not penetrated. These microstructures indicate that liquid phase sintering has not occurred at these sintering temperatures (Wu *et al.*, 2003). The grain growth of tungsten particles and decrease of porosity are observed with increase sintering time from 2 to 3 hours. This shows that the grain growth occurs with the increase in density (porosity reduction/elimination). The density and tensile properties of sintered W-(Ni-Cu-Co) specimens were sensitive to the sintering temperature ranged from 1400 to 1450°C. With increasing sintering temperature from 1400 to 1450°C with sintering time for 3 hours, the density increased from 16.64 to 18.02 g/cm^3 and the UTS dramatically increased from 443 to 776 MPa due to the sintering temperature of 1450°C, the significant microstructure change is observed and the porosity is remarkably reduced (**Figure 4.16**). These phenomena indicate that the sintering temperature reaches the solid to liquid phase transition temperature (Lee *et al.*, 2007). Thus, the Ni-Cu-Co metal binder liquid phase occurs, then penetrates and fills the pores between solid tungsten particles (German, 1994). Therefore, the distribution of tungsten particles is more uniform, leading to the increase of density and mechanical properties. At sintering temperature of

1450°C with increasing of sintering time from 3 to 4 hours, the presence of defect and tungsten particles coalescence were observed (**Figure 4.16 (i)**), that may cause inferior of density (from 18.02 to 17.76 g/cm^3) and mechanical properties (with UTS from 776 to 561 MPa). However, when compared to the tensile properties, hardness of sintered W-(Ni-Cu-Co) specimens did not significantly change. Usually, the mechanical properties of tungsten heavy alloy are explained in terms of microstructure parameters. The high strength tungsten heavy alloy is obtained by decreasing tungsten particles size (Akhtar, 2008).

The experimental results show that the W-(Ni-Cu-Co) specimens, sintered at 1450°C for 3 hours, have the highest sintered density and mechanical properties. Sintering for 4 hours yields the material with porosity and inferior mechanical properties due to porosity at tungsten grain corners. It was interesting to find out what would happen to the W-(Ni-Cu-Co) specimens sintered at 1450°C for sintering times longer than 4 hours. Sintering for 6 and 8 hours were then further conducted.

4.6 Effects of Longer Sintering Times

Densities of the W-(Ni-Cu-Co) specimens sintered at 1450°C for different sintering times in the range of 2 to 8 hours are shown in **Figure 4.30**. It was found that for sintering times longer than 3 hours, sintered density decreased with the increasing of sintering time and the lowest sintered density (16.90 g/cm^3) was observed at the sintering time of 8 hours. The dimensional change measurement shows that the shrinkage rate was decreased with increasing sintering times. This is in agreement with the sintered density shown in **Figure 4.30**. The shrinkage along grip width, gauge width, length and thickness at 1450°C for different sintering times are shown in **Figure 4.31**, **4.32**, **4.33** and **4.34** respectively. The effect of longer sintering times on mechanical properties with ultimate tensile strength, yield strength, modulus and hardness of W-(Ni-Cu-Co) specimens sintered at 1450°C with various sintering times are presented in **Figure 4.35**, **4.36, 4.37** and **4.38** respectively. The mechanical properties showed a similar trend to that of the sintered densities, i.e., mechanical properties decreased with increasing sintering time. It was found that mechanical properties dramatically decreased when sintering times longer than 3 hours were employed. With increasing sintering time from 3 to 4 hours, the UTS decreases from 776 to 561 MPa. The tungsten grain connectivity obviously increases at sintering times longer than 4 hours, the UTS continuously decreases from 561 to 256 MPa and specimens sintered at 1450°C

for 8 hours were brittle. However, when compared to the tensile properties, hardness of these sintered materials is less sensitive to longer sintering times. This may be attributed to the fact that hardness of the material is mainly contributed by tungsten grains.

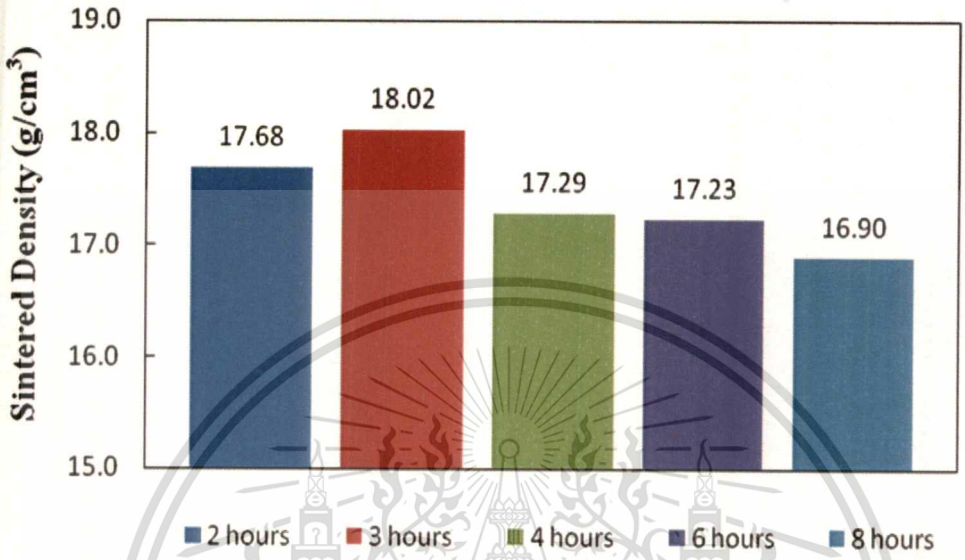

Figure 4.30 Sintered density of W-(Ni-Cu-Co) sintered at 1450°C for different sintering times.

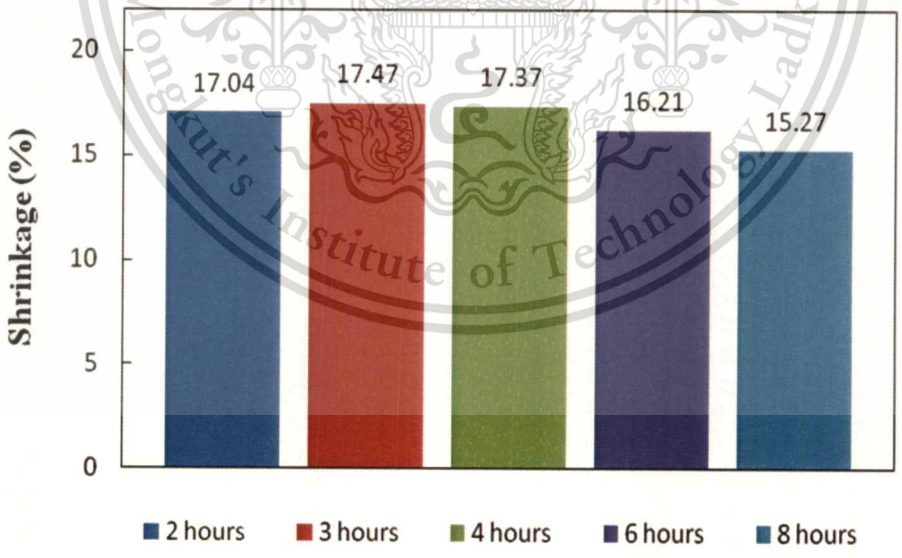

Figure 4.31 The shrinkage along grip width of W-(Ni-Cu-Co) specimens sintered at 1450°C for different sintering times.

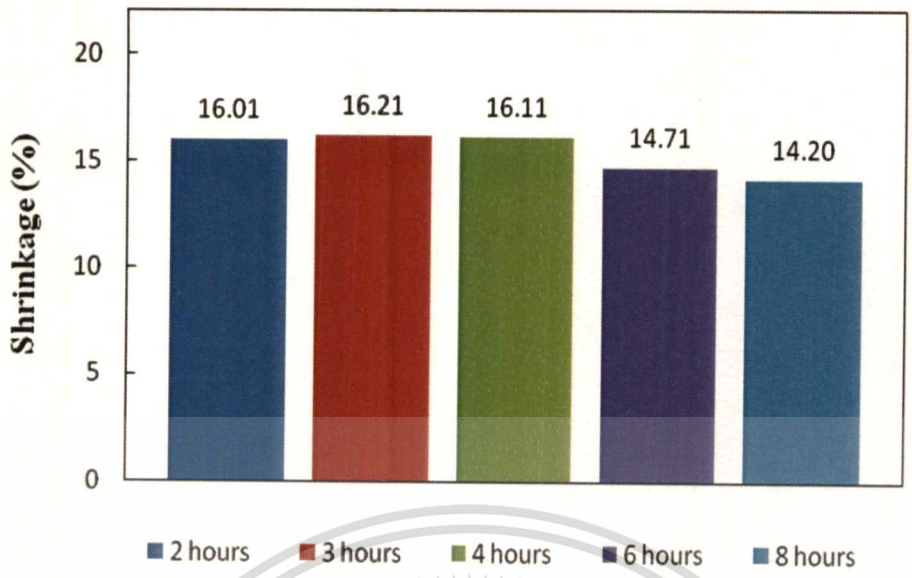

Figure 4.32 The shrinkage along gauge width of W-(Ni-Cu-Co) specimens sintered at 1450°C for different sintering times.

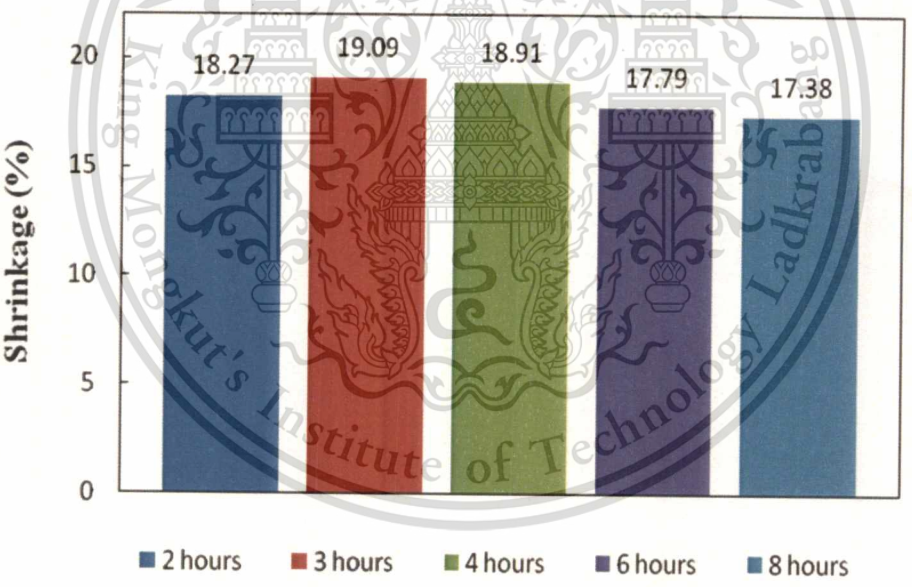

Figure 4.33 The shrinkage along length of W-(Ni-Cu-Co) specimens sintered at 1450°C for different sintering times.

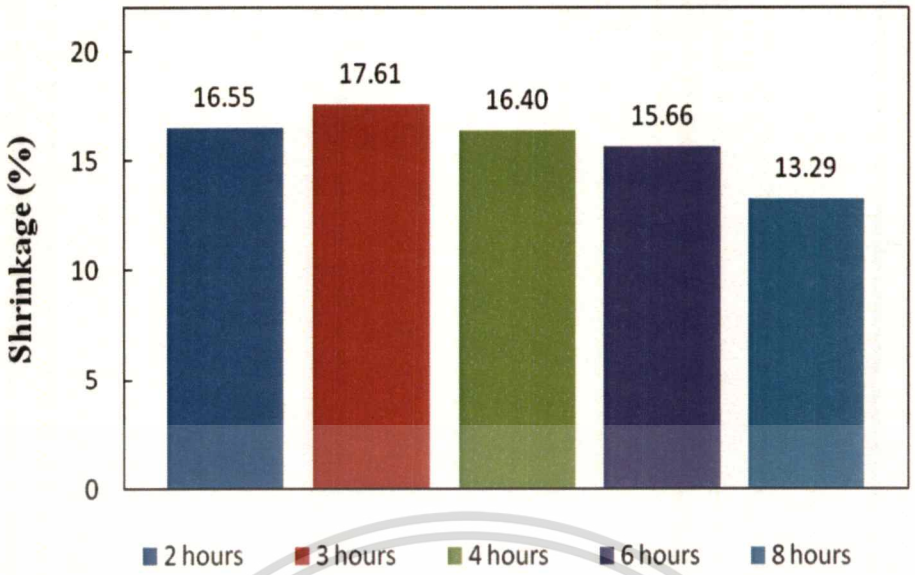

Figure 4.34 The shrinkage along thickness of W-(Ni-Cu-Co) specimens sintered at 1450°C for different sintering times.

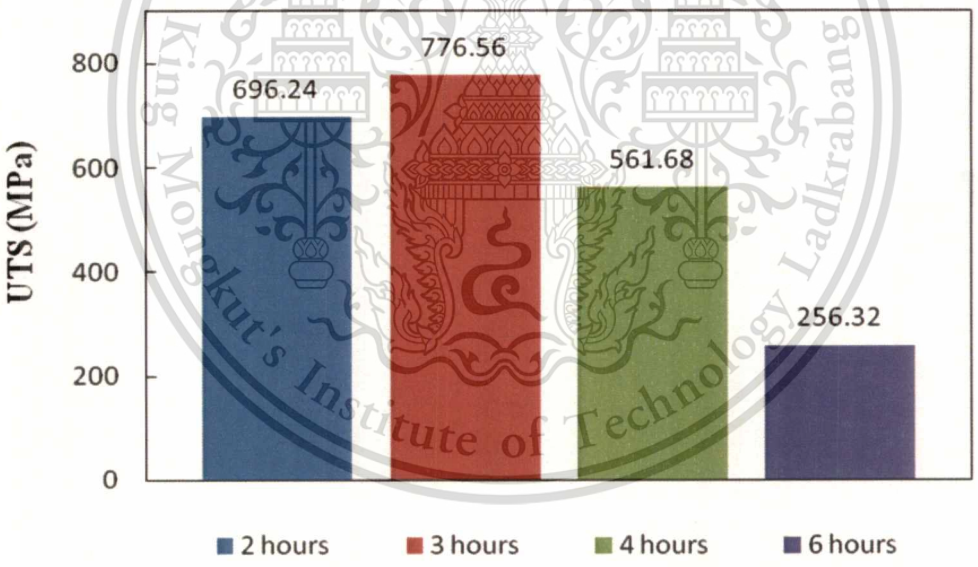

Figure 4.35 Ultimate tensile strength of W-(Ni-Cu-Co) specimens sintered at 1450°C for different sintering times.

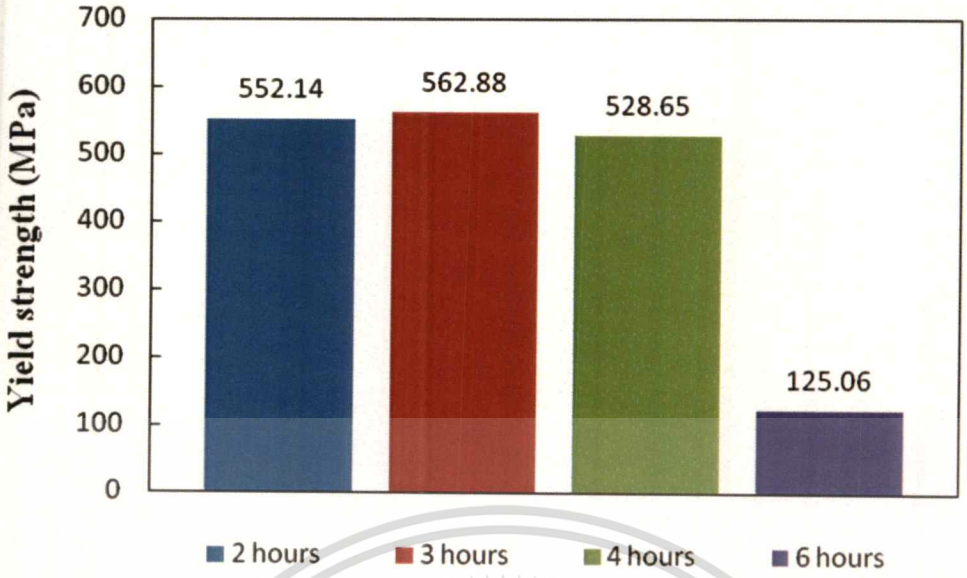

Figure 4.36 Yield strength of W-(Ni-Cu-Co) specimens sintered at 1450°C for different sintering times.

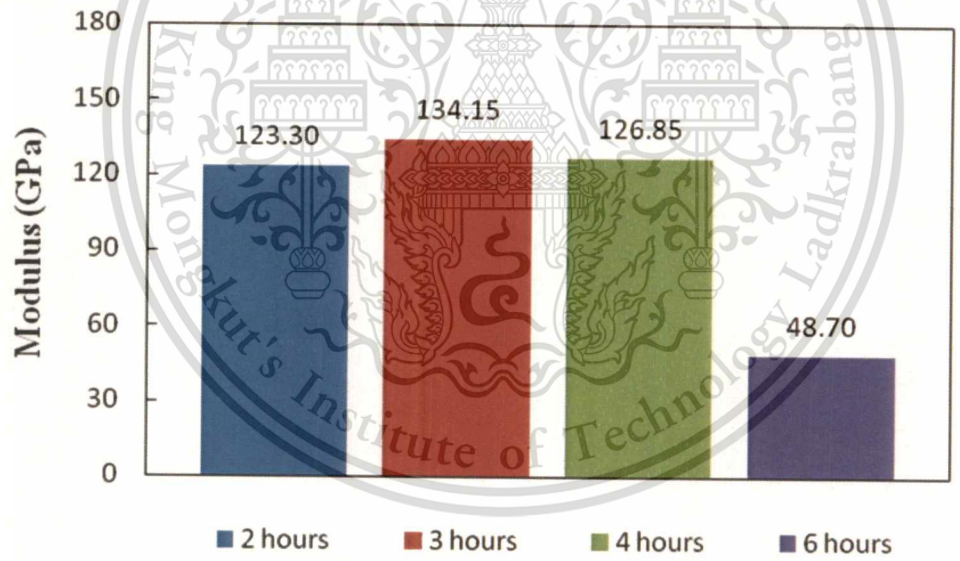

Figure 4.37 Modulus of W-(Ni-Cu-Co) specimens sintered at 1450°C for different sintering times.

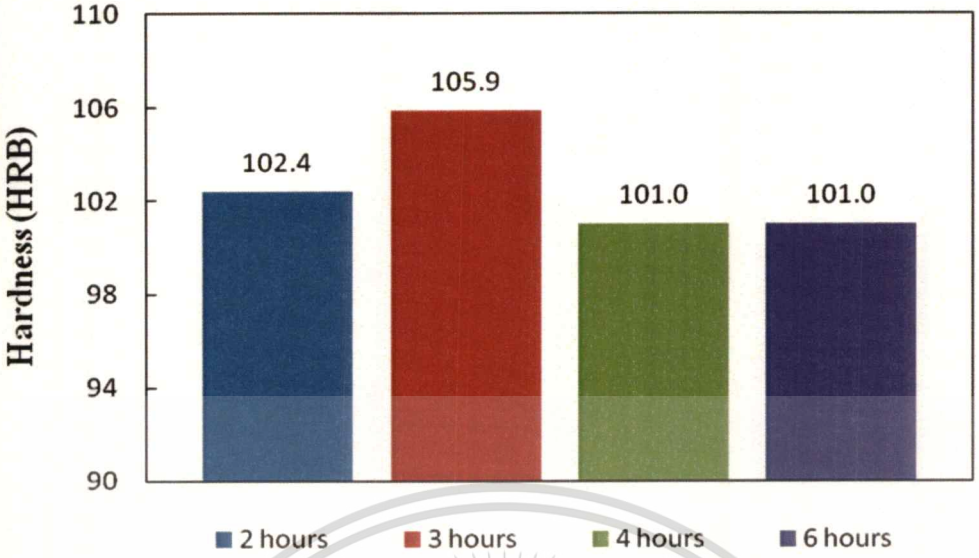

Figure 4.38 Hardness of W-(Ni-Cu-Co) specimens sintered at 1450°C for different sintering times.

Microstructures of the specimens sintered at 1450°C for 6 and 8 hours are shown in **Figure 4.39** and **4.40** respectively. **Figure 4.41** illustrates microstructures of W-(Ni-Cu-Co) specimens sintered at 1450°C for various sintering times. It can be seen that the microstructures of W-(Ni-Cu-Co) specimens sintered at 1450°C for 2 and 3 hours, Ni-Cu-Co formed uniform liquid phase and provided homogeneous distribution between matrix and tungsten particles. Increase of sintering times showed no improvement of tensile strengths. For too long sintering (6 and 8 hours), it was found that porosity growth and coalesced to each other between tungsten particles were observed. Coalescence occurs (**Figure 4.42**) at grain contacts where the grains merge into other neighbor grains by elimination of the grain boundary (Bollina *et al.*, 2004). Coalescence was observed in the microstructures of W-(Ni-Cu-Co) specimens sintered at 1450°C for 6 and 8 hours as seen in **Figure 4.39** and **4.40** respectively. Sintered specimens were yielded brittle with low mechanical properties. The sintered density decreased is attributed to porosity generation. For 4 hours sintering, porosity at tungsten grain corners is resulted from dissolution of metal binders into tungsten grains (**Figure 4.16 (i)**). For sintering longer than 4 hours, the tungsten grain corner pores are reduced by materials transport from tungsten grains to the corner pores. Solid-state sintering between tungsten grains also occurs. Both materials transport and solid-state sintering cause porosity inside the tungsten grains. The tungsten grain internal pores and grain growth are the main cause of lower sintered density and inferior mechanical properties (Yimin *et al.*, 1998).

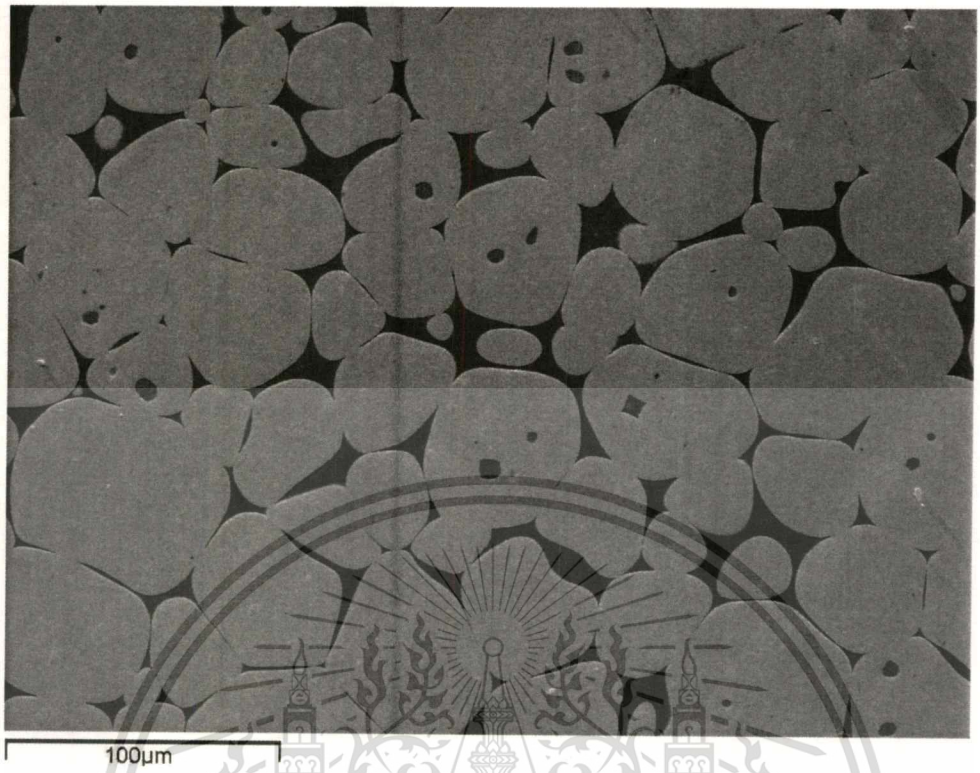

Figure 4.39 Microstructure of W-(Ni-Cu-Co) specimen sintered at 1450°C for 6 hours.

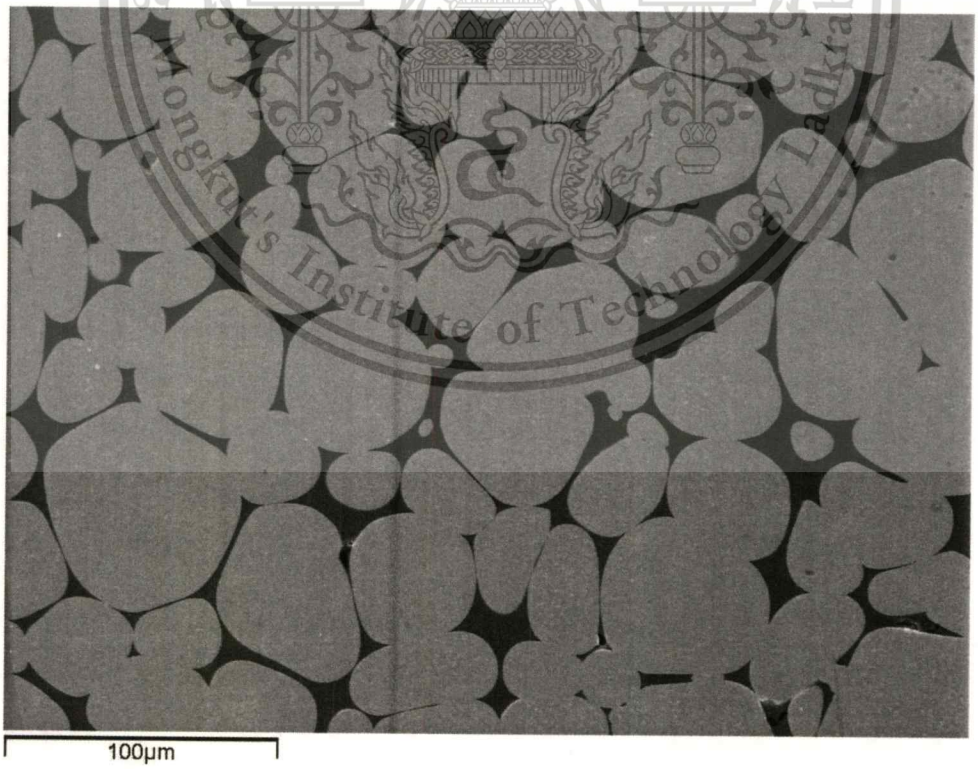

Figure 4.40 Microstructure of W-(Ni-Cu-Co) specimen sintered at 1450°C for 8 hours.

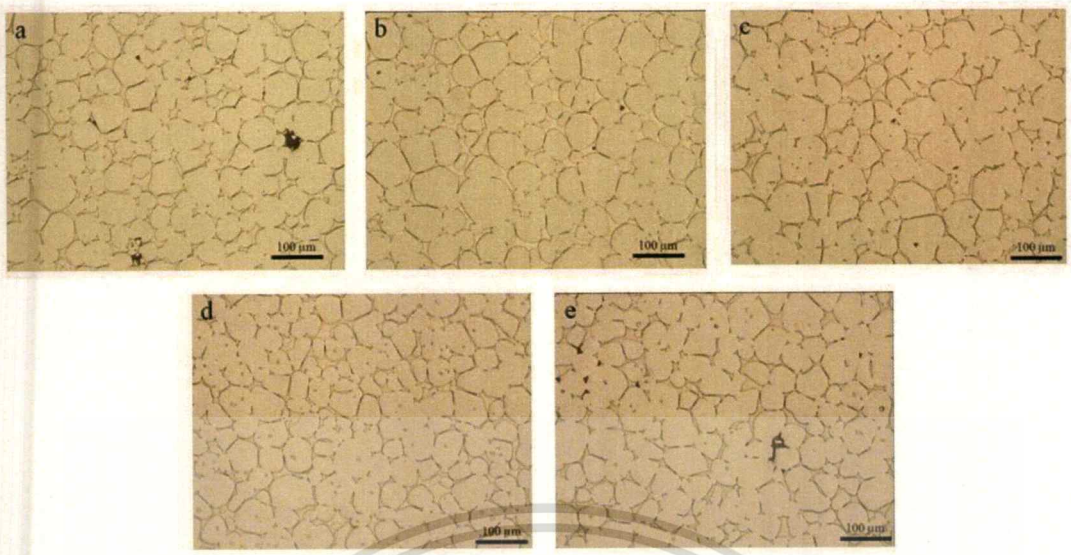

Figure 4.41 Microstructures of W-(Ni-Cu-Co) specimen sintered at 1450°C for (a) 2 hours, (b) 3 hours, (c) 4 hours, (d) 6 hours, (e) 8 hours.

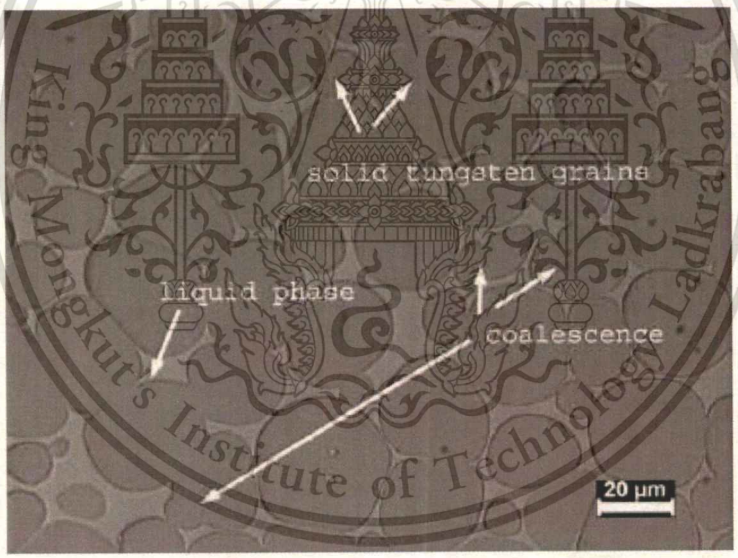

Figure 4.42 The coalescence of small grains into bigger grains of microstructures of 93W-Ni-Fe(7:3) alloy sintered at 1500°C for 30 min (Bollina *et al.*, 2004).

Chemical analyze was also performed with the sintered W-(Ni-Cu-Co) specimens sintered at 1450°C for 6 and 8 hours by using energy dispersive spectroscopy with modes of quantitative analysis. The results are illustrated in **Figure 4.43** and **4.44**. **Table 4.4** and **4.5** show the structure elements of **Figure 4.43** and **4.44** respectively. The results show that the tungsten content dissolved in Ni-Cu-Co phase decreased from 34.28 to 20.16wt.% when increased sintering time from 3 to 6 hours and decreased to 6.33wt.% in the Cu-depleted Ni-Co binder when sintering was further increased to 8 hours. The sintering temperature range from 1400 to 1450°C was a period of rapid decreasing of copper content in metal binder phase (from 7.78 to 2.38wt.%). Dramatically decreasing of copper content and porosity in microstructures from this period sintering temperatures corresponding to the study of Ho *et al.* (2008) that increasing sintering temperatures, less copper was detected. Ho *et al.* (2008) reported the reduction in porosity had an effect on the amount of copper that could be infiltrated to form the final product. At sintering temperature of 1450°C with increasing sintering times from 3 to 6 and 8 hours, the copper content decreased to 0.53 and 0.45wt.%. In contrast, the Ni content was increased from 53.68 to 66.73wt.% and increased to 80.73wt.% at sintering time for 8 hours. In addition, the lowest density and existence of pores at the tungsten grains were observed from microstructure with the tungsten content of 6.33wt.%. XRD pattern of W-(Ni-Cu-Co) specimens sintered at 1400°C for 3 hours is shown in **Figure 4.45**. **Figure 4.46** and **4.47** present XRD patterns of W-(Ni-Cu-Co) specimens sintered at 1450°C for 3 and 6 hours. For specimens sintered at 1400°C for 3 hours, XRD examination detected only two phase in the sintered specimen. Only W and $Cu_{0.4}W_{0.6}$ peaks observed. With increasing sintering temperature from 1400 to 1450°C for 3 hours, a large amount of new phases of Co_7W_6 and $Cu_{0.81}Ni_{0.19}$ appeared in the pattern with strong intensity, indicating that significant amount of Co_7W_6 and $Cu_{0.81}Ni_{0.19}$ had formed at sintering temperature 1450°C for 3 hours. At sintering temperature of 1450°C for 6 hours, XRD examination clarifies only two phases of W and $Cu_{0.4}W_{0.6}$. The patterns for the sintered specimens sintered at 1400°C for 3 hours and at 1450°C for 6 hours are essentially the same. The strongest peak is tungsten peak at a 2θ angle of ~40.4, 58, 73 and 87°. Weak peaks of $Cu_{0.4}W_{0.6}$ are observed at 2θ angle of ~58.5, 73.5 and 87.3°.

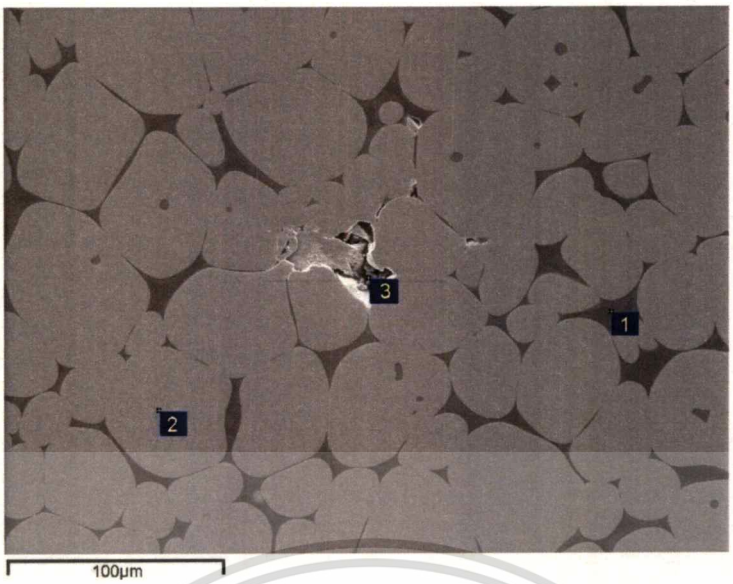

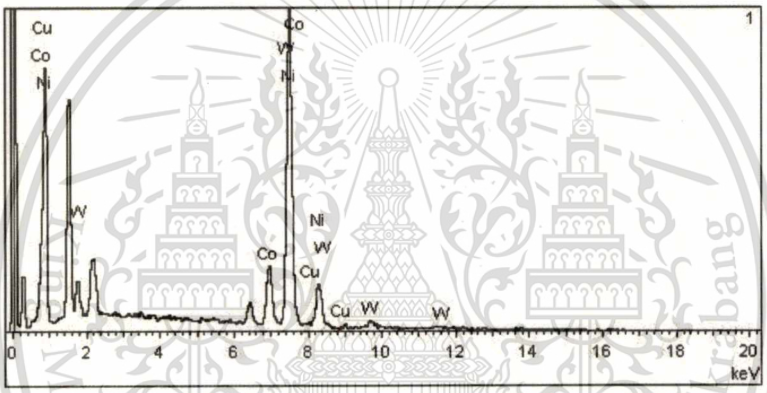

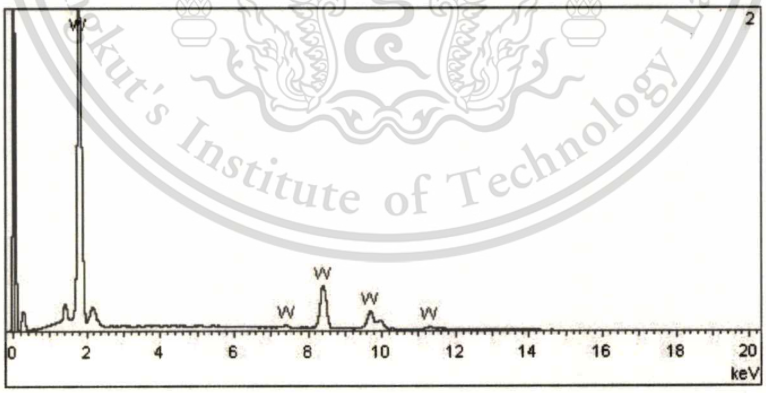

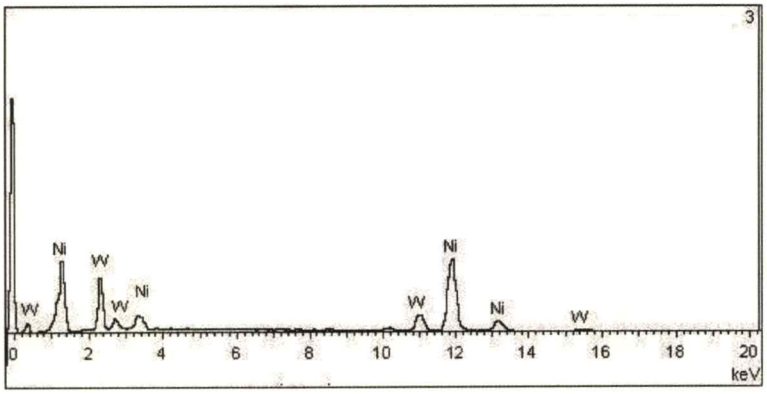

Figure 4.43 EDS patterns of W-(Ni-Cu-Co) specimen sintered at 1450°C for 6 hours.

Table 4.4 Structure elements of sintered W-(Ni-Cu-Co) specimen in **Figure 4.43**.

No.	Structure elements, wt%			
	W	Ni	Cu	Co
1	20.16	66.73	0.53	12.58
2	100	-	-	-
3	30.53	69.47	-	-

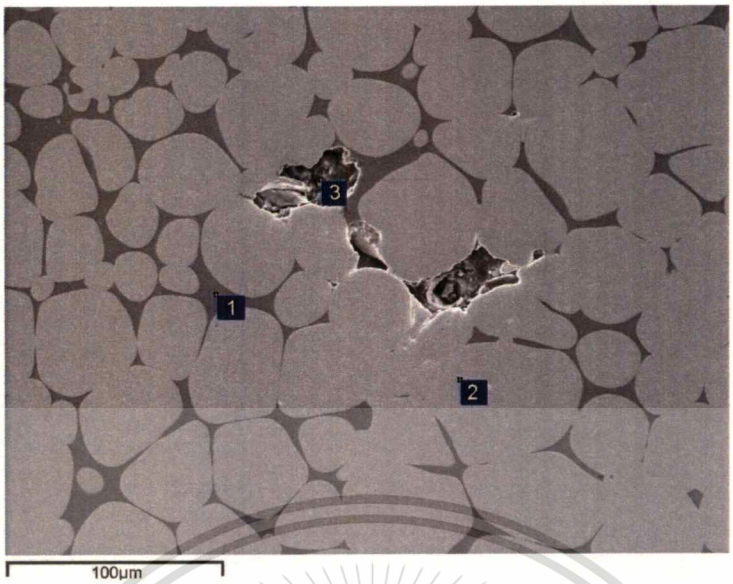

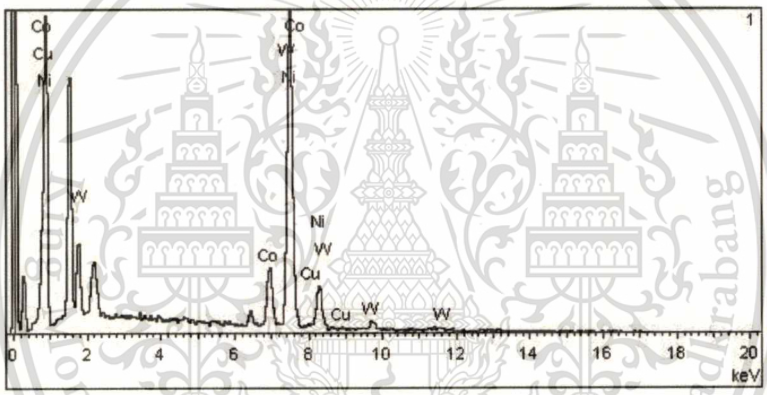

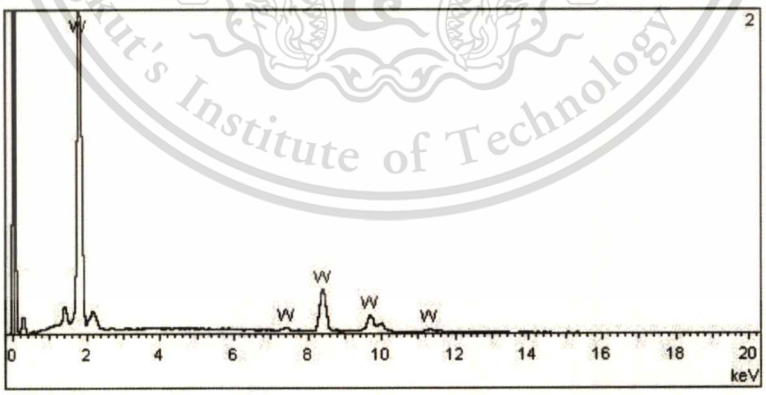

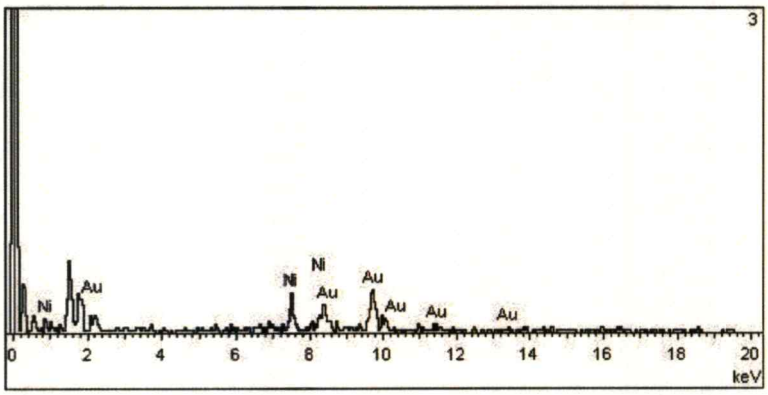

Figure 4.44 EDS patterns of W-(Ni-Cu-Co) specimen sintered at 1450°C for 8 hours.

Table 4.5 Structure elements of sintered W-(Ni-Cu-Co) specimen in **Figure 4.44**.

No.	Structure elements, wt%			
	W	Ni	Cu	Co
1	6.33	80.73	0.45	12.49
2	100	-	-	-
3	-	74.04	-	-

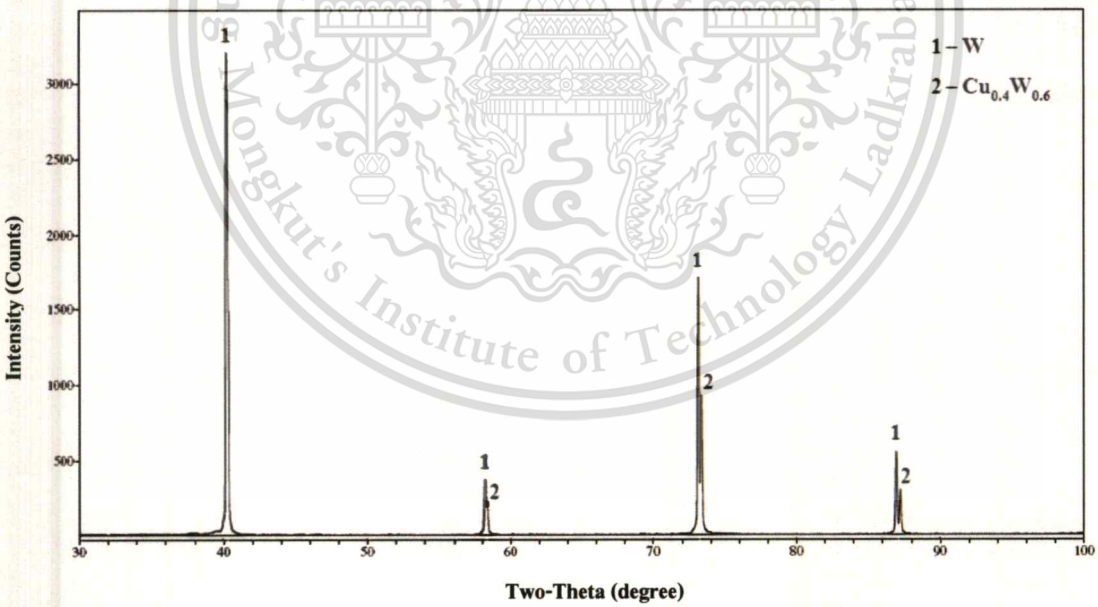

Figure 4.45 XRD pattern of W-(Ni-Cu-Co) specimen sintered at 1400°C for 3 hours.

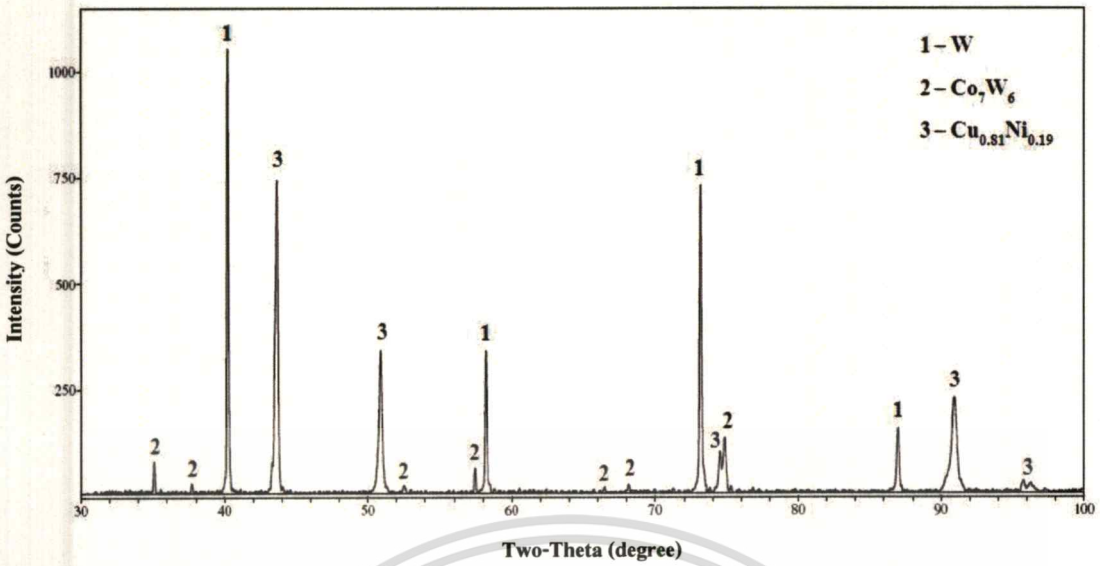

Figure 4.46 XRD pattern of W-(Ni-Cu-Co) specimen sintered at 1450°C for 3 hours.

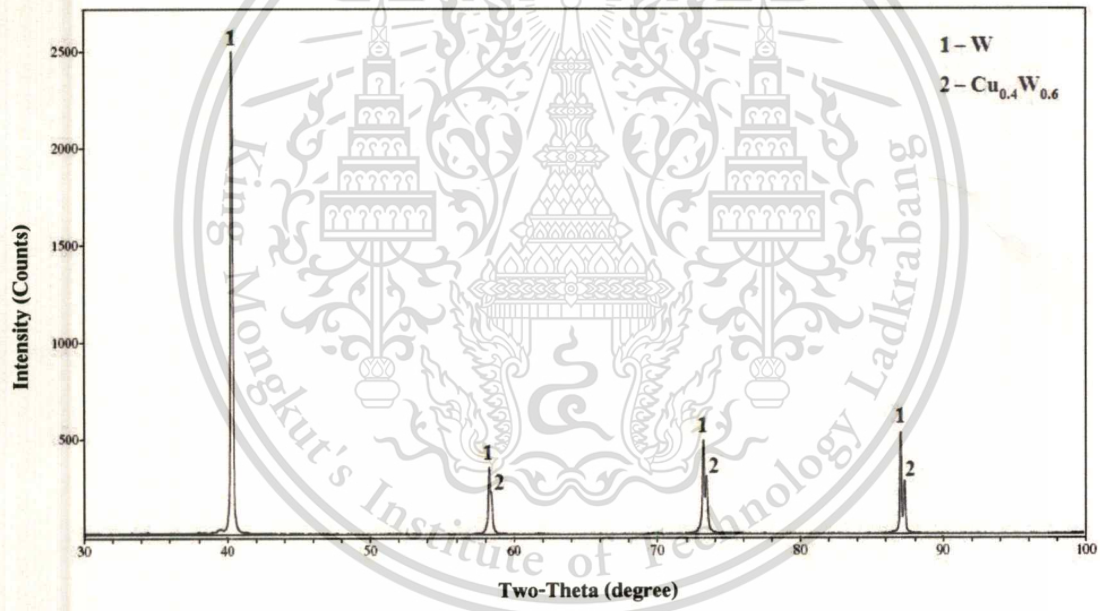

Figure 4.47 XRD pattern of W-(Ni-Cu-Co) specimen sintered at 1450°C for 6 hours.

4.7 Fractography

Scanning electron micrograph of the fracture surfaces of W-(Ni-Cu-Co) specimens sintered at different sintering temperatures and sintering times are shown in **Figure 4.48-4.51**. The tungsten particles appear in grey and the metal binder phase appear in light color. Akhtar (2008) reported that there are four possible fracture paths for tungsten heavy alloy microstructure: (1) matrix failure, (2) tungsten cleavage, (3) tungsten-tungsten interface failure and (4) tungsten-matrix failure. **Figure 4.48** shows fracture surface of W-(Ni-Cu-Co) specimens sintered at

1400°C for 3 hours. It can be seen from **Figure 4.48** that there are still many micro pores distributed on the fracture surface. During tensile testing, when the tensile stress is applied these pores act as cracks and cause failure in sintered specimens. The matrix failure and the tungsten-matrix failure are the main fracture of W-(Ni-Cu-Co) specimens sintered under this sintering condition. The W-(Ni-Cu-Co) specimens sintered at 1400°C for 3 hours failed at low stress (with UTS of 443 MPa) due to a large amount of pores and the inhomogeneous microstructure. With increasing sintering temperature from 1400 to 1450°C, liquid phase sintering occurs and a strong bond between tungsten and metal binder matrix is developed. This strong interfacial bond causes the increasing strength of W-(Ni-Cu-Co) specimens. Thus, at sintering temperature of 1450°C for 3 hours, the main fracture takes place at cleavage fracture of tungsten grains and interface between tungsten particles (**Figure 4.49**). The fracture takes place at cleavage fracture of tungsten grains is associated with higher tensile properties (with UTS increased to 776 MPa) (Das *et al.*, 2010). SEM of micrograph of the fracture surfaces of W-(Ni-Cu-Co) specimens sintered at 1450°C for 6 and 8 hours are shown in **Figure 4.50** and **4.51** respectively. It is obviously seen that the fracture changes from tungsten cleavage and interface between tungsten particles to matrix and tungsten-matrix failure which are associated with the lower tensile properties (UST decreased to 256 MPa and specimens sintered at 1450°C for 8 hours were brittle). SEM of micrograph of fracture surfaces correspond to the mechanical properties results in this experiment. These results indicate that the bonding strength between tungsten particles and the metal binder phase are strongly influence to the tensile properties. The optimal mechanical properties were obtained from specimens sintered at 1450°C for 3 hours (with UTS of 776 MPa) which is higher than those sintered other sintering conditions.

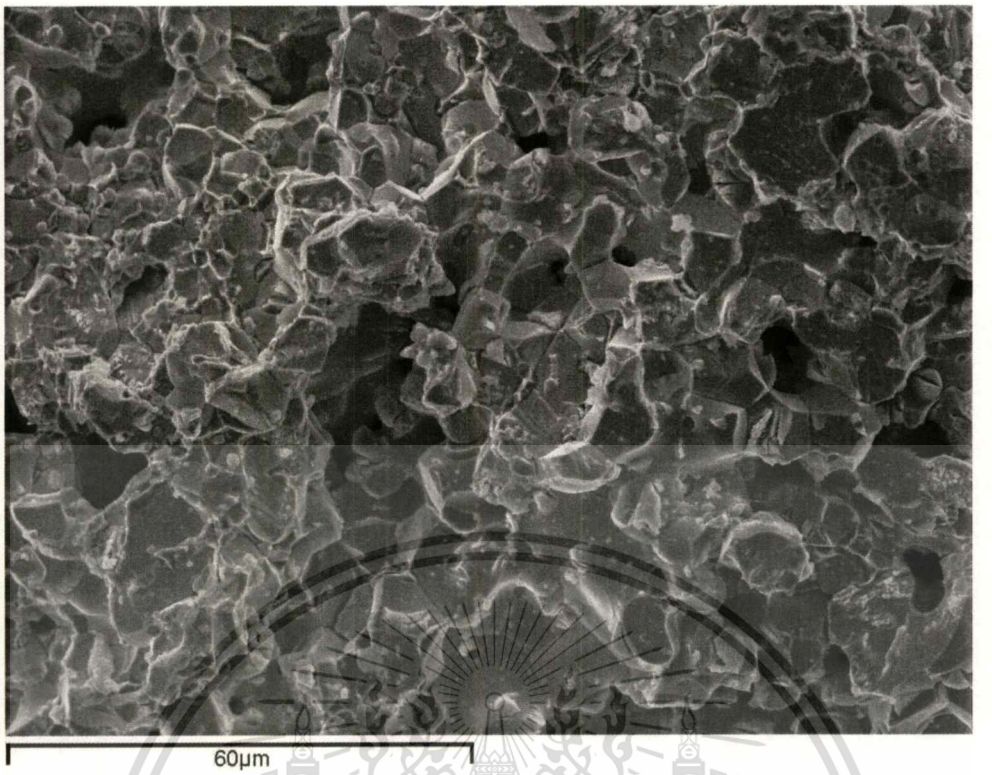

Figure 4.48 Fracture surface of W-(Ni-Cu-Co) specimens sintered at 1400°C for 3 hours.

Figure 4.49 Fracture surface of W-(Ni-Cu-Co) specimens sintered at 1450°C for 3 hours.

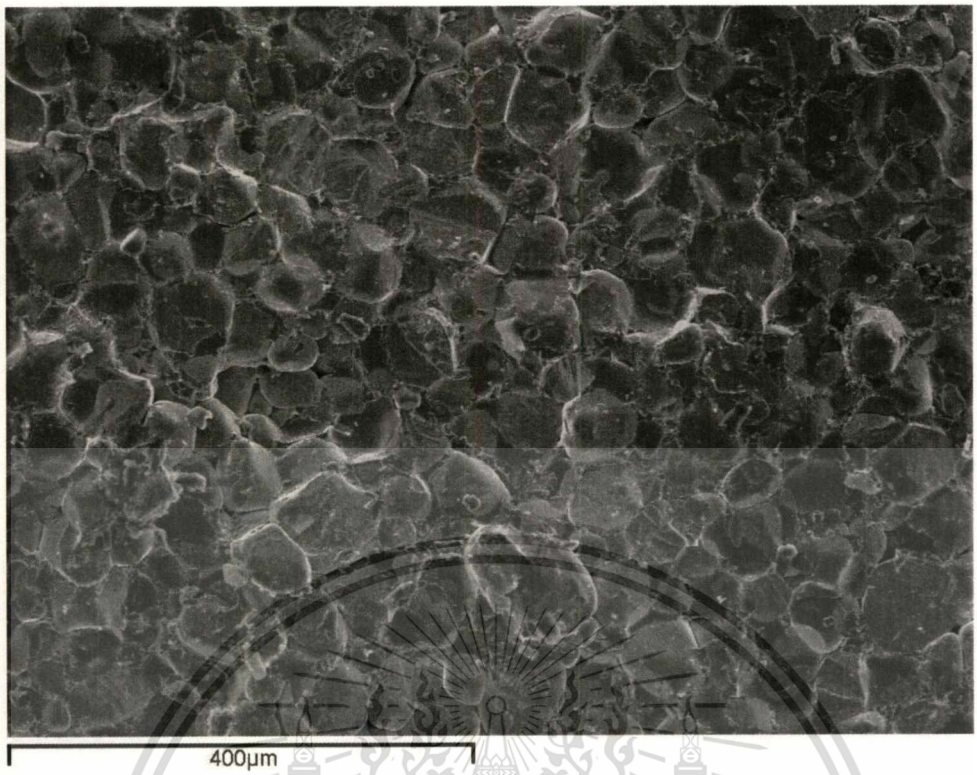

Figure 4.50 Fracture surface of W-(Ni-Cu-Co) specimens sintered at 1450°C for 6 hours.

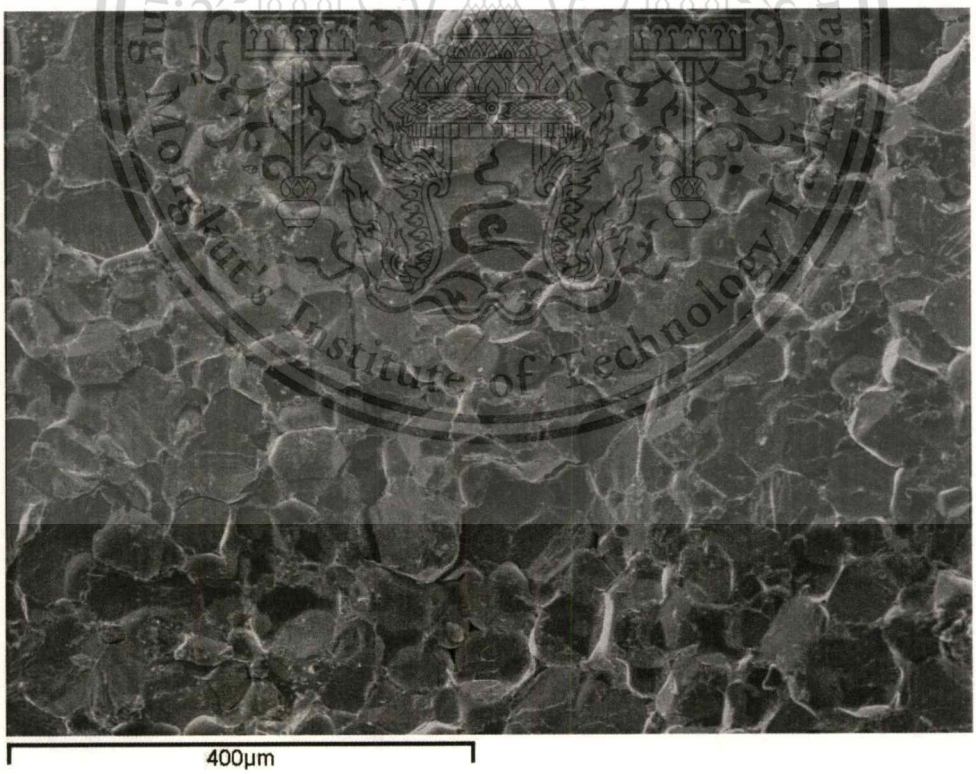

Figure 4.51 Fracture surface of W-(Ni-Cu-Co) specimens sintered at 1450°C for 8 hours.

From the experimental results, it indicates that with varied sintering temperature from 1350 to 1450°C, increasing sintering temperature trends to increase sintered density and mechanical properties. Therefore, it was interesting to further study the effects of sintering temperature at higher than 1450°C, such as 1500 and 1550°C. Nevertheless, due to the limitation of the sintering furnace, the highest generable sintering temperature is 1450°C. Sintering at temperature higher than 1450°C could not performed. From the literatures in section 2.2.4.4, temperature is a main parameter causes the atom motion and bond diffusion. The difference of sintering temperature contributed to the difference of the sinter density and mechanical properties (German, 1994). As the temperature increases, porosity decreases and grain size grows. The decreasing of porosity results in the increase of densification. Therefore, shrinkage of sintered parts increases as sintering temperature increases. However, higher sintering temperature causes the more extensive necking between tungsten particles and grain growth, leading to the decrease of mechanical properties.

Jigui *et al.* (2010) reported that with increasing sintering temperature from 1150 to 1250°C, microstructure showed more extensive necking and conjoining between particles. This more extensive necking between tungsten particles at higher temperatures also attributes for a greater degree of shrinkage observed for components sintered at higher temperatures.

Li *et al.* (2009) reported the effect of pure molybdenum specimens sintered at different temperature, ranging from 1550 to 1900°C, that grains and pores were coarsened as sintering temperature increasing. Optimal mechanical properties were achieved at 1850°C. The sintering at 1900°C caused a reduction in mechanical properties due to grain growth and pore coarsening.

Therefore, sintering at temperature higher than 1450°C may result in increasing of sintered density and greater degree of shrinkage but decreasing of mechanical properties similar to the results of long sintering time.

Since it is obvious from the results of variation of sintering times at sintering temperature of 1450°C that sintering time for 3 hours provided optimal sintered density and mechanical properties. Therefore, further different sintering vacuum levels and nitrogen atmosphere were also employed for sintering the brown parts at 1450°C for 3 hours.

4.8 Effects of Sintering Atmospheres

From the previous section, the highest sintered density of 18.02 g/cm^3 was observed from W-(Ni-Cu-Co) specimens sintered at 1450°C for 3 hours under vacuum atmosphere with the sintering chamber pressure of 10^{-5} bar. Sintered densities of the W-(Ni-Cu-Co) specimens sintered at 1450°C for 3 hours with different sintering atmospheres are shown in **Figure 4.52**. It was found that sintering in the higher sintering chamber pressure, the lower densities. Firstly, under vacuum sintering, with increases sintering chamber pressure from 10^{-5} to 10^{-4} bar the sintered density decreases from 18.02 to 17.89 g/cm^3. The density further decreases to 17.82 g/cm^3 when the sintering chamber pressure was increased to the sintering vacuum pressure level of 10^{-3} bar. In addition, specimens sintered under N_2 atmosphere had a little higher density (17.95 g/cm^3) than those sintered under vacuum atmosphere with the chamber pressure of 10^{-4} and 10^{-3} bar (17.89 and 17.82 g/cm^3) but lower in mechanical properties. The shrinkage along grip width, gauge width, length and thickness at various sintering temperatures and sintering times are shown in **Figure 4.53**, **4.54**, **4.55** and **4.56** respectively. The shrinkage follows a similar trend as density because it is closely related to the densification. The results show that the W-(Ni-Cu-Co) specimens sintered with higher sintering chamber pressure shrank less than those sintered with the lower sintering chamber pressure at all positions. The shrinkages of W-(Ni-Cu-Co) specimens sintered at 1450°C for 3 hours with various sintering atmospheres are slightly different and show the result in agreement to the density. Mechanical properties with ultimate tensile strength, yield strength, modulus and hardness are presented in **Figure 4.57**, **4.58**, **4.59** and **4.60** respectively. The mechanical properties also show the similar trends as the density, in which mechanical properties decrease with increasing sintering chamber pressure. It can be seen that W-(Ni-Cu-Co) specimens sintered with lower sintering chamber pressure trend to provide better tensile properties, i.e. higher UTS and yield strength. In addition, nitrogen atmosphere gave similar results as those of the cases of increased chamber pressure. Microstructures of W-(Ni-Cu-Co) specimens sintered at 1450°C for 3 hours under vacuum atmosphere with the sintering chamber pressure of 10^{-5}, 10^{-4}, 10^{-3} bar and under N_2 atmosphere are shown in **Figure 4.61**, **4.62**, **4.63** and **4.64** respectively. It was observed that all microstructures exhibited the uniform dispersion of tungsten particles in the metal binder matrix. **Figure 4.65** presents the microstructures of the specimens sintered in different conditions. The protective atmosphere of N_2 effectively prevents air from entering the furnace, thus effective in oxide reduction during sintering. This may result in

higher sinter density than specimens sintered under vacuum atmosphere with the sintering chamber pressure of 10^{-4} and 10^{-3} bar. XRD pattern of W-(Ni-Cu-Co) specimens sintered at 1450°C for 3 hours under N_2 atmosphere is shown in **Figure 4.66**. XRD examination detected two phase of W and $Cu_{0.81}Ni_{0.19}$ in the sintered specimen. New compounds of nitride formation were not detected. However, during sintering under N_2 atmosphere, some amount of nitrogen may absorbed into specimens and form nitrogen solid solution infiltrating between tungsten particles. This may result in a reduction of mechanical properties.

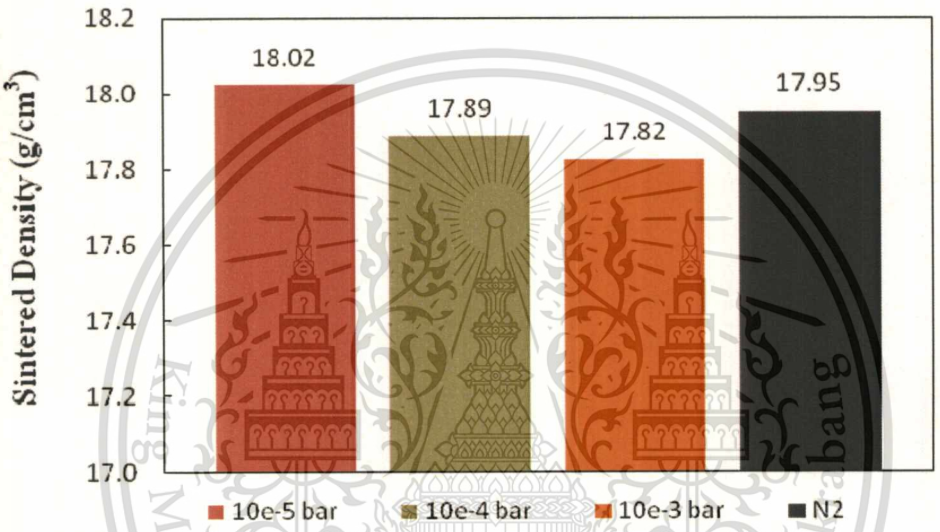

Figure 4.52 Densities of W-(Ni-Cu-Co) specimens sintered at1450°C for 3 hours in different sintering atmospheres.

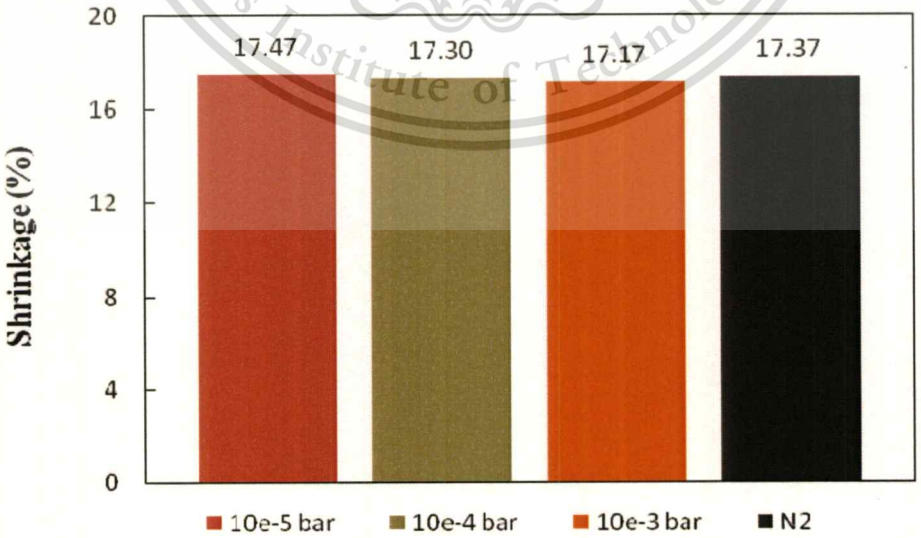

Figure 4.53 The shrinkage along grip width of sintered W-(Ni-Cu-Co) specimens sintered at1450°C for 3 hours in different sintering atmospheres.

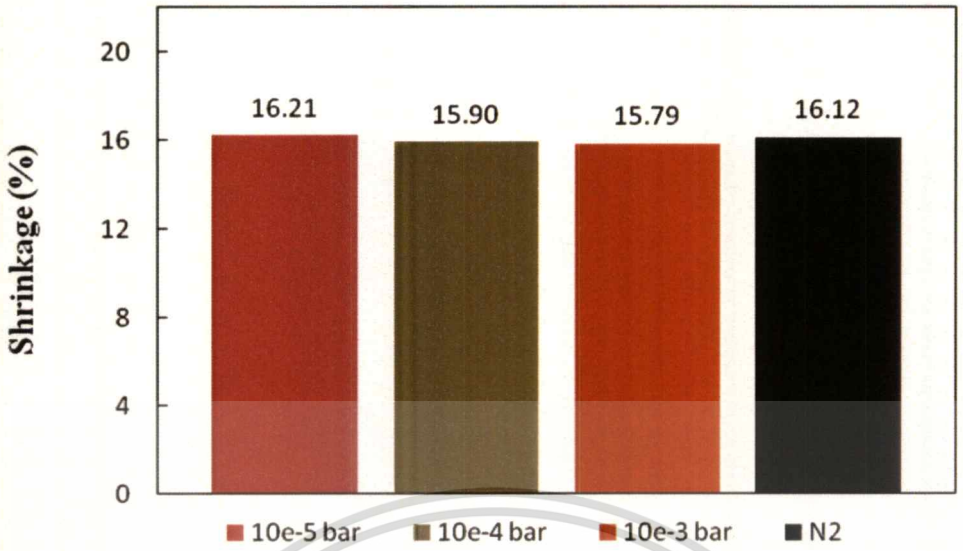

Figure 4.54 The shrinkage along gauge width of sintered W-(Ni-Cu-Co) specimens sintered at1450°C for 3 hours in different sintering atmospheres.

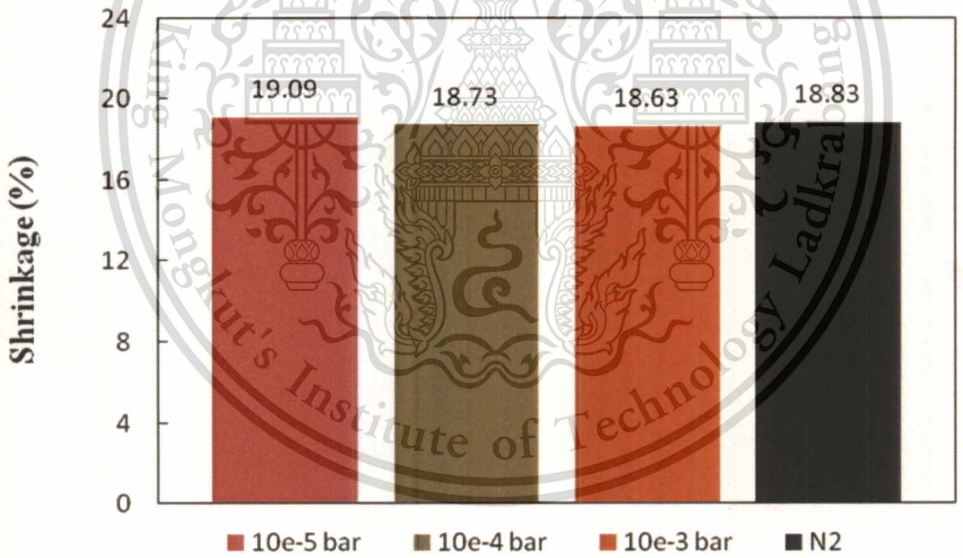

Figure 4.55 The shrinkage along length of sintered W-(Ni-Cu-Co) specimens sintered at1450°C for 3 hours in different sintering atmospheres.

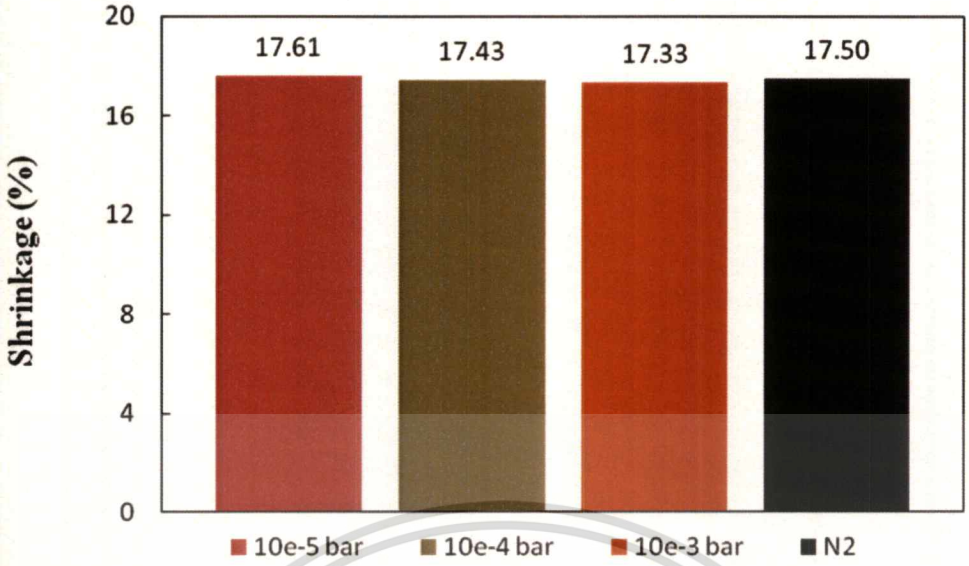

Figure 4.56 The shrinkage along thickness of sintered W-(Ni-Cu-Co) specimens sintered at1450°C for 3 hours in different sintering atmospheres.

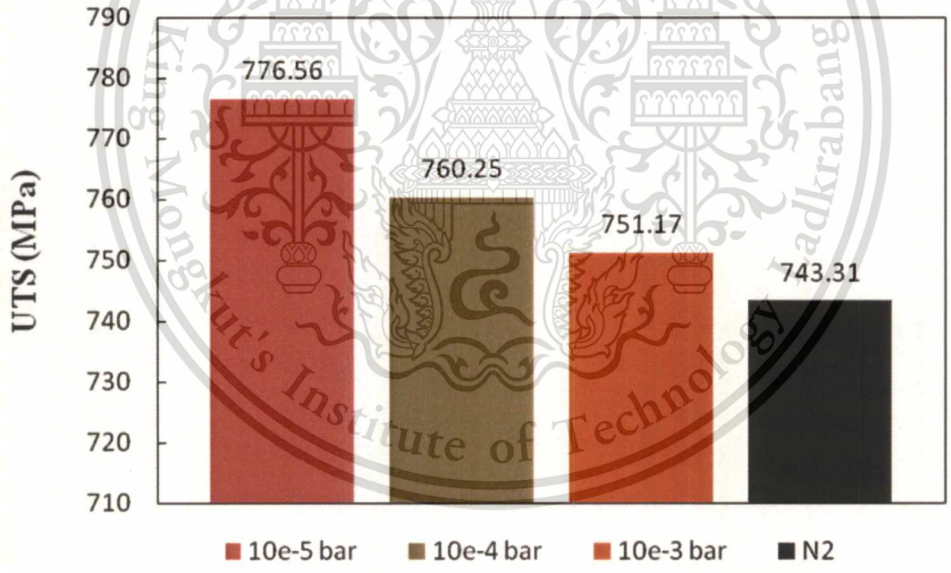

Figure 4.57 Ultimate tensile strength of W-(Ni-Cu-Co) specimens sintered at1450°C for 3 hours in different sintering atmospheres.

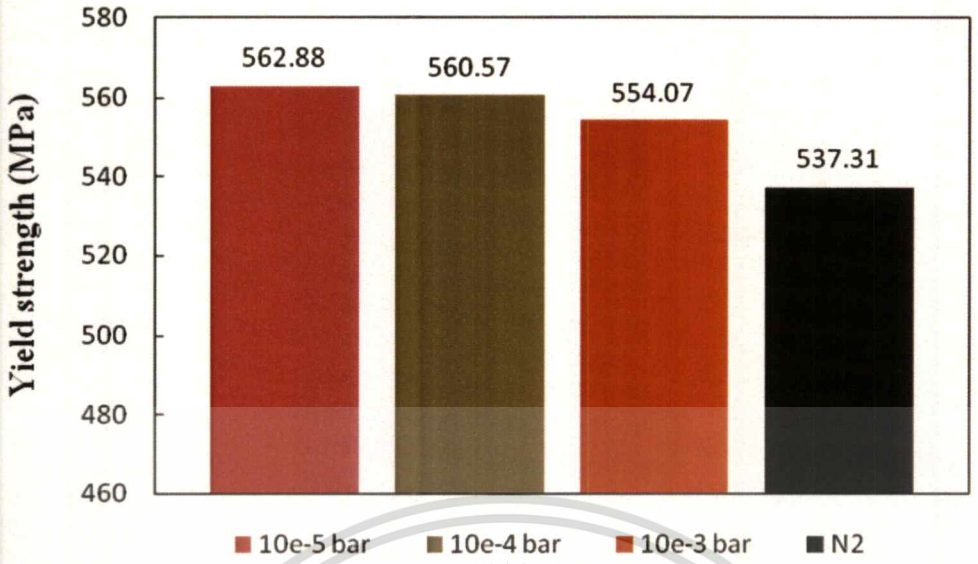

Figure 4.58 Yield strength of W-(Ni-Cu-Co) specimens sintered at1450°C for 3 hours in different sintering atmospheres.

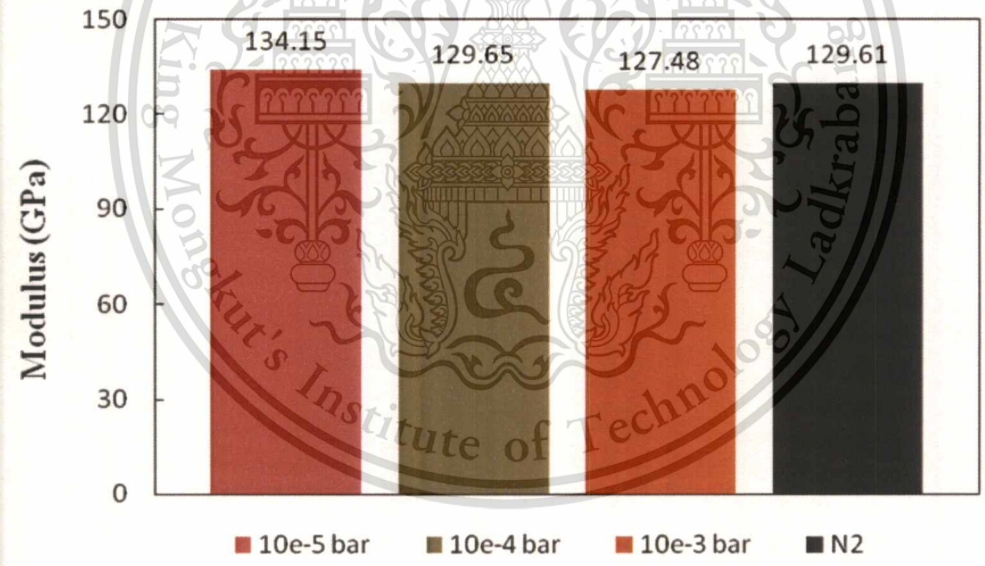

Figure 4.59 Modulus of W-(Ni-Cu-Co) specimens sintered at1450°C for 3 hours in different sintering atmospheres.

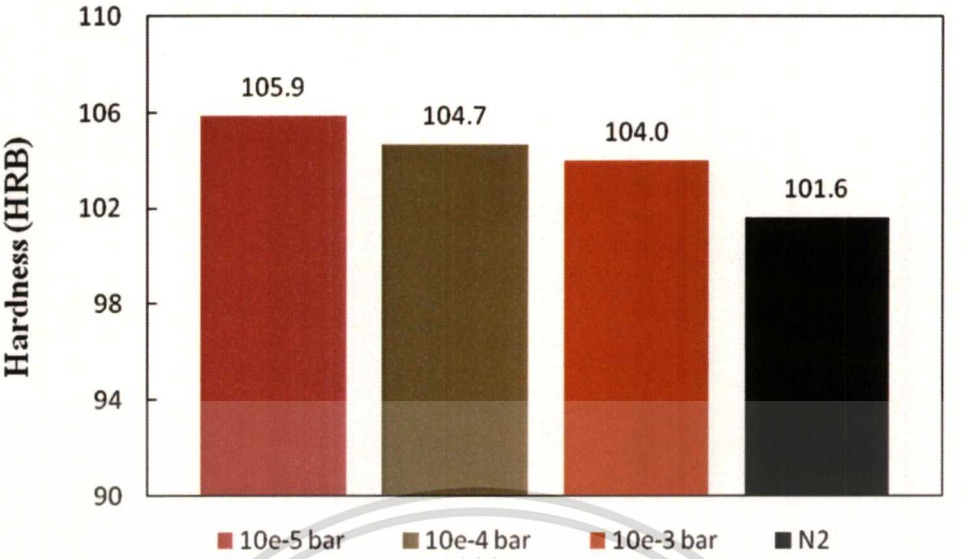

Figure 4.60 Hardness of W-(Ni-Cu-Co) specimens sintered at1450°C for 3 hours in different sintering atmospheres.

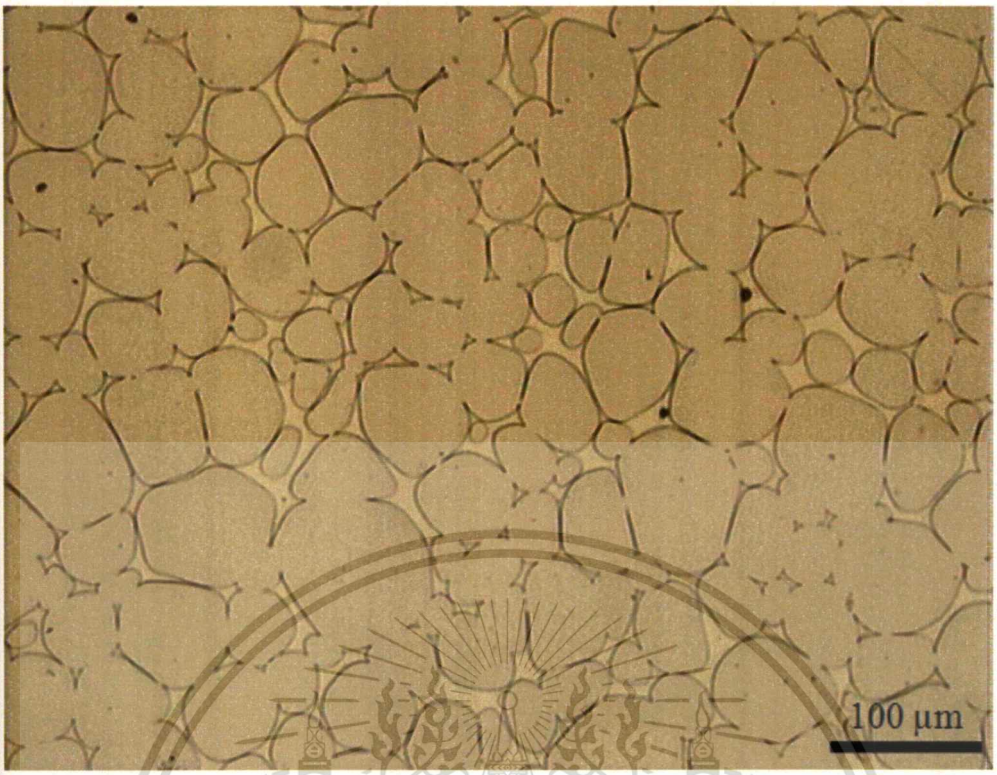

Figure 4.61 Microstructure of W-(Ni-Cu-Co) specimen sintered at 1450°C for 3 hours under vacuum atmosphere with sintering chamber pressure of 10^{-5} bar.

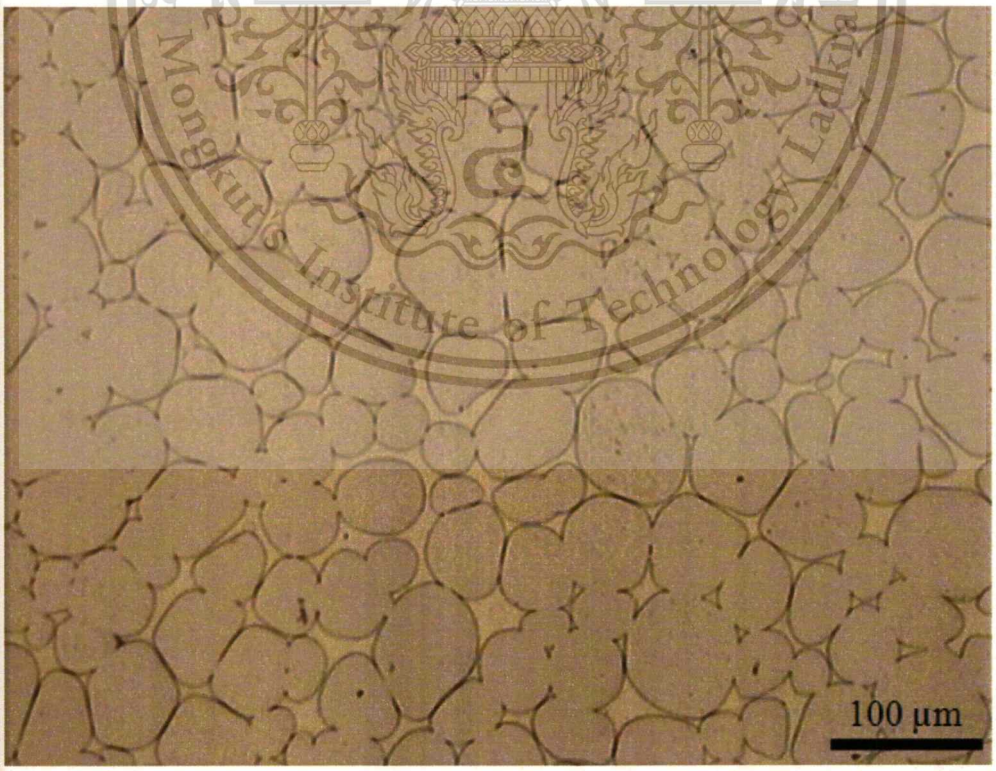

Figure 4.62 Microstructure of W-(Ni-Cu-Co) specimen sintered at 1450°C for 3 hours under vacuum atmosphere with sintering chamber pressure of 10^{-4} bar.

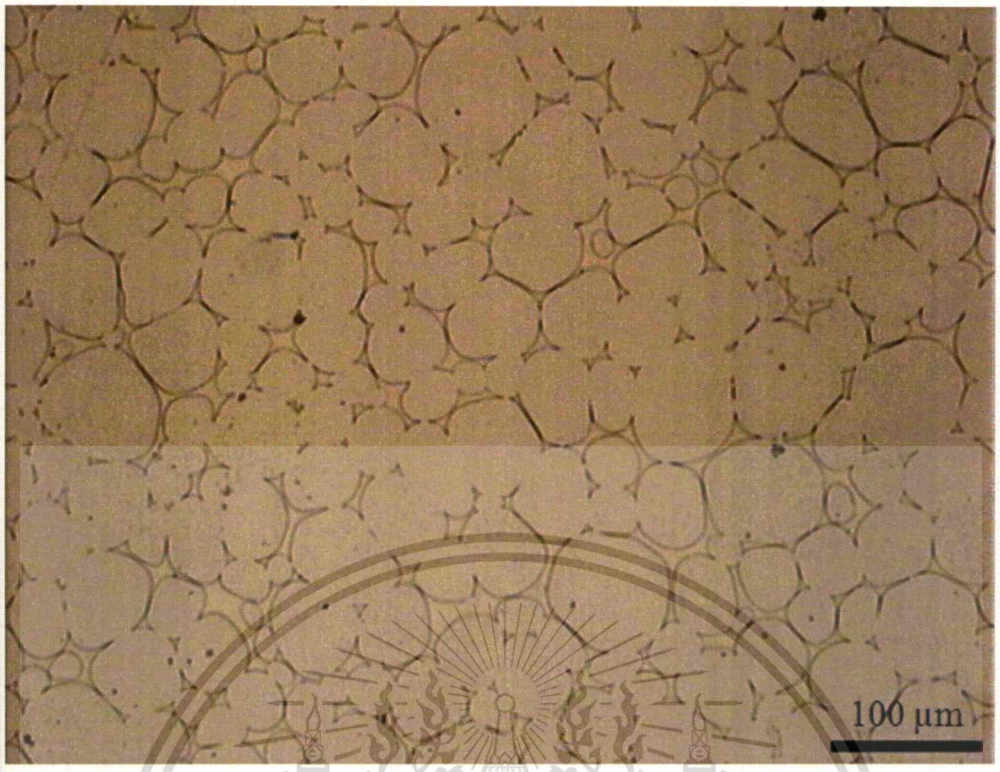

Figure 4.63 Microstructure of W-(Ni-Cu-Co) specimen sintered at 1450°C for 3 hours under vacuum atmosphere with sintering chamber pressure of with 10^{-3} bar.

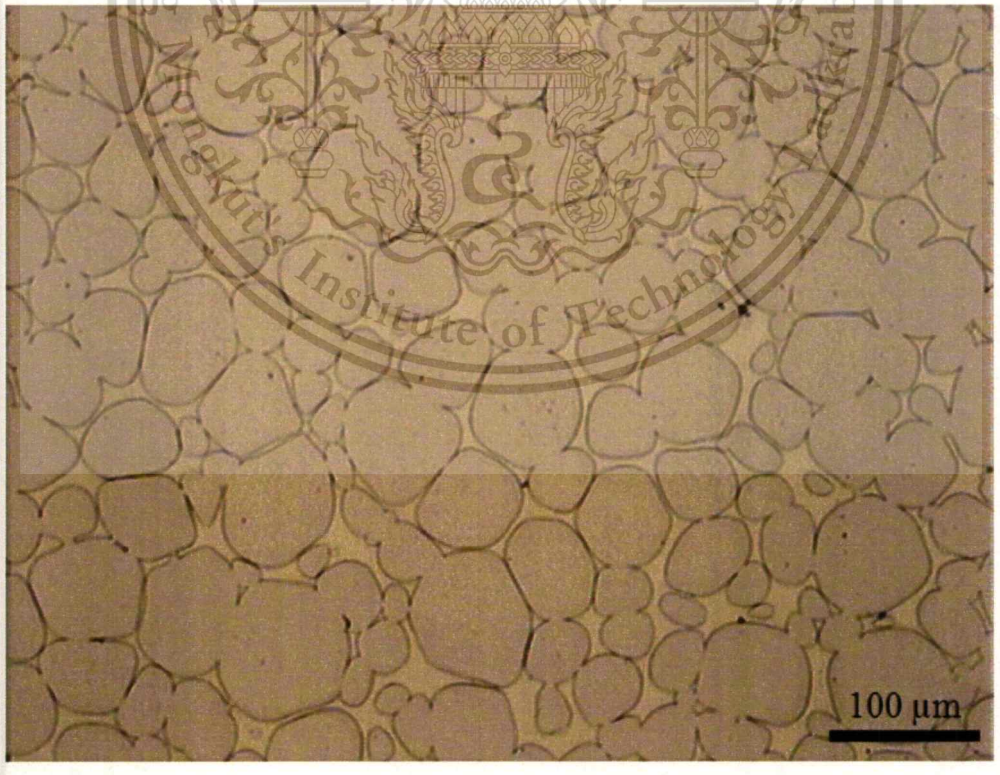

Figure 4.64 Microstructure of W-(Ni-Cu-Co) specimen sintered at 1450°C for 3 hours under N_2 atmosphere.

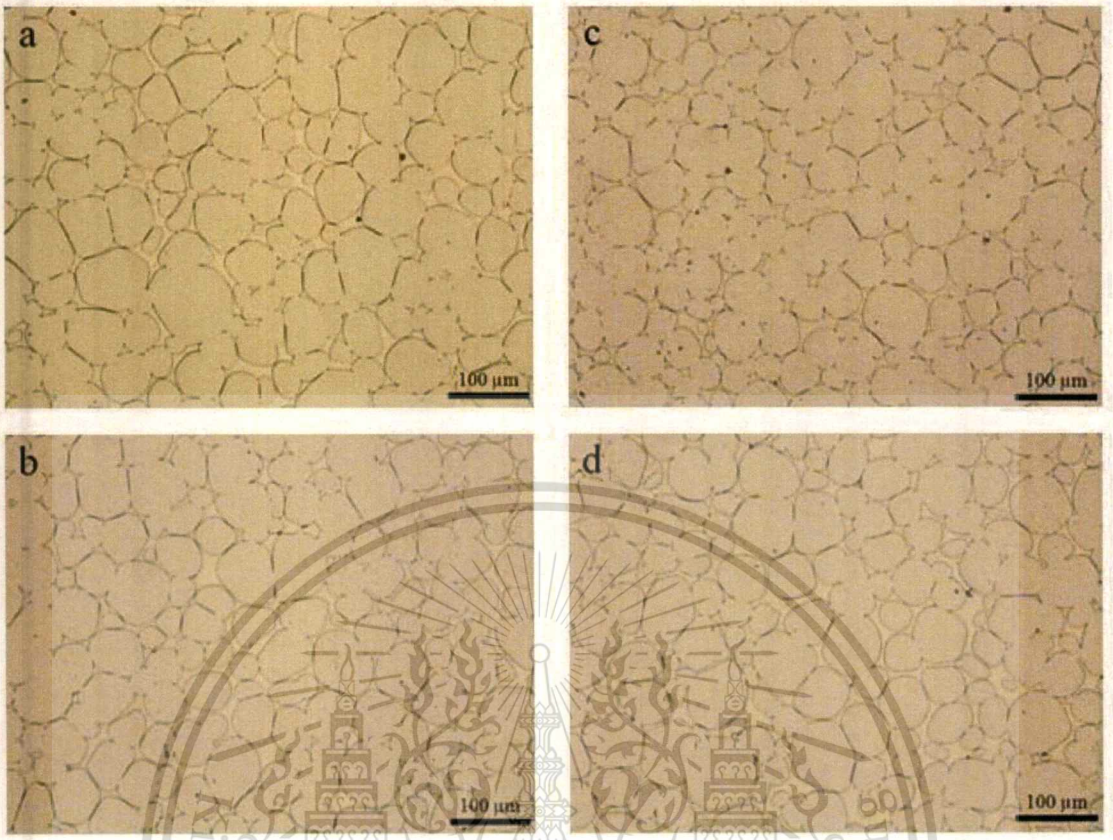

Figure 4.65 Microstructures of W-(Ni-Cu-Co) specimen sintered at 1450°C for 3 hours under vacuum atmosphere with sintering chamber pressure of (a) 10^{-5} bar, (b) 10^{-4} bar and (c) 10^{-3} bar and (d) under N_2 atmosphere.

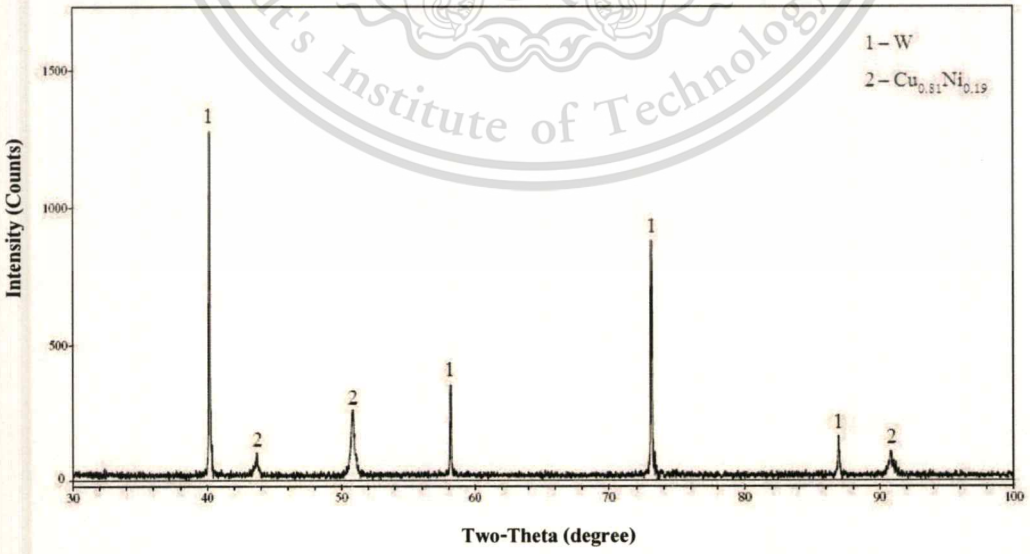

Figure 4.66 XRD pattern of W-(Ni-Cu-Co) specimen sintered at 1450°C for 3 hours under N_2 atmosphere.

In this work, the sintering conditions affected directly on microstructure, density and mechanical properties of sintered W-(Ni-Cu-Co) specimens. The results show that W-(Ni-Cu-Co) specimens sintered at 1450°C for 3 hours under vacuum atmosphere with the sintering chamber pressure of 10^{-5} bar had highest density of 18.02 g/cm^3 and optimal mechanical properties with UTS of 776 MPa, tensile strength of 562 MPa, Modulus of 134 GPa and hardness of 105.9 HRB. The higher density and mechanical properties were due to liquid phase sintering which occurred when the sintering temperature reached the solid to liquid phase transition temperature. Therefore, at this sintering condition, the Ni-Cu-Co liquid phase penetrated and filled the pores between tungsten particles completely. So minimum pores and defects were observed in the W-(Ni-Cu-Co) specimen sintered at this sintering condition.

The experimental results given above also indicate that porosity of the binder phase presenting in the intergranular regions is detrimental to mechanical properties. It was concluded that mechanical properties showed the results in agreement with the density. Better tensile properties were obtained in the highly dense materials. However, tensile properties of this material, sintered at 1450°C, were sensitive to sintering times. The sintering times shorter or longer than the optimum one caused higher volume fraction of pores in the sintered W-(Ni-Cu-Co) specimens. Low ductility of the sintered W-(Ni-Cu-Co) specimens was attributed to porosity. When compared to the tensile properties, hardness of these sintered materials was less sensitive to the porosity difference. This may be attributed to small volume fraction of the binder phase.

CHAPTER 5

CONCLUSION AND SUGGESTIONS

5.1 Conclusion

Sintering temperature and sintering time affect microstructure and significantly influence the density and mechanical properties of sintered W-(Ni-Cu-Co) specimens. In this experiment, at the sintering temperature of 1450°C, the Ni-Cu-Co liquid phase occurred, then penetrated and filled the pores between tungsten particles. Therefore, at this sintering temperature, microstructure of the sintered W-(Ni-Cu-Co) specimens showed spherical shape of tungsten particles dispersed in a metal binder matrix. The porosity in metal binder was changed with sintering temperature and sintering times. Porosity was reduced when the sintering temperature increased, at the same time the grain size increased. Sintering with too short times resulted in incomplete penetration of the liquid phase so pores could not be removed. From experimental results, a complete penetration with the minimum pores and defects was found at the sintering temperature of 1450°C for 3 hours under vacuum atmosphere with the sintering chamber pressure of 10^{-5} bar. Therefore, the W-(Ni-Cu-Co) specimens sintered under this sintering condition showed the highest density of 18.02 g/cm3 and optimal mechanical properties with UTS of 776 MPa, Tensile strength of 562 MPa, Modulus of 134 GPa and hardness of 105.9 HRB. Increase of sintering times showed no improvement of tensile strengths. For long sintering time (6 and 8 hours) at the sintering temperature of 1450°C resulted in coalescence to each other between tungsten particles and inevitably porosity growth. This phenomenon caused inferior density and mechanical properties of the sintered specimens. This indicates that mechanical properties significantly depend on the microstructural parameters such as tungsten grain size, tungsten particles contiguity and porosity. Neither density nor mechanical properties were improved with sintering time longer than 3 hours. The specimens sintered at 1450°C with too long sintering time (8 hours) were brittle. From the SEM micrograph of fracture surfaces of sintered W-(Ni-Cu-Co) specimens, it can conclude that the matrix failure and the tungsten-matrix failure are observed in the W-(Ni-Cu-Co) specimens sintered at 1400°C for 3 hours. While the fracture takes place at cleavage fracture of tungsten grains and interface between tungsten particles of W-(Ni-Cu-Co) specimens sintered at 1450°C for 3 hours. For specimens sintered for too long sintering times (6 and 8 hours), the fracture mode changes from tungsten cleavage and interface between tungsten particles to matrix and tungsten-matrix failure are associated with the

lower tensile properties. The fracture behavior of W-(Ni-Cu-Co) specimens corresponds to the mechanical properties. Which is higher when the fracture is occur at tungsten cleavage and interface between tungsten particles than those occur at the matrix failure. From the shrinkage measurement, the results showed shrinkage along all dimensions and showed a similar trend at all directions. The shrinkage of the sintered specimens also shows the result corresponding to the density. Different vacuum levels and nitrogen atmosphere were also studied for sintering the brown W-(Ni-Cu-Co) specimens at 1450°C for 3 hours. The results show that increasing of sintering chamber pressure caused detrimental effects on both physical and mechanical properties of the sintered tungsten specimens. In addition, nitrogen atmosphere gave similar results as those of the cases of increased chamber pressure.

5.2 Suggestions

Although this work was finished, it was only the first step tungsten injection molding process. There are some suggestions to the work for further study as follow:

5.2.1 Further study debinding parameters, i.e. debinding atmosphere, acid feeding rate, heating rate, and debinding temperature.

5.2.2 Further examine and analyze the effects of sintering chambers pressure on mechanical properties.

5.2.3 In order to study the effect of sintering atmosphere on physical and mechanical properties, other sintering atmospheres should be employed such as H_2 atmosphere.

5.2.4 Another suggestion is on sintering times, from the experiment results, a transition temperature from solid to liquid (Ni-Cu-Co) metal binder may be at somewhere between 1400 to 1450 °C. Thus, sintering time in this range should be study more specified.

REFERENCES

1. ASM International. 1984. **ASM Handbook of Powder Metallurgy**. 7 : 152-154.
2. ASM International. 1998. **Powder Metal Technologies and Applications.** 7 : 831-851.
3. German, R.M., Bose, A. 1997, Injection Molding of Metals and Ceramics, **Metal Powder Industries Federation,** Princeton, New Jersey.
4. German, R.M. 1990, **Powder Injection Molding, Metal Powder Industries Federation,** Princeton, New Jersey.
5. German, R.M. 1994, **Powder Metallurgy Science,** 2nd Edition, Metal Powder Industries Federation, Princeton, New Jersey.
6. German, R.M. 2001, **Center for Innovative Sintered Products,** The Pennsylvania State University, USA.
7. Akhtar, F. 2008, "An Investigation on the Solid State Sintering of Mechanically Alloyed Nano-Structured 90W-Ni-Fe Tungsten Heavy Alloy", **Int. Journal of Refractory Metals & Hard Materials**. 26 : 145-151.
8. Bollina, R., German, R.M. 2004, "Heating Rate Effects on Microstructure Properties of Liquid Phase Sintered Tungsten Heavy Alloys", **Int. Journal of Refractory Metals & Hard Materials**. 22 : 117-127.
9. Das, J., Kiran, U.R., Chakraborty, A., Prasad, N.E. 2009, "Hardness and Tensile Properties of Tungsten Based Heavy Alloys Prepared by Liquid Phase Sintering Technique", **Int. Journal of Refractory Metals & Hard Materials**. 27 : 577-583.
10. Das, J., Rao, G.A., Pabi, S.K. 2010, "Microstructure and Mechanical Properties of Tungsten Heavy Alloys", **Materials Science and Engineering**. A 527 : 7841-7847.
11. Ding, L., Xiang, D.P., Li, L.L., Li, J.B. 2012, "Effects of Sintering Temperature on Fine-Grained Tungsten Heavy Alloy Produced by High-Energy Ball Milling Assisted Spark Plasma Sintering", **Int. Journal of Refractory Metals & Hard Materials**. XX : XXX-XXX.

REFERENCES (CONT.)

12. Fujiki, A. 2001, "Present State and Future Prospects of Powder Metallurgy Parts for Automotive Applications", **Materials Chemistry and Physics**. 67 : 298-306.

13. Krueger, D., Bloemacher, M., Weinand, D. 1993, "Rapid Catalytic Debinding MIM Feedstock: A New Technology Grows Into A Manufacturing Process", **Adv. Powder Metall. Particulate Mater**. 5 : 121-132.

14. Ho, P.W., Li, Q.F., Fuh, J.Y.H. 2008, "Evaluation of W-Cu Metal Matrix Composites Produced by Powder Injection Molding and Liquid Infiltration", **Materials Science and Engineering**. A 485 : 657-663.

15. Hong, S.H., Ryu, H.J. 2003, "Combination of Mechanical Alloying and Two-stage Sintering of a 93W-5.6Ni-1.4Fe Tungsten Heavy Alloy", **Materials Science and Engineering**. A344 : 253-260.

16. Huang, B., Fan, J., Liang, S., Qu, X. 2003, "The Rheological and Sintering Behaviour of W-Ni-Fe Nano-Structured Crystalline Powder", **Journal of Materials Processing Technology**. 137 : 177-182.

17. Lee, K.H., Cha, S.I., Ryu, H.J., Hong, S.H. 2007, "Effect of Two-Stage Sintering Process on Microstructure and Mechanical Properties of ODS Tungsten Heavy Alloy", **Materials Science and Engineering**. 458 : 323-329.

18. Jigui, C., Yanbo, W.L.C., Jinchuan, Z., Peng, S., Jie, D. 2010, "Fabrication of W-20wt.%Cu Alloys by Powder Injection Molding", **Journal of Materials Processing Technology**. 210 : 137-142.

19. Li, D., Hou, H., Tan, Z., Lee, K. 2009, "Metal Injection Molding of Pure Molybdenum", **Advanced Powder Technology**. 20 : 480-487.

20. Loh, N.H., Tor, S.B., Khor, K.A. 2001, "Production of Metal Matrix Composite Part by Powder Injection Molding", **Journal of Material Processing Technology**. 108 : 398-407.

REFERENCES (CONT.)

21. Moballegh, L., Morshedian, J., Esfandeh, M. 2005, "Copper Injection Molding using a Thermoplastic Binder based on Paraffin Wax", **Materials Letters**. 59 : 2832-2837.

22. Piotter, V., Zeep, B., Noraitra, P., Ruprecht, R. 2008, "Development of a Powder Metallurgy Process for Tungsten Components", **Fusion Engineering and Design**. 83 : 1517-1520.

23. Qu, X., Fan, J., Huang, B. 2001, "Injection Molding of W-Ni-Fe Nanocomposite Powder Prepared by Mechanical Alloying", **J. Mater. Sci. Technol.**, Vol. 17 No. 6.

24. Setasuwon, P., Bunchavimonchet, A., Danchaivijit, S. 2008, "The Effects of Binder Components in Wax/Oil Systems for Metal Injection Molding", **Journal of Material Processing Technology**. 196 : 94-100.

25. Suri, P., Atre, S.V., Randall M. German R.M., Souza, J.P.d. 2003, "Effect of Mixing on the Rheology and Particle Characteristics of Tungsten-Base Powder Injection Molding Feedstock", **Materials Science and Engineering**. A356 : 337-344.

26. Wu, Y., German, R.M., Marx, B., Bollina M., Bell, Matt. 2003, "Characteristics of Densification and Distortion of Ni-Cu Liquid-Phase Sintered Tungsten Heavy Alloy", **Materials Science and Engineering**. A344 : 158-167.

27. Xu, X., Upadhyaya, A., German, R.M. Iacocca, R. 1999, "The Effect of Porosity on Distortion of Liquid Phase Sintered Tungsten Heavy Alloys", **Int. Journal of Refractory Metals & Hard Materials**. 17 : 369-379.

28. Ye, H., Liu, X.Y., Hong, H. 2008, "Fabrication of Metal Matrix Composites by Metal Injection Molding-A review", **Journal of Materials Processing Technology**. 200 : 12-24.

29. Yimin, L., Xuanhui, Q., Zhilin, L., Baiyun, H. 1998, "Injection Molded Tungsten Heavy Alloy", **State Key Laboratory for Powder Metallurgy**, Central South University of Technology, Changsha 410083, P.R. China.

REFERENCES (CONT.)

30. Zaky, M.T. 2004, "Effect of Solvent Debinding Variables on the Shape Maintenance of Green Molded Bodies", **Journal of Materials Science**. 39 : 3397-3402.

31. Zeep, B., Norajitra, P., Piotter , V., Boehm, J., Ruprecht, R., Hausselt, J. 2007, "Net Shaping of Tungsten Components by Micro Powder Injection Molding", **Fusion Engineering and Design**. 82 : 2660-2665.

32. Zhu, Y.B., Wang, Y., Zhang, X.Y., Qin, G.W. 2007, "W/NiFe Interfacial Characteristics of Liquid-Phase Sintered W-Ni-Fe Alloy", **Int. Journal of Refractory Metals & Hard Materials**. 25 : 275-279.

33. Zu, Y.S., Lin, S.T. 1997, "Optimizing the Mechanical Properties of Injection Molded W-4.9%Ni-2.1%Fe in Debinding", **Journal of Material Processing Technology**. 71 : 337-342.

APPENDIX A

MATERIAL AND PROCESSING INFORMATION

Appendix A-1: Product information of Catamold W

Data Sheet **Catamold® W**

2002-09-24

supersedes version 2002-08-07

® = Reg. Trademark of BASF Aktiengesellschaft

Product Catamold ® W

Product Description Ready-to-mold granules for the production of a **tungsten heavy metal** sintered components using the BASF technology.

Typical composition after Sintering

W (%)	Ni + Cu + Co
≥ 94,0	Balance

Processing Molding on standard injection molding machines used for thermoplastic polymers. Catalytic debinding according to BASF technology. Sintering in hydrogen.

Characteristic Properties

Density	≥ 17.8 g/cm³
Hardness HV1 (typical)	320
Magnetic Properties	Non-magnetic
Thermal Conductivity (54°C)	80 W/mK

Figure A-1 Product information of tungsten heavy alloy feedstock used in this study.

BIOGRAPHY

Name: Mr. Jittrabhanu Lamlerttham

Date of Birth: September 21, 1986

Place of Birth: Bangkok, Thailand

Education:

2005-2008	B. Eng. in Mechanical Engineering, Department of Mechanical Engineering, King Mongkut's Institute of Technology Ladkrabang (KMITL)
2009-2011	M. Eng. in Automotive Engineering (International program), International College, King Mongkut's Institute of Technology Ladkrabang (KMITL)

Scholarship:

2009-2011	Full scholarship for study in the master degree from National Science and Technology Development Agency (NSTDA)

Publications:

1. J. Lamlerttham, P. Wila, N. Tosangthum, A. Daraphan, R. Tongsri, J. Charoensuk and Y. Saito. "Sintering Optimization of W-(Ni-Cu-Co) for Metal Injection Molding." **Proceeding of the 5th Thailand Metallurgy Conference**, Bangkok, Thailand, January 19-20, 2012.
2. J. Lamlerttham, P. Wila, N. Tosangthum, A. Daraphan, R. Tongsri, J. Charoensuk and Y. Saito. "Sintering Optimization of W-(Ni-Cu-Co) for Metal Injection Molding." **Proceeding of the 8th International Conference on Automotive Engineering,** Bangkok, Thailand, April 2-5, 2012.